

Symposium of High Energy Solar Physics  
 Institute of Space and Aeronautical Science  
 Tokyo, Japan

SOFT X-RAY ASTRONOMY USING  
 GRAZING INCIDENCE OPTICS

John M. Davis  
 American Science and Engineering, Inc.  
 Cambridge, Massachusetts 02139 USA

ABSTRACT

The instrumental background of X-ray astronomy with an emphasis on high resolution imagery is outlined. Optical and system performance, in terms of resolution, are compared and methods for improving the latter in finite length instruments described. The method of analysis of broadband images to obtain diagnostic information is described and is applied to the analysis of coronal structures.

1. Instrumental Background

Although X-rays are characterized by their ability to penetrate matter classical dispersion theory shows that below a critical angle, X-rays, incident on a denser medium will undergo total external reflection. The critical angle, defined in terms of atomic constants, is

$$\theta_c = \left[ \frac{e^2}{\pi m c^2} \frac{Z \rho N}{A} \right]^{1/2} \lambda$$

and is shown for a variety of materials in Figure 1. These angles fall in the range of a few degrees and therefore X-ray optical systems have to be designed with their reflecting surfaces nearly parallel to their optical axis. For a parabola, this means using the far zone of the surface. However, this region of the surface does not satisfy the Abbe sine condition and the image suffers from coma, i.e., a point source will be imaged as a circle having an angular radius equal to the displacement of the point source from the optical axis. This can be minimized by introducing a second reflecting surface (Wolter, 1952) and in the X-ray region a paraboloid-hyperboloid combination is most commonly used.

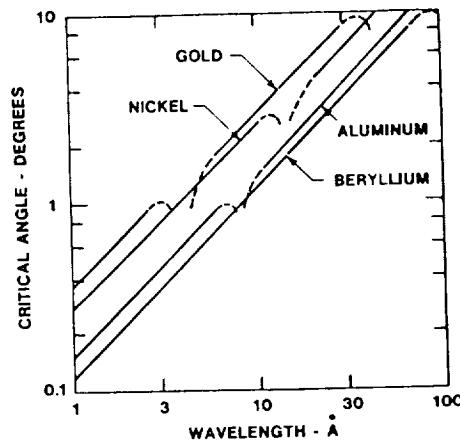


Figure 1. The variation of the critical angle with wavelength for several materials.

For the past 20 years we, at AS&E, have stressed the importance of high resolution imagery. The resolution of a particular system is a combination of the resolution of the optics, which is established by the manufacturing tolerances, and of the detecting system. X-ray mirrors can be made with angular

resolution of 1 arc second. However, even when film has been used, most X-ray images have been limited by the detector. In the future, when the missions dictate the use of electronic imaging detectors, with relative coarse picture elements, compared to film, the situation will be worse unless the images can be made correspondingly larger. If longer focal lengths are prohibited, magnifying optics provide the only alternative. Two types of systems are shown in Figure 2. We are developing the second, which uses hyperboloid-hyperboloid

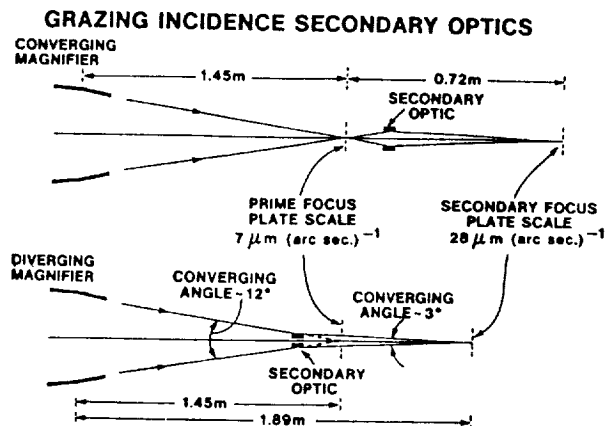


Figure 2. Diagrams of the two possible designs for secondary grazing incidence optics. The dimensions refer to systems based on an existing primary mirror and a magnification of 4.

optics (Davis *et al.*, 1984) since it combines the greatest magnification in the shortest length. Currently magnifications of 4 are near the practical limit set by the tolerance on the axial slope. The difficulties in this approach are that it adds two extra reflections, requiring extra smooth surfaces, and provides images with a field of view limited to a few square arc minutes.

## 2. Method of Analysis

To extract the properties of the coronal plasma (temperature, density and pressure) from the images, we relate them to the focal plane irradiance through the use of a model spectrum (Vaiana *et al.*, 1977). The spectrum gives the power emitted by unit volume of plasma with density  $N_e$  at temperature  $T$  in the wavelength range  $\Delta\lambda$ . If this incident spectrum is focussed by a telescope and the beam passed through a filter, the instrument will detect a spectrum that has been modified by the reflection efficiency of the mirrors and the transmission of the filter. By using more than one filter, different integrals of the spectrum will be sampled. Using the model spectrum, we can form ratios of the filter transmissions to create spectral hardness indices as a function of temperatures. These allow pairs of images to be converted into temperature maps and once the temperature is known, the focal plane irradiance can be converted into emission measure, or the  $\int N_e^2 dl$ , along the line of sight. Finally, if the geometry of the emitting structure is known, a density can be evaluated. Since the spectrum consists of a large number of lines and continuum, this method has the advantage of averaging and, since in general no single line, ion or continuum process is dominant, the impact of uncertainties in atomic parameters and element abundances is minimized.

### 3. Physical Properties of Loops

Soft X-ray observations have dispelled the idea of a vertically layered corona and have replaced it by a view dominated by magnetic loops on all spatial scales. The loops are long lived and therefore must exist in an equilibrium state where the power losses, though conduction and radiation, must balance the power inputs. The sources and mechanisms of the power loss are a mystery. Figure 3 is a schematic representation of the power loss as a function of temperature for a coronal loop.

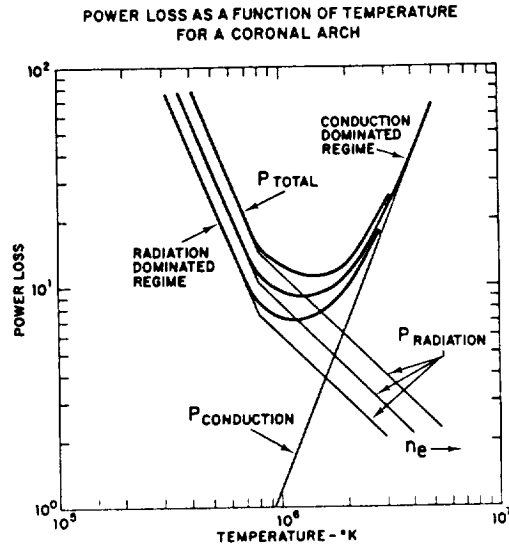


Figure 3. A schematic diagram showing the dependence of the power losses of a coronal arch on its temperature.

Shown are the conductive losses which are proportional to  $T^{5/2}$  and the radiative losses which are proportional to  $N_e T^2$  at coronal temperatures. The total power loss is the sum of these curves which has a minimum at a certain temperature. An equilibrium will exist when the power supply heating the loop balances the radiative and conductive losses. For the equilibrium to be stable the loop must exist on the conduction dominated branch of the total loss curve where small fluctuations in the power supply can be compensated by moving to a new equilibrium state. For instance if the heating supply decreases, the temperature will fall and although the radiation losses increase with falling temperature the conduction losses which are the dominant loss mechanism at these temperatures decrease sufficiently to allow a new equilibrium to be established at a slightly lower temperature. An increase in the heating supply will result in a new equilibrium at a higher temperature.

This is not the case if the loop exists on the radiation dominated branch of the total loss curve. Here where the radiation losses dominate the conduction losses a reduction in the heating supply leading to a decrease in temperature will result in an increase in the total losses which cannot be conduction stabilized at coronal temperatures and the loop will cool. This phenomenon is known as the radiative instability.

To reach this equilibrium state chromospheric 'evaporation' is invoked to fill the magnetic loop with coronal material. The process can be visualized by realizing that if power is dissipated in a magnetic structure, it will cause the material within the structure to rise rapidly in temperature because of its low thermal capacity, its low radiation losses and the negative temperature coefficient of the loss term. The eventual result will be that the majority of the dissipated power will be conducted to the chromosphere/transition region where it will heat that material to coronal temperatures which will allow it to rise and fill the loop. The increased radiation losses of the now dense loop will allow an equilibrium state to be reached. These ideas are discussed by Pye *et al.* (1978).

They have been used by Davis and Krieger (1982) to show how filaments could condense from coronal loops. This hypothesis was based on the observation that filament channels, i.e., regions in which the H-alpha data show a field structure identical to that surrounding the filament but where no filament exists, are located beneath arcades of coronal loops and that the quantity of material within the arcade is sufficient to form the filament.

In another study where we had obtained images using a finer grain emulsion than used on Skylab, we were able to evaluate the plasma parameters of a small bright loop, tentatively identified as a flaring bright point. The loop was 10 arc sec long by 1 arc sec wide and we found a density in excess of  $2 \times 10^{11} \text{ cm}^{-3}$  at a temperature of  $2 \times 10^6 \text{ K}$ . This low temperature is uncharacteristic of typical flare phenomena. Since the dimensions of the loop were known, we were able to calculate the total loss curves as a function of temperature. When the loop was located on the appropriate curve, it was found to exist on the radiation dominated branch of the curve and thus to be radiatively unstable. It is unlikely that the temperature determination could be in error by the amount necessary to place the arch on the conduction dominated branch for this would require temperatures above  $6 \times 10^6 \text{ K}$  which are ruled out by the observation.

Therefore, we appear to have an example of a bright loop cooling through the radiative instability. This identification depended critically on our ability, through the availability of high resolution images, to define the dimensions of the loop which allowed us to convert an emission measure into density.

This example and many others have confirmed our firmly held belief in the importance of obtaining images with the highest possible resolution if the secrets of the corona are to be revealed.

#### References

- Davis, J.M. and Krieger, A.S., *Solar Phys.* 81, 325 (1982)
- Davis, J.M. *et al.*, *Nuc. Instrum. and Methods* 221, 20 (1984)
- Pye, J.P. *et al.*, *Astron. & Astrophys.* 65, 123 (1978)
- Vaiana, G.S. *et al.*, *Space Sci. Instrum.* 3, 19 (1977)
- Wolter, H., *Ann. Physik* 10, 94 (1952)

4.2 X-Ray Bright Points and the Solar Cycle Dependence of Emerging Magnetic Flux

John M. Davis

American Science and Engineering, Inc.  
Cambridge, Massachusetts 02139

ORIGINAL FACE IS  
OF POOR QUALITY



X-RAY BRIGHT POINTS AND THE SOLAR CYCLE  
DEPENDENCE OF EMERGING MAGNETIC FLUX

John M. Davis

American Science and Engineering, Inc.  
955 Massachusetts Avenue  
Cambridge, Massachusetts 02139

ABSTRACT

Soft X-ray imaging of the solar corona during the period 1970 to 1978 has resulted in significant modifications to our view of the solar cycle with respect to both the properties of the large scale (coronal holes) and small scale (X-ray Bright Points) solar magnetic field. In the latter case the particular contribution is to the emerging magnetic flux. Sounding rocket observations combined with the Skylab data indicate that the XBP are anticorrelated with sunspot number and are the dominant contributors to the total emerging flux spectrum during all but the maximum phase of the solar cycle. A continuous data set covering a complete cycle would enable the validity of this result, which has serious implications for the nature of the solar dynamo, to be confirmed.

1.0 INTRODUCTION

Since the early sixties NASA has supported a program of high spatial resolution solar X-ray astronomy at AS&E. One of the prime objectives of this program has been the study of both the large and small scale variations occurring in the corona during the 11-year solar cycle. The studies have used the data from sounding rocket flights and Skylab; the latter providing a major contribution by establishing a baseline against which the sounding rocket observations can be compared.

During the first decade of the program major advances were made in the fabrication of the X-ray optics, in the preparation of the broadband filters used to select the various soft X-ray wavelength ranges and in the development of suitable photographic emulsions which are used as the recording medium. These three areas of development had all reached fruition by 1970 and produced for the first time the high quality X-ray images to which we have now grown accustomed. A panoramic representation of these data is shown in Figure 1 where images from 6 rocket

flights and 3 representative Skylab photographs are combined. The images cover the period 1970 to 1978 and show all the phases of the solar cycle except solar maximum, for which period no images of comparable quality exist. The combination of high resolution and sensitivity has revealed many new phenomena of which two have a direct bearing on the cyclical behavior of the solar magnetic field. The unique contribution of the X-ray images has been to clearly and unambiguously identify phenomena whose signatures, although present in the records of the photospheric magnetic field, tend to be obscured by a wealth of confusing detail.

## 2. CORONAL HOLES AND X-RAY BRIGHT POINTS

Historically the first major result of the program was the unambiguous identification of coronal holes followed by the recognition that equatorial coronal holes were the elusive 'M-Regions' which give rise to geomagnetic storms by their influence on the velocity pattern of the solar wind. Although coronal holes had been tentatively identified earlier on the basis of ground-based observations (Waldmeier, 1957) and low resolution X-ray pinhole and XUV heliograms (Russell and Pounds, 1966; Austin *et al.*, 1967), they attracted little interest primarily because they were not clearly defined entities. However, three different groups reintroduced the subject almost simultaneously (Altschuler *et al.*, 1972; Munro and Withbroe, 1972; Krieger *et al.*, 1973) just prior to Skylab. The subsequent high resolution X-ray images obtained during Skylab ignited a general interest in the study of these indicators of the large scale structure of the solar magnetic field. Several categories, based on their heliographic location, are known each having a characteristic relationship to the solar cycle; for instance, the recurrent equatorial holes are present only during the declining phase of the solar cycle, while the polar holes are always present except perhaps during solar maximum. Although coronal holes can now be identified from ground-based observations, notably the He 10830 line, the reconfiguration of the magnetic field which occurs as their boundaries expand or recede is best studied with X-ray or XUV observations.

The X-ray observations have also shed light on the small scale structure of the magnetic field following the observation and classification of the features known

as X-ray Bright Points (XBP). XBPs are small, compact, short-lived, magnetically bipolar regions whose size and lifetime spectra blend into the corresponding active region spectra.

Their major significance results from their identification as sources of emerging magnetic flux. The relationship of XBPs to the general solar field is still not understood. However what is clear is that the emerging magnetic flux associated with XBPs differs radically from that associated with active regions in at least two ways. The first, discovered from the Skylab observations, is that the XBP are distributed more or less uniformly over the solar surface in sharp contrast to the active regions which are limited to the equatorial band (Golub et al., 1974, 1975). The observations do suggest that there are two components to the bright point distribution, one associated with the active region latitudes and the second uniformly distributed over the entire disk.

The second difference is their variation with the solar cycle which appears to run counter to the well-known sunspot cycle.

### 3. THE SOLAR CYCLE VARIATION

A basic limitation of the Skylab study was that it covered only a short period (8 months) of the solar cycle and consequently the conclusions drawn from this period may not be typical of solar conditions throughout the 11-year cycle. To augment these data, four sounding rockets have been flown since Skylab and in particular two flights were made in September and November 1976 close to solar minimum. On both these occasions the X-ray images revealed that the corona was composed of low-lying weakly emitting structures, interspersed with very large numbers of XBPs. Coronal holes were visible at both poles, however, there was no evidence of the large equatorial holes which were so characteristic of the declining phase.

The most obvious and striking difference was the large number of XBPs. In order to compare their number with those from the Skylab period, the relative efficiencies of the two rocket telescopes were evaluated and compared to the Skylab

telescope. Using these ratios the closest comparable rocket exposures were selected and were used to establish the bright point counts.

The major result of the investigation is shown in Figure 2 where the relative numbers of XBP in 1973 and 1976 are compared (Davis et al., 1977). The 124 daily averages from 1973 are plotted in the form of a histogram showing the frequency of occurrence of each number count. The histogram approximates to a Gaussian distribution, even though there were persistent non-random variations during the eight rotations observed, and the mean (39) and its standard deviation ( $\pm 3$ ) have been used to characterize the distribution. The values observed in 1976 are indicated by arrows and lie well outside the range of values recorded in 1973.

After scaling the 1976 values are  $90 \pm 8$  and  $75 \pm 9$ . They are both consistent with a substantial increase in the number of bright points occurring between 1973 and 1976. In fact the average of the two 1976 observations, 83, is 110 percent higher than the combined average, 39, of the 1973 data. Under the assumption that the data from both 1973 and 1976 belongs to the same Gaussian frequency distribution, the probability that two random observations will result in the 1976 value is found to be 1 in  $5 \times 10^6$ . Even using the lower bounds for the 1976 observations, thus maximizing the probability, the chance of making the observations is still only 1 in  $2 \times 10^5$ . We realize that because of deviations from a Gaussian distribution these probabilities are not strictly true but even so the inescapable conclusion remains that the 1976 data belong to a different frequency distribution with a higher mean value.

In Figure 3 we show the latitude distribution of XBP seen on the two 1976 images, compared with the 1973 average. The 1976 data show much larger error bars since only two photographs were available. However, it is clear from the figure that there were more XBP at all latitudes in 1976 than in 1973, with the possible exception of the extreme polar latitudes where the statistical sample is small. Thus it is clear that the emergence of small-scale magnetic flux regions at solar minimum does not follow the pattern set by the larger active regions. Unfortunately, further details of the behavior within restricted latitude intervals cannot be deduced because of the limited statistics of the data sample.

The increase in the number of XBP is even more significant when compared to the changes in the other indices of solar activity between 1973 and 1976. For instance the average relative sunspot number,  $R_z$ , for the Skylab period, May to November 1973, was 35 whereas the index for January to December 1976 averaged 13. Thus while the sunspot number has declined by a factor of 3, the number of XBPs has increased by over a factor of 2. The implication of this result is that XBPs vary out of phase with the solar cycle as measured by the usual indicators of activity.

To explore this possibility further we have reexamined data from the older rocket flights going back to 1970 and the two other post-Skylab flights. Following a careful calibration program to compensate for the instrumental differences, a consistent pattern of anticorrelation between sunspot number and bright point count is found. The data are summarized in Figure 4 where we show the variation with time of  $R_z$  and XBP number, both normalized to maximum values of 100, over the last sunspot cycle. It is apparent that the variation in XBP count is close to  $180^\circ$  out of phase with  $R_z$ . This demonstrates that XBP must represent magnetic flux which emerges independently of the active regions. For if the emergence of XBPs was somehow associated with the emergence of the larger active regions (e.g., if the XBP represented either precursors or remnants of the larger active regions), then the bright point count could not lead or lag  $R_z$  by much more than the characteristic lifetime of the flux associated with the active regions ( $\sim 6$  months). Instead the observed phase lag is closer to 6 years. Therefore, in order to determine the total magnetic flux emerging at the solar surface at any time, it is necessary to sum the magnetic flux represented by the XBPs with that represented by the active regions.

#### 4. IMPROTANCE OF THE RESULT

The last conclusion, that in order to determine the total magnetic flux emerging from the solar surface, it is necessary to sum both the XBP and active region components, provides the significance to the observations. For now, the possibility exists that the amount of magnetic flux emerging throughout the cycle is constant or even that the total increases at solar minimum.

Comparison of the X-ray data with high resolution magnetograms shows that on average XBP emerge with  $2 - 3 \times 10^{19}$  Mx of flux (Harvey et al., 1975; Golub et al., 1977). Although this is more than an order of magnitude less than for active regions, because of their large number, XBP contributed 80 percent of the total of all emerging magnetic flux at the time of the Skylab observations. Under the assumptions that the XBPs seen in all of the rocket flights are physically the same so that the characteristic value of  $3 \times 10^{19}$  M<sub>x</sub> per bright point can be used for all the data, and that the sunspot index R<sub>z</sub> may be used as a relative indicator of the amount of flux emerging in the form of active regions throughout the solar cycle, it is possible to proceed to estimate the relative contributions of XBP and active regions to the total magnetic flux spectrum of the sun during the period 1970 to 1978. By taking the 1973 fraction of 80 percent as a base, we estimate that ~40 percent of the total magnetic flux in 1970 emerged in the form of XBP. The contribution of XBPs to the total reached a peak of ~95 percent in 1976 and has since declined to about 70 percent in early 1978. From this analysis we conclude that XBPs make a substantial contribution to the total emerging magnetic flux spectrum throughout the entire solar cycle and are the dominant contributors throughout the declining, minimum and ascending phases.

## 5. CONCLUSIONS

High resolution X-ray images of the solar corona contribute to the study of the solar magnetic field by revealing, in a unique manner, the topology of the extension of that field into the corona. It is extremely difficult, if not impossible, to obtain this information in other ways, for instance by extrapolating the measurements of the photospheric magnetic field because this requires theoretical modelling, e.g., potential field calculations, which results in, at best, an approximation to the real situation.

The X-ray images, although recorded only during brief intervals over the last decade, have revealed two new facets of the behavior of the solar magnetic field which must be explained in any comprehensive theory of its origin and variability. In particular it has been learned that XBPs represent a dominant feature of the

emerging magnetic flux spectrum through the majority of the solar cycle. In fact they display a counter cycle to the better known sunspot cycle and at this time the relative importance of the two cycles to the actual description of the solar dynamo is not known. Because of the limited number of data samples, the statistics of the observations over a solar cycle are not high and other contributions of XBPs to the complete picture of the solar magnetic field almost certainly remain to be discovered. An example is their latitude distribution which is known to differ markedly from that of active regions but whose possible cyclical variation is completely unknown.

In this context the SCADM mission presents a unique and valuable opportunity to obtain an uninterrupted, long duration sample of coronal observations. In the recording of these data, the value of high sensitivity, high resolution observations cannot be overemphasized. For although both XBPs and coronal holes are visible, in retrospect, in the X-ray images made prior to 1970 their importance was not realized at the time because the lack of definition in the observations did not allow a positive and unambiguous identification to be made. Since the coronal observations will still be to some extent exploratory, the preliminary planning for the SCADM spacecraft must reflect the requirement for imaging data with comparable quality to those of current rocket programs.

#### ACKNOWLEDGMENTS

The work described in this report has been supported in part by NASA under contracts NAS2-8683, NAS5-25496, and NAS8-27758.

#### REFERENCES

- Altschuler, M. D., Trotter, D.E., and Orrall, F.Q.: Solar Phys. 26, 354, 1972.
- Austin, W.E., Purcell, J.D., Snider, C.B., Tousey, R., and Widing, K.G.:  
Space Research VII, 1252, 1966.
- Davis, J.M., Golub, L., and Krieger, A.S.: Astrophys. J. 214, L141, 1977.
- Golub, L., Krieger, A.S., Silk, J.K., Timothy, A.F., and Vaiana, G.S.: Astro-  
phys. J. 189, L93, 1974.
- Golub, L., Krieger, A.S., and Vaiana, G.S.: Solar Phys. 42, 131, 1975.
- Golub, L., Harvey, J.W., Krieger, A.S., and Vaiana, G.S.: Solar Phys. 53, 111,  
1977.

Harvey, K. L., Harvey, J. W., and Martin, S. F.: Solar Phys. 40, 87, 1975.

Krieger, A. S., Timothy, A. F., and Roelof, E. C.: Solar Phys. 29, 505, 1973.

Munro, R. H. and Withbroe, G. L.: Astrophys. J. 176, 511, 1972.

Russell, P. C. and Pounds, K. A.: Nature 109, 490, 1966.

Waldmeier, M.: Die Sonnenkorona 2, Verlag Birkhauser, Basel, 1957.



7 March 1970



24 November 1970



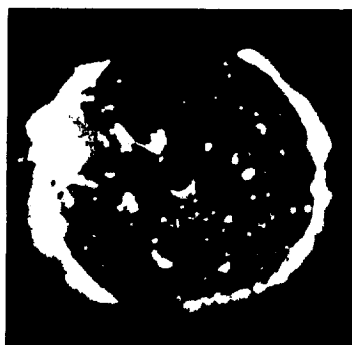
8 March 1973



1 June 1973



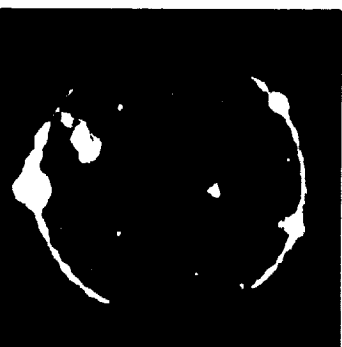
2 September 1973



14 November 1973



27 June 1974



17 November 1976



31 January 1978

Figure 1. Coronal X-ray observations during the period 1970-1978. A collection of images from sounding rockets and Skylab.

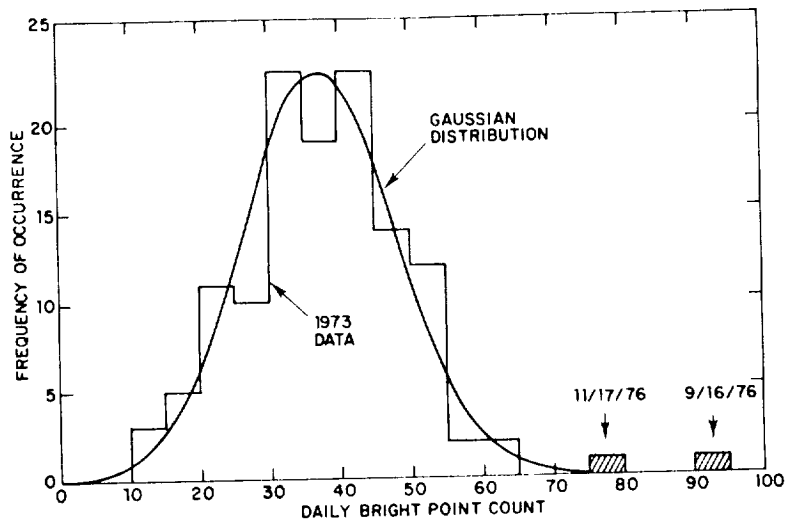


Figure 2. Daily X-ray bright point counts. The curve is a Gaussian distribution fitted to the 1973 data.

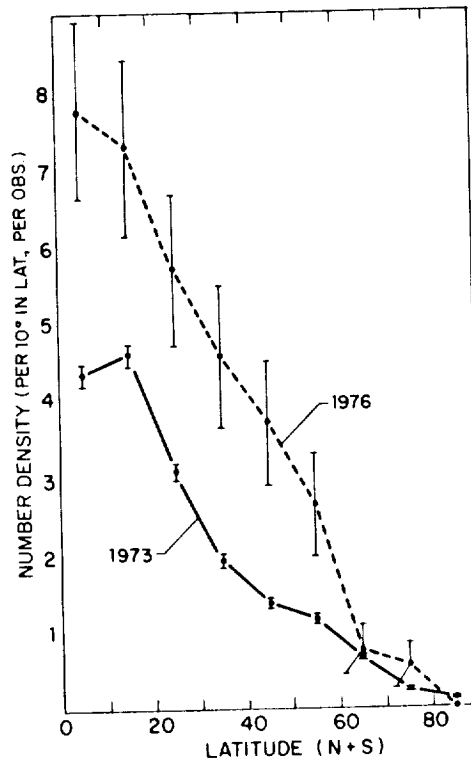


Figure 3. The latitude distribution of X-ray bright points in 1973 and 1976.

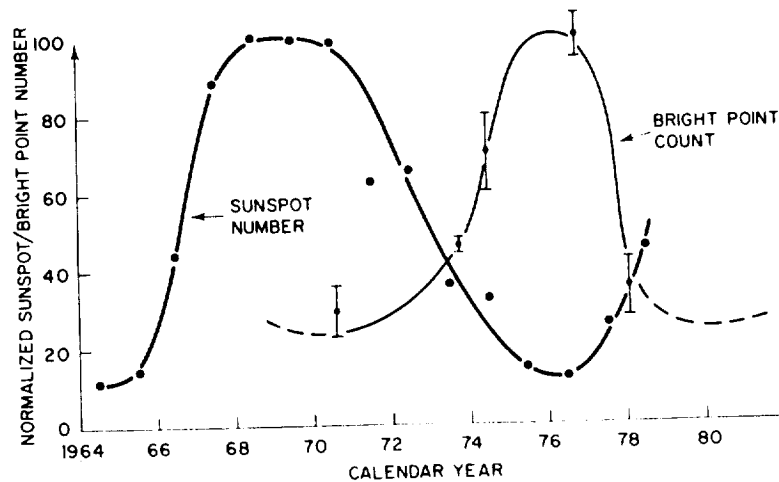


Figure 4. Variation of the number of X-ray bright points with the solar cycle.



4.3 Quest for Ultrahigh Resolution in X-Ray Optics

John M. Davis, Allen S. Krieger, J. Kevin Silk and Richard C. Chase

American Science and Engineering, Inc.  
Cambridge, Massachusetts 02139

ORIGINAL PAGE IS  
OF POOR QUALITY

1  
2  
3  
4  
5  
6  
7  
8  
9  
10  
11  
12  
13  
14  
15  
16  
17  
18  
19  
20  
21  
22  
23  
24  
25  
26  
27  
28  
29  
30  
31  
32  
33  
34  
35  
36  
37  
38  
39  
40  
41  
42  
43  
44  
45  
46  
47  
48  
49  
50  
51  
52  
53  
54  
55  
56  
57  
58  
59  
60  
61  
62  
63  
64  
65  
66  
67  
68  
69  
70  
71  
72  
73  
74  
75  
76  
77  
78  
79  
80  
81  
82  
83  
84  
85  
86  
87  
88  
89  
90  
91  
92  
93  
94  
95  
96  
97  
98  
99  
100

## Quest for ultrahigh resolution in x-ray optics

John M. Davis, Allen S. Krieger, J. Kevin Silk, and Richard C. Chase

American Science and Engineering, Inc.  
955 Massachusetts Avenue  
Cambridge, Massachusetts 02139

### Abstract

A program of solar X-ray astronomy using grazing incidence optics has culminated in X-ray images of the corona having one arc second spatial resolution. These images have demonstrated that in general X-ray optics can be fabricated to their specifications and can provide the level of resolution for which they are designed. Several aspects of these programs relating to the performance of X-ray optics in regard to resolution, including the point response function, the variation of resolution with off-axis position and the recognition that nearly all solar X-ray images have been film limited, are discussed. By extending the experience gained on this and other programs it is clearly possible to design and fabricate X-ray optics with sub-arc second resolution. The performance required to meet the scientific objectives for the remainder of the century are discussed in relation to AXIO, an Advanced X-Ray Imaging Observatory for solar observations which is proposed for flight on the space shuttle. Several configurations of AXIO are described, each of which would be a major step in the quest for ultra-high resolution observations.

### Introduction

The majority of the contributions to this workshop have described the application of grazing incidence optics to celestial X-ray astronomy. Although this is not surprising, in light of the dramatic results from the HEAO-2/Einstein mission, it should not be allowed to completely overshadow either the achievements or the requirements of that branch of X-ray astronomy devoted to the study of the solar corona. Our current abilities in this field represent the culmination of fifteen to twenty years of experimentation at several laboratories throughout the United States and Europe. The scientific results from these studies have suggested that the understanding and detailed interpretation of the physics of the corona will require observations with a much higher spatial resolution than has been achieved to date; which fact provides the incentive for this paper.

Any discussion of the design and performance specifications of grazing incidence telescopes must recognize that there exist significant differences in the requirements placed on the observations by the objectives of solar and celestial X-ray astronomy. These differences are reflected in the way the performance of the instruments is described. Solar X-ray images are views of a highly structured object of considerable extent. Point to point variations of intensity within the image, which after analysis can be converted into electron temperature, density and pressure measurements, are important. In contrast celestial observations are frequently limited to the study of one or more, but never very many, point sources within the field of view, whose internal structure is unresolved. Consequently for solar observations, the requirement of high spatial resolution reflects the more general optical application in which the performance of an imaging system is represented by its modulation transfer function (MTF). In contrast the advantage of high resolution in celestial imaging systems is to improve the sensitivity of the instrument by concentrating the flux from a particular object within a single image element. This improves the sensitivity by increasing the signal to noise ratio of the observation thus allowing the detection of fainter and presumably more distant and hence cosmologically interesting objects. In the celestial case it is convenient to describe the performance of the grazing incidence mirror in terms of the RMS blur circle radius of the image of a point source, since this indicates the efficiency with which the reflected energy is concentrated in the image plane.

Since the objective in solar physics is to distinguish discrete structures, identify their boundaries, describe their geometry and differentiate between the plasma conditions inside and outside these structures, it is possible to define the level of resolution achieved in practice by reference to the observations. The Skylab telescopes and the mirror used in our current rocket program produce images having a realistic resolution when defined in this way of a few (2-5) arc seconds. However it must be realized that the observed resolution of these instruments is the result of folding together the transfer functions of both the optics and the detector. The latter has usually been photographic film and, as we will show later, all the recent solar images, but one, recorded to date have been limited by the film rather than by the optics. This type of performance, i.e., the ability to resolve structures at the 2-5 arc second level will be referred to as high resolution. The term ultra-high will refer to roughly an order of magnitude improvement over existing instruments, that is, to sub-arc second resolution with limiting values of 0.1 to 0.2 arc second.

We believe that this level of resolution is necessary if further significant advances in our understanding of coronal physics are to be made. Moreover, we are confident that the technology now exists, not only for the fabrication of ultra-high performance grazing incidence mirrors, but also with the development of the space shuttle to carry these large instruments into orbit. Together these facts make the serious consideration of the next generation of solar X-ray telescopes both meaningful and worthwhile.

### Characterizing the Performance of Grazing Incidence Optics

#### The Point Response Function

The performance of X-ray grazing incidence optics is usually described in terms of two quantities: the point response function (PRF) of the mirror, and the variation of the RMS blur circle radius as a function of off-axis position. The PRF describes the fraction of the reflected intensity which falls within a given radius of the central maximum and it is determined experimentally. In general the PRF can be considered as the sum of two separate distributions which are composed of the specularly reflected rays and of the surface scattered rays respectively. The specularly reflected component forms a narrow central peak which is characterized by its HWHM. It is a measure of the accuracy of the figure of the mirror surfaces and its magnitude can be directly related to their tolerances. The scattered distribution tends to be broad and flat and it can be described by the half power radius, i.e., by the radius within which 50 percent of the reflected energy is contained. The presence of the broad 'wings' of the scattering distribution, which extend out to at least 15 arc minutes, means that the power in the image is spread out over a large angular area. These terms can be demonstrated by the comparison of the PRFs of the Skylab and rocket mirrors which are shown in Figure 1.

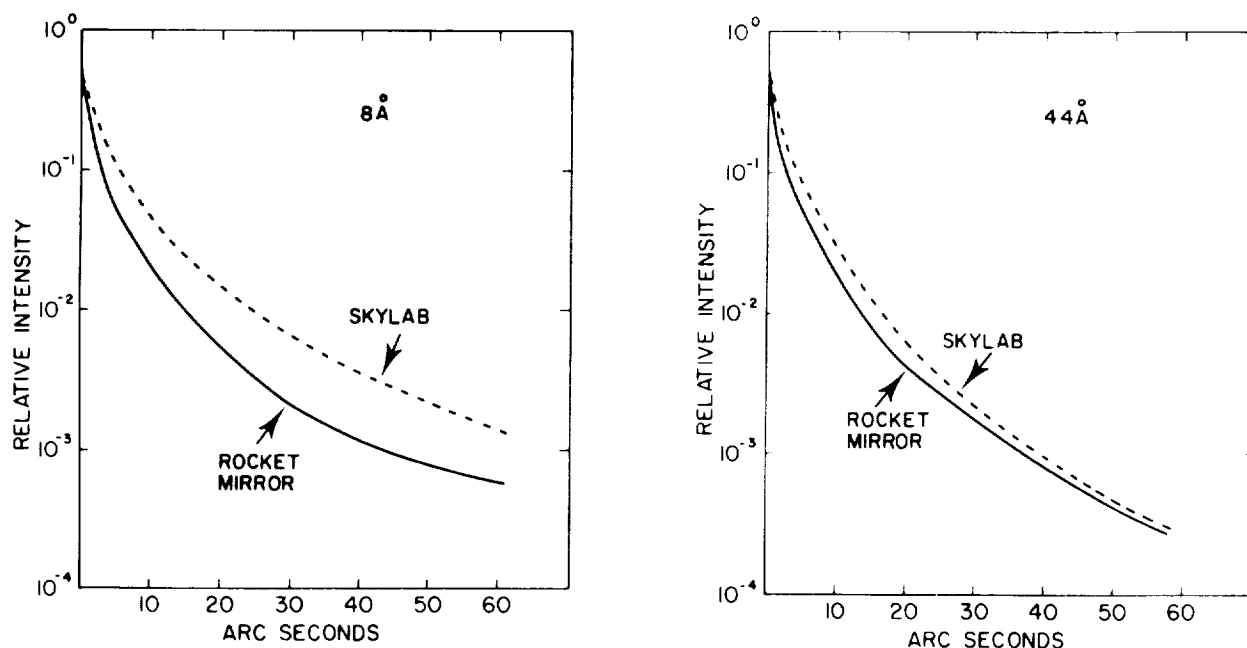


Fig. 1. A comparison of the inner region of the PRFs of the rocket and Skylab mirrors at 8 and 44 Å.

The Skylab mirrors<sup>(1)</sup> are a nested pair of Wolter Type I paraboloid-hyperboloids. They were fabricated from beryllium with superpolished<sup>(2)</sup> electroless nickel (Kanigen) reflecting surfaces. The rocket mirror is also a Wolter Type I design, but it has Wolter Schwarzschild surfaces which, although more difficult to fabricate, were chosen over the more normal paraboloid-hyperboloid surfaces since they satisfy the Abbé sine condition and therefore eliminate the coma aberration for paraxial rays<sup>(3)</sup>. It was chosen to fabricate the mirror from fused silica on the basis of a test program which evaluated the scattering of X-rays from highly polished flats. The results of this program indicated that fused silica was superior to all other metals and glasses available at that time.

The HWHM of the rocket mirror PRF is approximately 1 arc second while the corresponding value for the Skylab mirror is roughly twice as large. The half power radii are respectively 31 and 48 arc seconds at 8 Å and 18 arc seconds for both mirrors at 44 Å. Inspection of the data recorded in Figure 1 shows that the rocket mirror PRFs have very little dependence on wavelength and further that the PRFs of the two mirrors are quite

similar at 44 Å. These data can be interpreted as an indication that the surface roughness for the Skylab mirror is small compared to 44 Å but not to 8 Å while the surface roughness of the rocket mirror which is beginning to affect the PRF at 8 Å may be of this order.

Both these mirrors were fabricated over seven years ago and represent a rather early stage of surface polishing technology. In particular our ability to measure surface smoothness was limited and this was reflected in the mirror specification for surface smoothness. In contrast the HEAO-2 mirrors<sup>(4)</sup> are the latest stage in this technology and demonstrate the improvements in our ability not only to make mirrors of very large size but more importantly with very smooth reflecting surfaces. By comparison the half power radii for 8 and 44 Å radiation are respectively 6 and 4 arc seconds<sup>(5)</sup>. These values reflect the average smoothness for all the mirrors in the nested set and the surface achieved on the smoothest mirror would be adequate for the next generation sub-arc second telescope.

### The Off-Axis Resolution of Grazing Incidence Optics

In order to introduce the topic of the off-axis response of grazing incidence mirrors we will first discuss a method we have developed for determining the location of the focal plane. In the past modified Focault tests, Hartmann cameras or other techniques which determine the focus for on-axis rays have been used. However, the focal plane of an X-ray mirror is not flat but is curved and when the objective is to image a broad source, such as the sun, an adjustment has to be made from the measured position to compensate for the different focus of the off-axis rays. In general the optimum focus for an on-axis ray is located behind the same position for an off-axis ray (Figure 2). To overcome the need for an adjustment we have developed a simple procedure which allows us to specify the optimum focal plane for a broad source.

The procedure uses a star pattern of resolution targets. Each block in the star contains 5 groups (II through VI) of a USAF resolution target. Each group contains 6 patterns containing 3 vertical and 3 horizontal bars with each pattern reduced in size by  $6\sqrt{2}$  from its predecessor. A set of focus plates is taken with the flight camera as its position is varied along the optical axis and the resulting images are observed with a microscope. Rather than obtaining the best focal position by inspection, we have placed the procedure on a numerical basis by calculating a Figure of Merit (FoM) which reflects the resolution across the field of view.

The FoM is determined in the following way:

- (i) Each pattern in each group is assigned a numerical value starting with II-1, which is set equal to unity, and increasing by one for each succeeding (i.e., decreasing) pattern. Thus,

$$\begin{aligned} \text{II-1} &= 1 \\ \text{II-2} &= 2 \\ &\dots \\ \text{II-6} &= 6 \\ \text{III-1} &= 7, \text{ etc.} \end{aligned}$$

i.e., the patterns with better resolution are assigned higher numbers.

- (ii) Three exposures of the star pattern are taken at each focal position to eliminate (or minimize) the effects of Schlieren due to air turbulence. The smallest horizontal and vertical patterns, which are resolvable in each exposure, are recorded for each position in the star. The average of the smallest horizontal and vertical pattern resolved is computed and recorded for each position (Figure 3).
- (iii) The sum of the averages from each position in the star is recorded and is used as an indicator or FoM for the resolution across the field of view at that focal position.

A typical set of data obtained with the fused silica rocket mirror is shown in Figure 4. The two sets of points correspond to the orthogonal directions in the focal plane formed by the star pattern. The data shows a

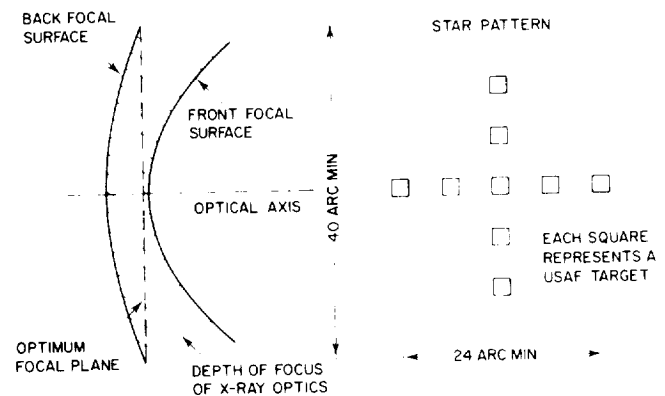


Fig. 2. Schematic representation of the mirror focal plane and the star pattern used in its location.

Focal Position	Star Position										Figure of Merit
	1		2		3		4		5		
	H	V	H	V	H	V	H	V	H	V	
550	IV-5	IV-3	IV-4	IV-3	IV-4	IV-4	IV-3	IV-4	IV-3	IV-2	81 ← Sum of averages
	IV-4	IV-4	IV-4	IV-3	IV-5	IV-3	IV-4	IV-3	IV-4	IV-4	
	IV-4	IV-4	IV-4	IV-4	IV-5	IV-4	IV-4	IV-4	IV-4	IV-4	
	16.5		16		16.5		16		16		← average within each position

$$\frac{1}{2}(IV-5 + IV-4) = \frac{1}{2}(17 + 16) = 16.5$$

H & V are the horizontal and vertical sets within a pattern

Fig. 3. An example of the data used in the determination of the Figure of Merit.

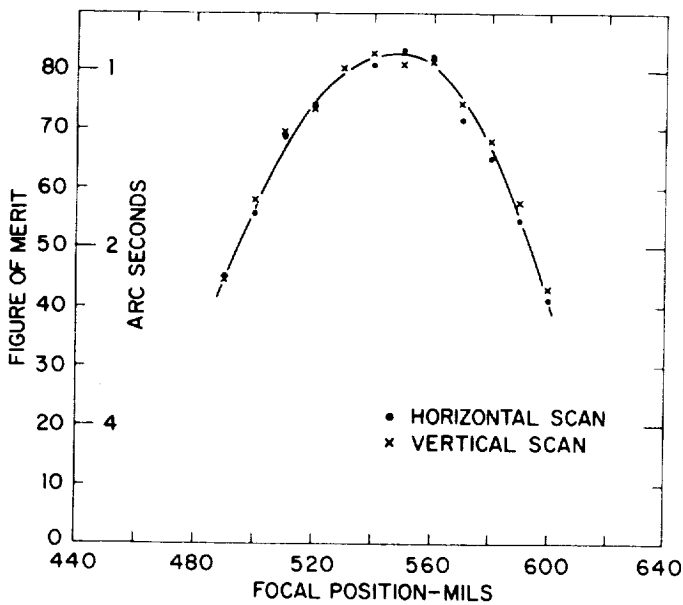


Fig. 4. Experimental data showing the location of the focal plane by the figure of merit method.

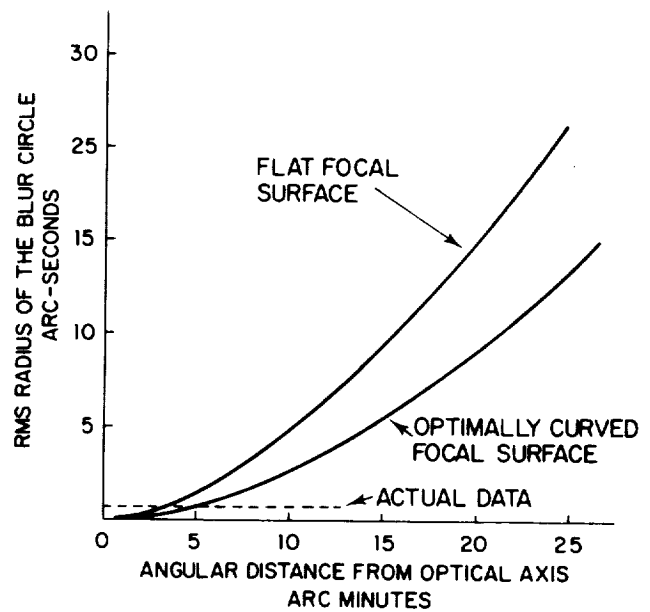


Fig. 5. The variation of the RMS blur circle radius with off-axis position. The broken line represents the observed resolution using USAF resolution charts.

plateau where the average resolution is better than 1 arc second (FoM > 80) which we interpret as the effective depth of field. The 1 arc second level of resolution at the plateau is predominantly a function of the recording medium for, if a finer grain film is used, the effective resolution improves to close to 0.5 arc second (FoM = 116) which is near the diffraction limit for visible light for this mirror.

Although we believe that this is a useful method for determining the focal plane of grazing incidence mirrors, we have introduced it to illustrate a different point; namely, the off-axis response of the mirror or the variation of resolution with distance from the optical axis. In general our knowledge of the off-axis performance of grazing incidence mirrors is obtained from ray-tracing calculations. These calculations are based on purely geometrical optics and make no allowance for diffraction effects or for the X-ray PRF. They describe the off-axis response in terms of the RMS radius of the blur circle formed of a point object. In general this radius increases monotonically with the angular distance of the source from the optical axis for both flat and curved focal surfaces. However, when we analyze the focus plates, as described above, it is immediately apparent

that the variation of resolution with off-axis position is far less severe than predicted by the calculations of the RMS blur circle radius. In fact out to 12 arc minutes no fall off in resolution is observed for the rocket mirror while the ray tracings indicate that the RMS radius has increased from essentially zero to 4 arc seconds in the best case (Figure 5).

The conclusion that we draw from this result is that the RMS blur circle radius is a poor indicator of actual mirror performance when applied to angular resolution. Consequently the various figures which can be found in the literature describing the off-axis performance of mirrors are probably misleading when considered in the context of solar observations. A more serious consideration is their use in those solar applications which call for both high resolution and large collecting areas. To increase collecting area, for a fixed focal length, there are usually three options available, to increase the diameter of the mirror, to use nested sets, or to increase the length of the mirror element. When the application calls for high resolution over a wide field, the third option is usually rejected because of the loss in off-axis resolution predicted by the ray tracing programs. Our observations would suggest that this conclusion may be overly restrictive and we would be interested to learn of the experience of other groups in this area.

To conclude this section we would like to illustrate the two points that we have raised, namely that there is little degradation in image quality as one goes off-axis and secondly that most of the observations made to date have been limited by the film rather than by the optics and its corollary that the current generation of X-ray optics have in fact met their design goals of one arc second imaging, by using actual data recorded during a rocket flight. Figure 6 shows the solar X-ray corona on 31 January 1978 photographed with the fused silica rocket mirror. The box encloses a feature which has been tentatively identified as a flaring bright point. It is located a little over 14 arc minutes from sun center at which the optical axis of the telescope was directed. The two lower frames of Figure 6 are magnified views of the same region taken with different exposures and recorded on two different emulsions. The left hand frame was recorded on Eastman Kodak SO-212, the Skylab film. The effect of the grain noise is obvious and the feature is unresolved. However, in the right hand frame, which was recorded on Eastman Kodak SO-253, a fine grain holographic emulsion, the structure is clearly revealed as a single loop 12 arc seconds long and slightly in excess of 1 arc second wide. The photograph, which of course includes the effect of the PRF which is neglected in the ray tracing treatment, clearly demonstrates that even at relatively large angles from the optical axis the angular resolution of the mirror for X-rays is on the order of one second of arc. Note: Essentially the same conclusion can be drawn from the HEAO-2 calibration data which shows that the HWHM is essentially independent of off-axis position<sup>(5)</sup>.

#### The Scientific Rationale for Improved Resolution Imaging

Given the fact that our current observational capability is on the order of one arc second, we must ask the question: Are there valid scientific objectives that will justify the effort to improve the resolution of X-ray telescopes by an order magnitude? Clearly we believe the answer to this question is yes. During the last decade our knowledge of the solar corona has been vastly increased due, in large part, to observations made with grazing incidence optics in the soft X-ray region of the spectrum. The classical view of the corona, as uniform and symmetrical with a radially outward decreasing density which expanded and contracted with the solar cycle, has been replaced by a picture dominated by plasma filled magnetic loops of all dimensions down to the limit of resolution (Figure 7). Similarly the description of the physics of the corona, of its energy balance, of the method of its heating, of the mass exchange between it and the lower levels of the solar atmosphere and of the nature of the instabilities which give rise to solar flares and other transient phenomena, has evolved into an explanation of these phenomena within the framework of magnetic loops.

This change in perspective has developed in concert with improvements in the spatial resolution of X-ray telescopes and in particular as a result of the long duration observations obtained from Skylab. However, the latter were limited in general to a spatial resolution of a few arc seconds, except for certain objects which have very high contrast. Nor, because of the high level of scattering produced by the mirror surfaces, were the Skylab X-ray instruments well suited for distinguishing between subtle changes in intensity from adjacent image elements. For many of the more fundamental problems outlined above, this has proved to be a particularly severe limitation to the Skylab data.

Observationally the requirement is not simply to resolve loops, or other structures, of smaller and smaller size, but rather to resolve the internal structure of individual loops which are themselves of moderate dimensions. For instance typical active region loops have widths on the order of 5-30 arc seconds and lengths of 1-4 arc minutes. The Skylab telescopes, with their realistic resolution of something in excess of 3 arc seconds, had sufficient resolution to resolve these loops but were unable to unravel the characteristic structure of individual loops. In particular it has not proved possible to specify the radial variations of the plasma properties of loops. This question is crucial because the high transport coefficients along the direction of the magnetic field (i.e., along the loop) tend to smooth out longitudinal pressure and temperature variations. In contrast the magnetic field inhibits the transport properties perpendicular to the field and gradients can be

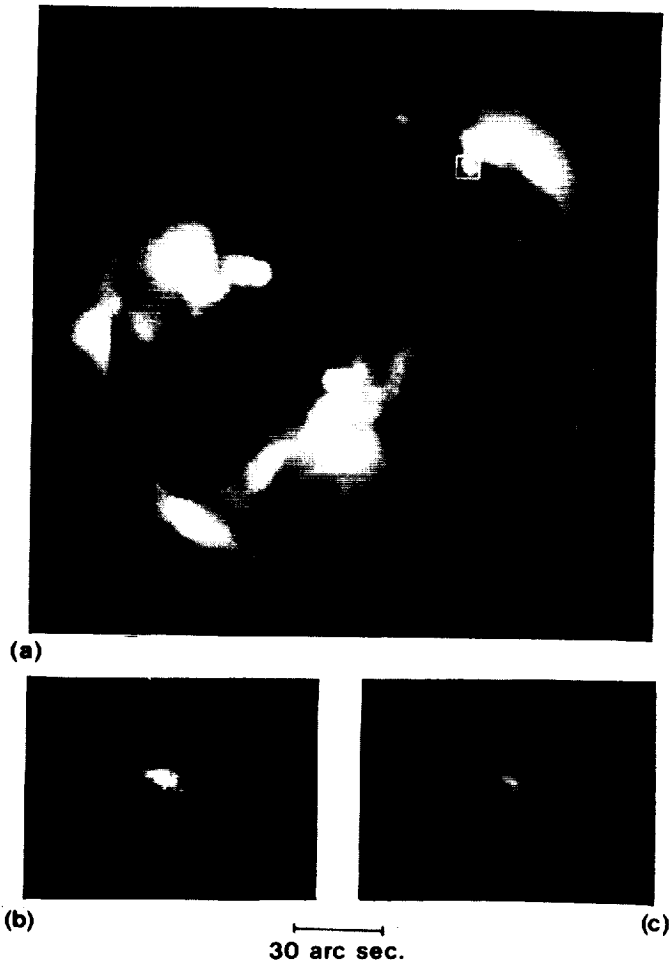


Fig. 6. The X-ray corona on 31 January 1978 showing the location of a flaring bright point (a). Magnification of the feature seen in different exposures shows the improvement in resolution between Eastman Kodak SO-212, the Skylab film (b) and the fine grain SO-253 (c). In the latter a single loop with a width slightly in excess of 1 arc sec and 12 arc sec long is clearly revealed.



Fig. 7. The X-ray corona on 8 March 1973 showing the predominance of loop-like structures throughout the corona. The magnified image shows the loops associated with one of the active regions. The loops are several arc minutes long and 15-25 arc sec wide. They are too narrow to have their radial structure clearly resolved at the 2-3 arc sec resolution level of this image.

established in this direction. Consequently the different models of loop heating can be characterized by their description of the variations that can be expected across the loop. For instance, does loop heating take place only in a thin surface layer which surrounds a cool core or are loops bundles of individual flux strands each with its own temperature and pressure regime? It is difficult to see how a rationale choice can be made between the various theoretical models without observations with much higher spatial resolution than is currently available.

A second fundamental and largely unexplored area deals with the stability of loops. Here the important question is why many loops remain relatively quiescent while others undergo large transient brightenings and flaring. Recent theoretical work indicates that the initial instabilities in loops are almost certainly the long wavelength macroscopic instabilities. The pressure, or temperature, perturbations corresponding to these instabilities will show up as brightness fluctuations at or below the arc second level.

An estimate of the time resolution required for the study of transient or flaring phenomena can be obtained from the time taken for a plasma disturbance moving at the coronal sound speed ( $2-3 \times 10^2 \text{ km s}^{-1}$ ) to cross one arc second, that is the distance over which independent determinations of the plasma characteristics can be made. Since this distance corresponds to  $\sim 700 \text{ km}$  at the center of the solar disk then a time resolution of 1 s or less is necessary. Further, since the small loops frequently found at the centers of flaring regions

have lengths on the order of 10 arc seconds, it is obvious that a combination of both high spatial and temporal resolution is essential if the propagation of disturbances through this type of structure is to be studied. A recent review by Wentzel<sup>(6)</sup> provides a more detailed discussion of the current problems of coronal physics with particular emphasis on coronal loops.

#### The Next Generation of X-Ray Imaging Instruments for Solar Observations

The observational goals that would justify the development of a new generation instrument are:

- (i) A real spatial resolution of less than half an arc second. In light of the earlier discussion, this resolution is the resultant of folding together the MTFs of both the optics and the detector; and
- (ii) A temporal resolution on the order of one second.

The first stage in achieving this goal would be the fabrication of a very high quality grazing incidence mirror and such a program forms the basis of our proposal for AXIO - An Advanced X-Ray Imaging Observatory.

#### An Advanced X-Ray Imaging Observatory

Our concept of AXIO is based on a single Wolter Type I grazing incidence mirror with Wolter Schwarzschild reflecting surfaces. We believe that only minor advances in current technology are required to permit the fabrication of the reflecting surfaces with sufficient accuracy to provide a resolving power of better than 0.2 arc seconds. The instrument concept provides for a group of four interchangeable focal plane detectors which would be selected for specific scientific objectives. An initial configuration, designed specifically for imaging observations would consist of pairs of 70 mm photographic cameras for ultra-high spatial resolution and electronic cameras for high time resolution observations. Many other configurations are possible and would undoubtedly be implemented in the expected 20-year operational life of the mirror and one rather exciting example is discussed later.

AXIO is projected as a candidate for flight on the Space Shuttle where it would be mounted to the instrument pointing system (IPS). Consequently it has been sized to be contained within a cylindrical volume roughly 7 m long and 1 m in diameter and weighing approximately 1000 kg. This size was chosen specifically to allow AXIO to be flown as part of a solar instrument cluster. For although AXIO is designed to operate alone the range of problems which it is proposed to study would benefit from the simultaneous acquisition of data by other solar instruments, many of which are already planned for flight.

An indication of the improvements in observational capability that AXIO will provide can be found by reference to Table I. In this table the various instrument parameters are compared with those of the Skylab telescope and in general reflect an order of magnitude improvement.

We have chosen a single mirror for AXIO rather than a nested set for three main reasons:

- (i) In a nested set the final imaging properties tend to be governed by the worst mirror in the set rather than by the best.
- (ii) The mechanics of nesting large mirror assemblies inevitably leads to some degradation in image quality arising from distortions introduced in the mounting plane, slight differences in focal lengths, etc., and these degradations are likely to be relatively more severe for large, ultra-high resolution mirrors.
- (iii) For solar observations the requirement for very large collecting areas is not quite as overriding as it is for celestial astronomy.

Obviously a single mirror design of rather modest dimensions, as AXIO is, will also be less expensive to fabricate than, for instance, the larger and more mechanically complex nested assembly proposed for the Advanced X-Ray Astrophysical Facility (AXAF). However, even if cost were not a consideration, for those applications where ultra-high resolution is of paramount importance we believe that the single mirror approach is the best solution.

#### The AXIO Mirror Fabrication Tolerances

The goal of sub-arc-second resolution for the AXIO mirrors can be met with carefully figured and very smooth reflecting surfaces. The tolerances on the surface figure are generally tighter than those specified for

**TABLE I INSTRUMENT PARAMETERS**  
**A Comparison Between AXIO and Skylab**

	<u>AXIO</u>	<u>Skylab</u>
Wavelength Range	6 - 300 Å	2 - 60 Å
Spectral Resolution	Broadband 10 ranges	Broadband 6 ranges
Field of View	40 x 40 (arc min) <sup>2</sup>	48 x 48 (arc min) <sup>2</sup>
<u>X-Ray Mirrors</u>		
Figure	Wolter Schwarzschild	Paraboloid-Hyperboloid
Material	Fused Silica	Nickel Coated Beryllium
Diameter	80 cm	30 cm and 23 cm nested pair
Effective Collecting Area	175 cm <sup>2</sup>	20 cm <sup>2</sup>
Focal Length	475 cm	213 cm
Plate Scale	23 microns (arc sec) <sup>-1</sup>	10 microns (arc sec) <sup>-1</sup>
Solar Image Size	4.4 cm	2.0 cm
Resolving Power (X-ray)	0.2 arc sec	2 arc sec
Diffraction Limit 5600 Å	0.1 arc sec	0.4 arc sec
20 Å	4 x 10 <sup>-4</sup> arc sec	2 x 10 <sup>-3</sup> arc sec
Point Response Function (FWHM)	0.5 arc sec	3.4 arc sec
<u>Focal Plane Detectors</u>		
<u>Film</u>		
Type (Eastman Kodak)	3414	SO-212
Spatial Frequency 20% MTF	9 cycles (arc sec) <sup>-1</sup>	1 cycle (arc sec) <sup>-1</sup>
Exposure Times	1/4, 1, 4, 16, 64, 256 sec	1/64, 1/16, 1/4, 1, 4, 16, 64, 256 sec
Time Resolution	0.5 sec	6.5 sec
<u>Photoelectric</u>		
Types	Microchannel Plate & CCD	--
Pixel Center to Center Spacing	15 microns (0.65 arc sec)	--
Wavelength Range	6 - 300 Å	--
Spectral Resolution	Broadband 4 ranges	--
Time Resolution		--
for 4 x 4 arc min field	1 sec (for data rate of 1 M bits s <sup>-1</sup> )	--
for 40 x 40 arc min field	15 sec (for data rate of 1 M bits s <sup>-1</sup> )	--

the HEAO-2 mirrors by approximately a factor of 2. Not surprisingly they are very similar to the tolerances proposed for the AXAF mirrors<sup>(5)</sup>. However the latter are physically larger and consist of a nested set of mirrors and consequently in assessing the ultimate resolution of the AXAF mirrors the tolerances which describe the achievement of confocality between the individual mirrors of the set have to be included.

In general the fabrication methods that were used for the HEAO mirrors will be adequate to achieve the specifications required for AXIO. However, the in-process metrology must be improved since the current limitations in our ability to figure very accurate surfaces, is not in actually figuring the surface but rather in knowing when the required figure has been achieved. In this respect we believe that a laser scanning technique developed for the fabrication of a high resolution X-ray microscope could be adapted successfully to the metrology of the AXIO mirrors. The technique is capable of measuring displacements of less than one microinch or slopes of less than one microinch per inch in real time and without the removal of the piece under fabrication from its production fixture. The tolerances on the microscope figure were in general tighter than required by AXIO and its successful fabrication<sup>(7)</sup> demonstrates the soundness of the basic concepts and gives us confidence that the tolerances for the larger AXIO mirror can be achieved.

The tolerances on the mirror surfaces required to achieve AXIO's stated goal are shown in Table II where they are compared with the specifications for the HEAO-2 mirrors. Definitions of these tolerances can be found in the description of AXAF presented by Zombeck<sup>(5)</sup> at this conference. It is more instructive to compare the AXIO requirements with the tolerances actually achieved on HEAO-2. From this comparison it can be seen that

**TABLE II MIRROR TOLERANCES\***  
**A Comparison Between AXIO and HEAO-2**

<u>Tolerance</u>	HEAO-2		AXIO	
	<u>Specification</u>	<u>Achieved</u>	<u>Specification</u>	<u>Design Goal</u>
1. Out of Roundness $\Delta R = (R_{\max} - R_{\min})$	$200 \times 10^{-6}$	$40 \times 10^{-6}$	$100 \times 10^{-6}$	--
2. $\Delta (\Delta R)$	$50 \times 10^{-6}$	$43 \times 10^{-6}$	$20 \times 10^{-6}$	$8 \times 10^{-6}$
3. $\overline{\Delta R}$	$250 \times 10^{-6}$		$250 \times 10^{-6}$	--
4. $\overline{\Delta R} (\phi)$ per inch of Circumference	$\pm 25 \times 10^{-6}$	$5 \times 10^{-6}$	$\pm 10 \times 10^{-6}$	$\pm 5 \times 10^{-6}$
5. Sagittal Depth	$\pm 5 \times 10^{-6}$	$\pm 3 \times 10^{-6}$	$\pm 3 \times 10^{-6}$	--
6. $\Delta$ Slope per Axial Length of One Inch	$\pm 3 \times 10^{-6}$	$\pm 4 \times 10^{-6}$	$\pm 3 \times 10^{-6}$	$\pm 0.5 \times 10^{-6}$
7. Surface Finish RMS Roughness	$30 \text{ \AA}$	$14-25 \text{ \AA}$	$20 \text{ \AA}$	$10 \text{ \AA}$

\* All specifications are in inches unless otherwise stated.

the major problem area is the axial slope error ( $\Delta$  slope per axial length). However it is precisely this tolerance that the laser scanning method was developed to measure. Since with its use we have demonstrated a capability to figure and measure surface slopes to better than one microinch per inch we feel confident that the AXIO design tolerance can be met.

Finally the surface smoothness actually achieved for several of the HEAO mirrors is better than the required specification for AXIO and very close to the design goal. The HEAO mirrors were finished using the submerged polish technique and, provided that sufficient time is available for final polishing, this technique appears to be adequate to achieve our goals.

In concluding this section we would like to reiterate the point that the achievement of the fine tolerances required by AXIO lies not so much in improvement of the fabrication techniques themselves, but rather in the in-process metrology which must be capable of monitoring the progress in near real time.

#### Expected Performance

To visualize the improvement in the observations that we expect to obtain with the AXIO system, we have compared several indicators of its predicted performance with the known performance of the Skylab telescope. The two characteristics that we will compare here are the PRF, which is the ultimate indicator of resolution and the ERF or edge response function which demonstrates how well the system, i.e., the optics and the detector can reproduce an infinitely sharp brightness edge.

The central maximum of the AXIO PRF has been calculated on the basis of the tolerances placed on the surface figure while the wings are based on the achieved scattering function of the HEAO mirrors. The Skylab PRF is actual experimental data and the two curves are shown in Figure 8. Compared to Skylab, the AXIO PRF is very sharply peaked within a few arc seconds of the central maximum. It has a HWHM of  $\sim 0.25$  arc seconds and a half power radius of  $\sim 3$  arc seconds. The latter figure is quite conservative since it can be obtained without any improvement in surface finish over that which has already been achieved with the HEAO mirrors.

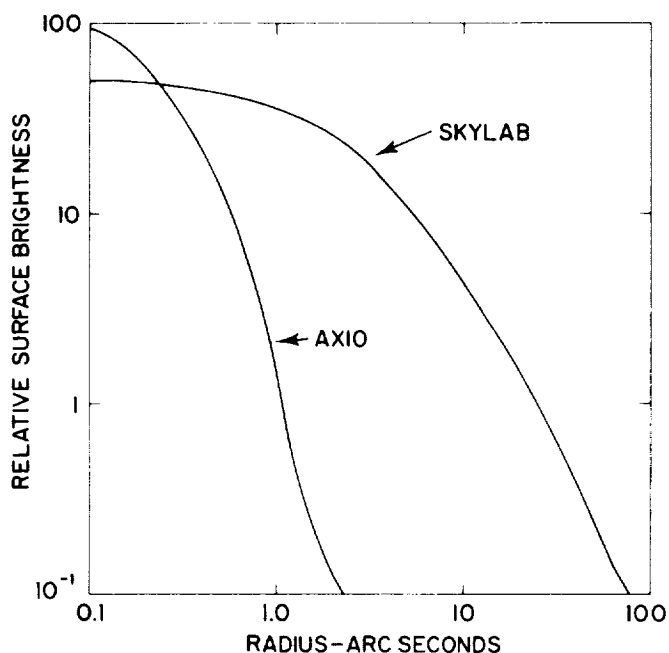


Fig. 8. A comparison of the calculated PRF for AXIO with the measured PRF of Skylab.

However, even if no further technological advances in fabrication are made and the calculated AXIO PRF is realistic, the ability to resolve the fine details of solar structure will be greatly improved compared to Skylab whose PRF within 2 - 3 arc seconds of the central maximum is nearly flat.

In order to obtain the maximum performance from AXIO the resolution of the mirrors and the detection system must be carefully matched. For the highest resolution observations, we plan to use a fine grain emulsion film as the prime detector. Unfortunately, there is a penalty for the use of these emulsions, namely their poor sensitivity. For instance we have found that it requires fifty times more deposited energy to obtain a net photographic density of 1.0 for SO-253 than for SO-212, the two emulsions compared in Figure 6. Therefore before we can calculate the ERF we have to make certain that the choice of emulsion will not limit the observations by making the exposure times too long. To check this, we have defined a criterion based on our Skylab experience. For instance we wish to record bright features, e. g., flares and active region cores, with exposure times not exceeding 4 s while we are prepared to make synoptic observations of large scale structures, coronal holes, etc., with exposures up to but not exceeding 256 s. Now the effective speed (f-number)

of an X-ray mirror can be defined as the ratio of the effective collecting area to the focal length squared and using the values in Table I, AXIO shows an improvement in speed of a factor of 2 over Skylab. This is insufficient to compensate for the difference in film speed; however, because of the increase in focal length, and hence image size, it is not necessary to use SO-253 to achieve the 0.2 arc second resolution design goal. A review of available Eastman Kodak emulsions suggests that 3414, a high definition aerial film with an intermediate grain size, is a good compromise.

Experimentally 3414 is a factor of 10 slower than SO-212 which would still leave AXIO with only 1/5 the speed of the Skylab telescope. However we have not compensated for the effect of AXIO's greatly improved PRF. The narrowing of the PRF means that more of the reflected energy will fall on the central image location, thus increasing the speed, at least for small scale features. By modelling various size features we have estimated the magnitude of this effect based on the measured results from Skylab. For cylindrical features with a source radius of 1.5 arc seconds the increase is a factor of 12, which falls to 6 for a 4 arc second radius and levels off around a factor of 3 for features larger than 10 arc seconds in radius. Taking all factors into account the speed of the AXIO mirrors together with 3414 film should be roughly equal to Skylab for large scale features and over twice as fast for the smallest features.

Having decided on the emulsion that will be used for AXIO we can now evaluate the ERFs for both AXIO and Skylab. They are calculated by integrating the PRF to form the line spread function of the mirror. This is then convolved with the line spread function of the film and the resultant is integrated to form the ERF. The results are shown in Figure 9 and the superiority of AXIO over Skylab at both high and low frequencies is obvious. To quantify the smoothing introduced by the system we find that a  $\pm 10$  percent change in the ERF at the center of the edge occurs over a spatial separation of 0.16 arc seconds for AXIO and 2.0 arc seconds for Skylab while a  $\pm 50$  percent change in the ERF reflects spatial separations of 0.82 and 14 arc seconds, respectively. Consequently, we believe that the AXIO system as presently configured will be capable of meeting the design resolution goal of 0.2 arc second.

#### The Use of Grazing Incidence Relay Optics

The previous discussion has been directed towards ultra-high spatial resolution observations using film placed at the primary focus of the grazing incidence objective mirror. However, an equally important scientific objective outlined earlier was for high time resolution observations and these almost certainly imply electronic imaging. The likely candidates for focal plane detectors, e. g., CCDs or microchannel plates, have resolution elements with center to center spacings of no less than 15 microns. Since the plate scale for AXIO is 23 microns/arc second, these devices will severely limit the spatial resolution of the observations. An

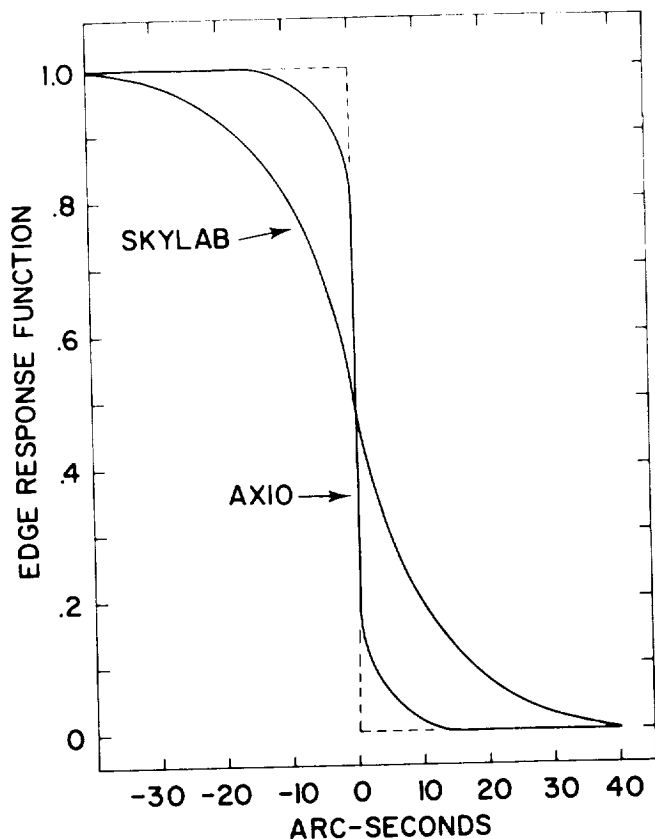


Fig. 9. A comparison of the ERFs for the Skylab and AXIO systems.

alternative to increasing the plate scale by increasing the focal length, we believe that the level of technology is sufficiently advanced to consider the development of relay optics to magnify the primary image.

In particular a grazing incidence microscope of the type described by Silk<sup>(7)</sup> could, with suitable modification, be used to image the primary focus of the AXIO mirrors to form a grazing incidence astronomical telescope, an arrangement shown in Figure 10. The secondary grazing incidence mirror has hyperboloid-ellipsoid reflecting surfaces with the forward surface designed to collect the cone of rays leaving the primary focus of the objective. Since the microscope has achieved a spatial resolution of ~ 1 micron in the object plane, it will not deteriorate the resolution of the secondary image, for the design goal of 0.2 arc seconds corresponds to 5 microns at the primary focus. The factor of 10 magnification will expand the plate scale in the secondary image to 230 microns/arc second and consequently the 15 micron center to center spacing of the CCD resolution elements would not be a limiting factor.

The price paid for the increased magnification is a restriction of the field of view. However, if the instrument is baselined with an 800 x 800 CCD, which corresponds to a (52 x 52) arc second<sup>2</sup> field of view, the transmission of this field every second would require a data rate in excess of 5 M bit s<sup>-1</sup> for 8 bits of intensity information per resolution element.

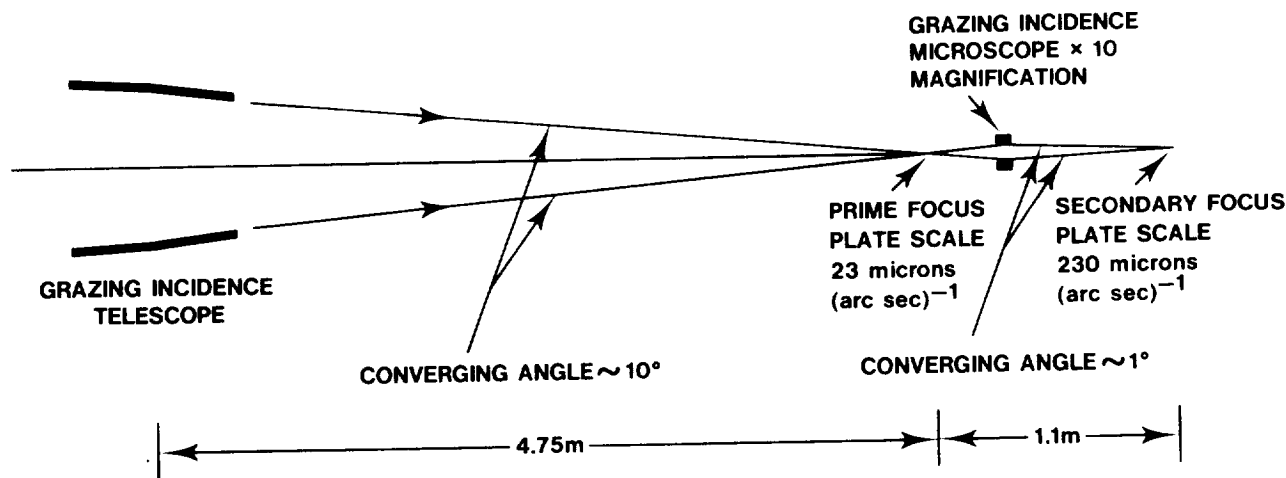


Fig. 10. A grazing incidence astronomical telescope employing two separate grazing incidence optical elements.

Therefore in the near future, the very high information content of the images is likely to restrict the area sampled to (20 x 20) arc second<sup>2</sup> which, based on our experience, is compatible with the field of view of the X-ray microscope.

Other advantages of the use of relay optics are that:

- (i) It provides the increase in magnification with only a modest increase in the total length of the instrument compared with the alternative of increasing the focal length of the objective; a difference

between 6 and 47.5 m in the example described above.

- (ii) Since the primary focus is not obstructed film cameras could be inserted there without disturbing the location of the secondary optic which is rather critical because of its small depth of focus.
- (iii) The addition of the relay optics also decreases the divergence of the X-ray beam which has a major impact when the grazing incidence mirror is used as a flux collector for a grating spectrograph. In the design shown in Figure 10 the convergence of the beam has been reduced from  $10^\circ$  after the primary to  $1^\circ$  after the secondary mirror with the result that the secondary beam is much more attractive for illuminating gratings. For now the grazing angles of the secondary beam, with respect to the grating, are below the critical angle and the reflection coefficients for the X-ray lines have reasonable values.

Although these designs are still in their infancy we believe that the progress already made indicates their feasibility and their realization will be a great assist in the quest for ultra-high resolution.

### Conclusion

In summary, the notable success of the HEAO-2/Einstein mission has demonstrated that the technology for fabricating ultra-high resolution mirrors exists. The scientific uses of such an instrument are clearly defined and extremely important to the understanding of the physics of the solar corona. When coupled with the imminent availability of the Space Shuttle Transportation System to carry large instruments into orbit, the time seems opportune for the development of a large ultra-high resolution grazing incidence mirror to serve the needs of the solar physics community.

Finally by illustrating (Figure 11) how our view of the corona has changed as the resolution of X-ray telescopes has improved, from 20-30 arc seconds in the early sixties to 2-3 arc seconds during the Skylab mission in 1973, we hope to convey the feeling of excitement that we have about this project. At the poorer resolution the areas of bright emission were isolated and found to be located above active regions. With a factor of 10 improvement in resolution, the bright emitting regions are resolved into individual loops, the basic building blocks of the corona. The improved resolution and sensitivity also reveals the presence of X-ray bright points and coronal holes. We expect that a further factor of 10 improvement will reveal the internal structure of the loops, will enable propagating wavefronts arising from energy released in localized instabilities to be tracked and perhaps allow us to observe the reconnection of magnetic field lines.

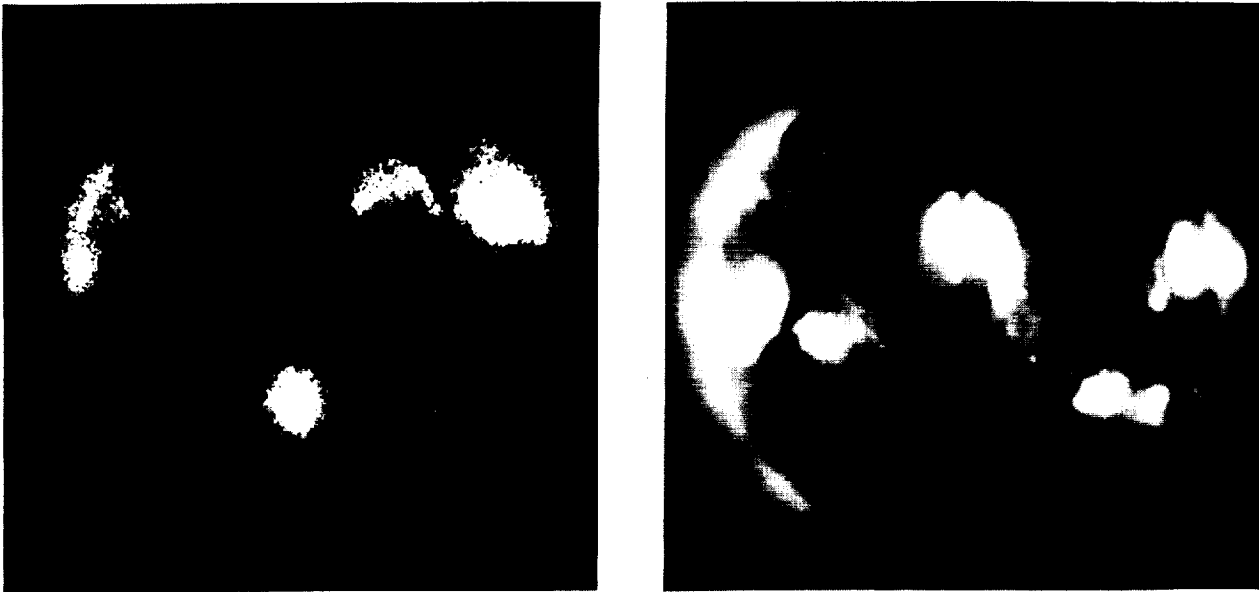


Fig. 11. Images demonstrating the effect of improving resolution on our knowledge of the structure of the corona. (a) A rocket photograph from May 1966 and (b) a Skylab image from June 1973.

Acknowledgments

It is a great pleasure to acknowledge the contributions of the many engineers and technicians at Diffraction Limited, Perkin Elmer, Applied Optics and Random Devices whose skill in fabricating grazing incidence optics has been largely responsible for our success.

The work described in this review has been supported in part by NASA under contracts NAS5-9041, NASW-2347, NAS2-7424, NAS2-8683, NAS5-25496, and NAS8-27758.

References

1. Vaiana, G.S., VanSpeybroeck, L., Zombeck, M.V., Krieger, A.S., Silk, J.K., and Timothy, A.F.: "The S-054 X-Ray Telescope Experiment on Skylab," Space Sci. Instr. 3, 19, 1977.
2. DelCarlo, C.: "Low-Scatter Metal Optics," Electro-Opt. Syst. Desgn. 3, 32, 1970.
3. Chase, R.C. and VanSpeybroeck, L.P.: "Wolter-Schwarzschild Telescopes for X-Ray Astronomy," Applied Opt. 12, 1042, 1973.
4. VanSpeybroeck, L.P.: "The Einstein Observatory Telescope - Design and Performance," Proc. SPIE 184, 1979.
5. Zombeck, M.V.: "The Advanced X-Ray Astrophysics Facility - Performance Requirements and Design Considerations," Proc. SPIE 184, 1979.
6. Wentzel, D.G.: "Heating of the Solar Corona: A New Outlook," Rev. Geophys. Space Phys. 16, 757, 1978.
7. Silk, J.K.: "Laboratory Evaluation of the High Resolution X-Ray Microscope," Proc. SPIE 184, 1979.

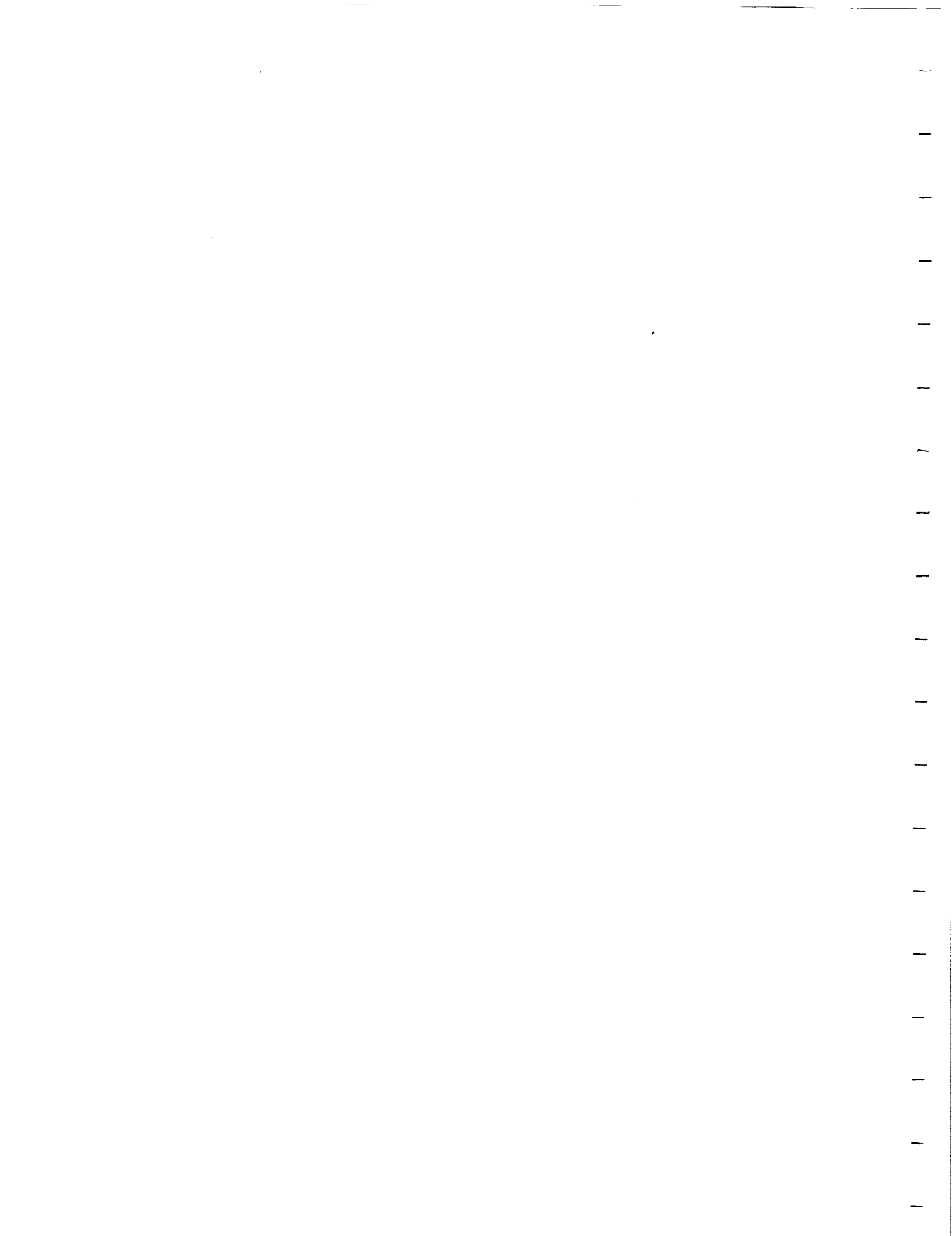
Questions from the Floor

Question 1: What is the projected curvature of field for AXIO?

Answer 1: The AXIO mirror design employs Wolter Schwarzschild surfaces and the expression for the curvature of field for such a mirror can be found in Reference 3. Substituting the parameters for AXIO, the deviation from a flat surface is 60 microns at 5 arc min and 480 microns at 15 arc min from the optical axis. If AXIO is coupled with a grazing incidence microscope to form a two element system, the curvature of field of the primary focus would not be the limiting factor. The primary focal plane would be within the depth of field of the microscope over an angle of  $\pm 2\frac{1}{2}$  arc min, which is very large compared to the useful field at the secondary focus which is of order  $\frac{1}{2}$  arc min.

Question 2: At 0.1 arc seconds, might you not require more light (x-rays) to make exposures rapidly ( $\sim 1$  sec) to prevent smearing of the image by actual motions on the Sun's surface?

Answer 2: It is quite true that there is little advantage to be gained by improving the spatial resolution for dynamic events if the temporal resolution is limited to a time which is long compared to the characteristic time, defined by the quotient of the resolution element and the velocity of the process to be observed. However, AXIO is designed to observe both static and dynamic events and the highest resolution observations will be associated with the former. The dynamic events will require electronic imaging and here the resolution will be limited to  $\sim 0.5$  arc sec, at least initially. For a sound speed of  $200 \text{ km sec}^{-1}$  the characteristic time for 0.5 arc sec resolution at the center of the solar disk is  $\sim 2$  sec, i.e., longer than the temporal resolution and therefore the image will not be smeared. As the observations are improved, we will undoubtedly run into limits imposed by the photon statistics. However, there is one saving grace, namely that at least one class of dynamic events, solar flares, have very high emissions and will allow an increase in temporal resolution of at least an order of magnitude above the one second level.



4.4 A Real-Time Electronic Imaging System for Solar X-Ray Observations from Sounding Rockets

John M. Davis, Joseph W. Ting and Michael Gerassimenko

American Science and Engineering, Inc.  
Cambridge, Massachusetts 02139

ORIGINAL PAGE IS  
OF POOR QUALITY



# A REAL-TIME ELECTRONIC IMAGING SYSTEM FOR SOLAR X-RAY OBSERVATIONS FROM SOUNDING ROCKETS

JOHN M. DAVIS, JOSEPH W. TING and MICHEL GERASSIMENKO

*American Science and Engineering, Inc., 955 Massachusetts Avenue, Cambridge,  
Massachusetts 02139, U.S.A.*

(Received 2 February, 1979)

**Abstract.** A real-time imaging system for displaying the solar coronal soft X-ray emission, focussed by a grazing incidence telescope, is described. The design parameters of the system, which is to be used primarily as part of a real-time control system for a sounding rocket experiment, are identified. Their achievement with a system consisting of a microchannel plate, for the conversion of X-rays into visible light, and a slow-scan vidicon, for recording and transmission of the integrated images, is described in detail. The system has a quantum efficiency better than 8% above 8 Å, a dynamic range of 1000 coupled with a sensitivity to single photoelectrons, and provides a spatial resolution of 15 arc seconds over a field of view of 40 × 40 square arc minutes. The incident radiation is filtered to eliminate wavelengths longer than 100 Å. Each image contains  $3.93 \times 10^5$  bits of information and is transmitted to the ground where it is processed by a mini-computer and displayed in real time on a standard TV monitor.

## 1. Introduction

During the past decade high spatial resolution X-ray images of the Sun's corona have been obtained using grazing incidence optics and photographic film [1-4]. Although there have been major advances in the recording techniques and in the analysis of the images [5], the use of film as the detector has so far limited their application to sounding rockets and manned spacecraft, where recovery of the film is possible. However, photoelectric detection of the X-rays and subsequent electronic imaging would allow the techniques to be extended to non-manned satellites and would in addition permit real-time control of the experiment either from the ground or in the case of the Space Shuttle from the Payload Specialist Station. The imaging capability would also enable non-imaging X-ray diagnostic instrumentation with narrow fields of view to be directed at targets on the solar disk selected on the basis of their X-ray rather than their visible light (e.g., H $\alpha$ ) signature. In this way several classes of coronal phenomena, for example X-ray bright points, coronal arches or coronal hole boundaries, which in general cannot be observed at longer wavelengths, can be studied directly. Primarily to meet this objective but also to provide experience for eventually replacing film entirely, an electronic X-ray imaging system has been developed for flight on a sounding rocket as part of a target acquisition system for a narrow field, plane crystal, X-ray spectrometer. Since electronic cameras cannot yet provide the same spatial resolution as film, the rocket instrument also included a photographic camera to record data for post flight analysis. Since there is only a single X-ray mirror, the experiment

was designed so that the two cameras could be interchanged in the focal plane either automatically or as a result of a ground command.

The scientific objectives of the experiment and the characteristics of the X-ray emission from the Sun establish the specifications of the electronic imaging system. They are:

- (1) A spatial resolution of better than 15 arc sec which corresponds to 9 line pairs per millimeter at the focal plane detector.
- (2) A dynamic range in excess of 100 coupled with the capability of detecting single photons and of withstanding 5 orders of magnitude above this minimum level without permanent damage.
- (3) A capacity to integrate signals for periods up to tens of seconds.
- (4) Stable photometric accuracy under varying environmental exposure conditions and freedom from geometrical distortions.

To meet these requirements we have developed a system which uses a micro-channel plate (MCP) to convert the X-rays into visible light and a slow scan vidicon for signal recording and readout. The two units are coupled together using coherent fiber optics. This solution was chosen over relay optics to simplify the design of the interchangeable focal plane assembly.

To match the image size formed on the front plate of the MCP to the scanned area on the vidicon faceplate, the MCP phosphor is deposited directly onto the surface of a reducing fiber optic which reduces the image size by a factor of 1.5 (linear dimension). The demagnified image is transmitted to the fiber optic faceplate of the vidicon through a flexible coherent fiber bundle, or imagescope. The fibers in the optic and the vidicon are grouped in hexagonal arrays, whereas those in the imagescope form square arrays to minimize the Moiré patterns arising at the interfaces. For the same reason the individual fiber diameters change from 6 microns in the optic to 10 microns in the imagescope and back to 6 microns in the vidicon faceplate.

The detailed instrument description which follows is divided into sections devoted to the X-ray detector, the video camera, various circuit details and system performance.

## 2. The X-ray Detector

The solar X-ray corona viewed from the Earth subtends an angle of approximately 40 arc min. The image of this field produced by the rocket grazing incidence telescope has a diameter of 17 mm. Of the photoelectric detectors currently available, only the microchannel plate (MCP) combines high spatial resolution with a sufficiently large sensitive area to detect this image.

MCPs consist of close-packed arrays of geometrically uniform, semiconducting glass channels. The channel diameters may be chosen from within the range 8–50 microns, depending upon the application, and typically the channel diameter is 80% of the center-to-center spacing. When X-rays strike the inner surface of one

of the channels they are either reflected or absorbed. Since the work function of the glass is a few electron volts, the absorbed X-rays release one or more electrons. The application of an electric field between the ends of the plate accelerates the electrons and an electron avalanche forms as a result of further collisions with the channel walls. Upon exiting from the channels the electrons are proximity-focussed onto a phosphor screen. The overall gain of the system is limited to  $10^4$  by a process called ion feedback which arises because of the linear geometry of the channels. The effective gain can be increased by mounting plates in tandem in such a way that the channels of one plate are set at a small angle, or geometrical bias, to the plane of the MCP. This eliminates the straight path through the combined plate and the ions, because of their mass, are trapped at the junction of the plates [6]. This configuration which is called a chevron plate allows gains in excess of  $10^7$  to be obtained and chevron plates, manufactured by Galileo Electro-Optics [7], were used in the present instrument. For the flight unit we chose a chevron plate with a circular sensitive area of 25-mm diameter with 25-micron-diameter channels arrayed on 31-micron centers. This geometry provided a suitable match to the image size and resolution requirements; however, the more advanced projects that we have planned will need both smaller channels and larger sensitive areas.

The quantum efficiency of the MCP is a function of the angle at which the incident X-rays strike the channels [8], which in turn is set by the  $f$ -number of the imaging system. Because of the finite size of the solar image and the fact that grazing incidence optics produce an annular bundle of rays, the striking angle varies between

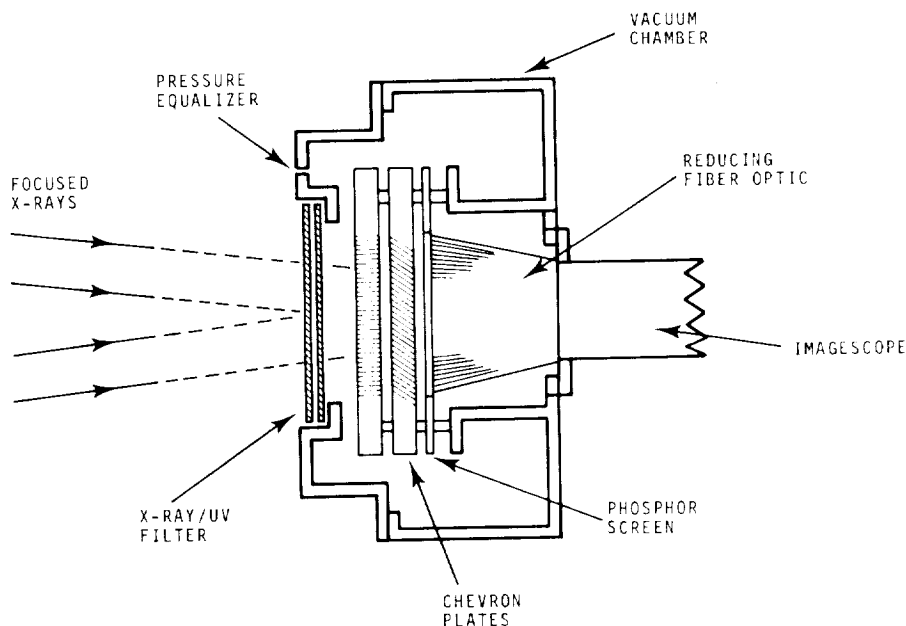


Fig. 1. Schematic diagram of the MCP focal plane assembly.

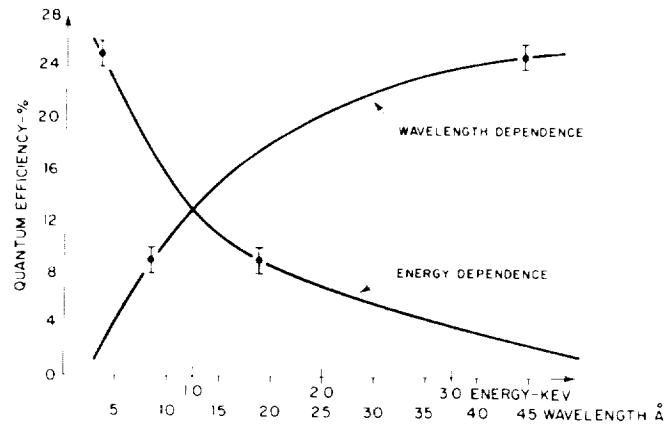


Fig. 2. The variation of the quantum efficiency of the MCP with wavelength (energy) for a fixed glancing angle.

5.5 and 6 degrees in the present instrument. As the quantum efficiency peaks close to this angle the channels of the first plate are aligned parallel to the optical axis of the imaging system and the second plate set at a bias of 15 (Figure 1), i.e. the reverse of the normal arrangement. This geometry provides approximately uniform quantum efficiency across the image. Actual measurements were performed at 8.3 and 43.4 Å and are shown in Figure 2 where the solid line represents the theoretical efficiency calculated using the model of Bjorkholm *et al.* [8] and normalized to the experimental data at 8.3 Å. The required passband of the detector is from 7 to 60 Å and the data show that the quantum efficiency increases monotonically from 7% to 25% across this range.

### 2.1. MOUNTING ASSEMBLY

Since the MCP can only be operated below  $2 \times 10^{-6}$  torr and must be conditioned for several hours at or below this pressure before the voltage is applied, it was enclosed in a stainless steel vacuum chamber (Figure 3). Copper gaskets were used throughout and the chamber was continuously pumped using a  $2 \text{ l s}^{-1}$  titanium cathode ion-pump [9]. To save weight the standard iron magnet was replaced by a magnet made from cerium cobalt [10] which has provided excellent performance at less than one fifth of the total weight. Typical operating pressures of  $5 \times 10^{-7}$  torr have been obtained.

The front port of the vacuum chamber contains a quartz window which allows the MCP to be operated in the payload during ground testing. The front port releases and swings forward when the MCP is driven into the focal plane. This action exposes a thin aluminized organic X-ray filter which now forms the forward vacuum seal. To minimize the pressure differential across the filter this event is timed to occur above an altitude of 120 km.

We have chosen not to operate the pump during flight to avoid the possibility

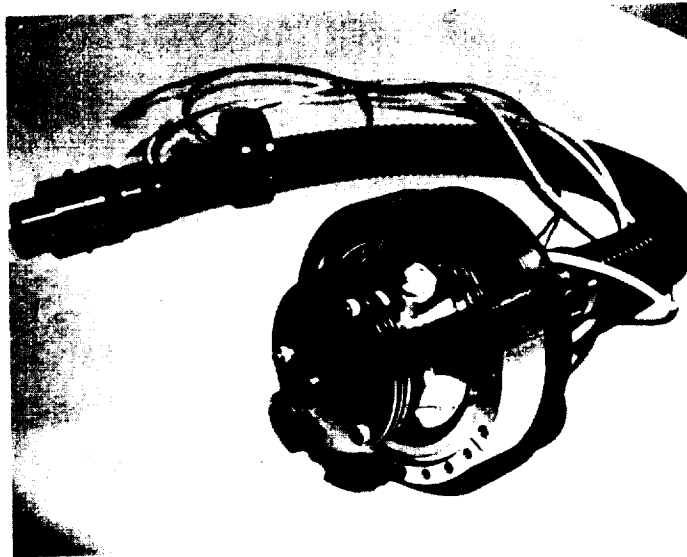


Fig. 3. A photograph of the MCP mounted in its stainless steel vacuum chamber with the front cover removed. The imageoscope is also shown.

of ion contamination of the MCP; this was never a major problem on the ground although its operation could be detected at the highest gain settings as a slight increase in the noise. However, the ion-pump is also used as a diagnostic aid to measure the chamber pressure and for this function its in-flight operation can be controlled from the ground.

## 2.2. X-RAY AND EUV FILTERING

The solar EUV and UV radiations, to which the plate is sensitive, are prevented from reaching it by a composite filter of 3000 Å of aluminum and 5 microns of polypropylene ( $C_3H_6$ ). The most critical wavelength region for the filter lies just beyond the aluminum L-edge between 170 and 250 Å. The transmission of the filter can be calculated using the mass absorption coefficients of Caruso [11] and Henke and Elgin [12]. It was found that increasing the thickness of polypropylene will reduce the transmission in the 170–250 Å waveband faster than the transmission at the shorter X-ray wavelengths. The actual thickness of the filter was chosen so that it would reduce the number of photons in the incident spectrum in the longer waveband to less than 5% of the number between 7–60 Å.

The filter is made in a sandwich; the first layer consists of 2.5 microns of polypropylene with 1500 Å of aluminum on either side and is followed by a separate film containing the balance of the polypropylene. The use of two layers of aluminum has been found to produce a much higher yield of pinhole-free filters and the sandwich construction isolates the second aluminum layer from the MCP and prevents UV-produced photoelectrons from producing noise counts.

### 2.3. THE MCP GAIN

Although the MCP can be operated at gains up to  $10^7$  there is a distinct advantage to operating at lower gains as this will reduce the noise contribution from spurious events. The required gain can be estimated from a knowledge of the sensitivity of the vidicon and the requirement that the system be able to detect single photoelectrons.

Typical slow scan vidicons are sensitive to a faceplate illumination of 0.01 foot-candles per second which corresponds to approximately  $0.17 \text{ erg s}^{-1} \text{ cm}^{-2}$ . If the sensitive area ( $\sim 1 \text{ cm}^2$ ) is divided into a  $256 \times 256$  pixel matrix (see Section 3.1), the energy required per pixel is on the order of  $3 \times 10^{-6} \text{ erg s}^{-1}$ . The maximum spectral response of the vidicon and the peak output of the MCP phosphor were matched at  $4200 \text{ \AA}$ . Using this wavelength the number of photons required to produce a useable signal is  $6.3 \times 10^5$ . Under normal operation the phosphor provides a gain of 100; consequently to detect single X-ray photons the MCP need only provide a gain of  $10^4$ . On the basis of the manufacturer's gain characteristics this requires operating the plate under a potential difference of 1350 volts. This is well below the maximum recommended operating voltage (2200 V) and ensures that the operation of the plate is essentially noise free.

Because of the wide range in intrinsic brightness of the X-ray corona ( $10^3$ – $10^4$ ), the imaging system was provided with three time exposures by electronically shuttering the MCP. The three exposures were nominally 1/4, 1 and 4 s and were obtained by gating the plate voltage. Thus each exposure duration is defined by the time the high voltage is maintained across the plate allowing electron multiplication to take place. When the exposure is over, the gating pulse is turned off and the plate is returned to a lower voltage where multiplication does not occur. The rise and fall time of the power supply was approximately 20 ms which is adequate for defining even the shortest exposure.

The three time exposures coupled with the intrinsic dynamic range of the vidicon ( $\sim 100$ ) provide a total dynamic range of  $1.6 \times 10^3$ . This value is marginal for detecting the range of phenomena on the sun and leaves little room for error in selecting the flight settings. The first alternative of adding further exposures, e.g. 16, 64 s, etc., was rejected as their addition to the sequence would take up too great a fraction of the observing time (approximately 100 s of the flight was all that could be allotted to the operation of the X-ray video system). An alternative approach is to vary the gain of the MCP by controlling the voltage applied across it. For instance if the gain is increased by a factor of 64 then the signal recorded by the vidicon during the shortest exposure will now be equivalent to four times the signal recorded during the longest exposure at the low gain setting, for a source of constant illumination. Thus the combination of the three exposure sequences and the two gains will provide a total system dynamic range in excess of  $10^5$ . This increase in gain can be achieved with a potential difference across the plates of 2000 V, which is still well below the maximum operating voltage. The instrument is launched in the low gain config-

uration and if the picture displayed on the ground monitor is too faint, the gain of the MCP can be increased by activating a relay closure, by way of a radio link, to select a second biasing resistance on the low voltage side of the MCP high voltage power supply.

### 3. The Video Camera

#### 3.1. DESIGN CONSIDERATIONS

The video camera is designed to meet the scientific requirements of the experiment within the constraints set by the capabilities of the telemetry and ground data handling and display systems. To recapitulate, it must possess a dynamic range of at least 100, a spatial resolution corresponding to 15 arc seconds and a capacity to integrate signals for a few tens of seconds. To interpret the spatial resolution requirement consider a square field of view of  $40 \times 40$  square arc minutes which satisfactorily contains the solar image. For such a field a picture format of  $256 \times 256$  pixels provides 10 arc second resolution elements. The incident flux within each pixel is represented by one of 64 intensity levels (6 bits) which our experience, gained with the computer display of digitized photographic images, has shown to provide an adequate visual representation of the corona and also suitably matches the dynamic range of the imaging system.

As it is necessary to integrate the X-ray signal for several seconds to obtain sufficient intensity the vidicon tube must combine image storage and high resolution during operation at room temperature. Although secondary electron conduction (SEC) vidicons have excellent storage capabilities, their spatial resolution and dynamic range are severely limited. The best available tubes at the time (1975) had a resolution, at the center of the frame, of only 250 TV lines with a 50% modulation transfer function (MTF). Comparable figures for slow scan vidicons are in excess of 800 TV lines and under slow scan operation, vidicons have been developed which retain over 90% of their signal for periods in excess of 20 s. They operate at room temperature, have dynamic ranges over twice as wide as SEC vidicons and are much less susceptible to burn out, being able to withstand signals in excess of  $10^5$  times the minimum without suffering damage. Both types of tube have similar photometric accuracy and are capable of providing an absolute accuracy of approximately 10% which is adequate for the present application. Therefore, because resolution and dynamic range were of primary importance, a slow scan vidicon was selected as the basis of the camera design.

A pulse coded modulation (PCM) transmitter is used to relay the video pictures and additional scientific data to the ground. Each telemetry data frame is divided into 32 twelve-bit words and the repetition frequency is  $1024 \text{ frames s}^{-1}$ . Ten words of the 32-word frame are used to transmit the video data. Of these ten, 8 contain pixel intensity coded into 6 bits, or 64 grey levels; the remaining two bits of each intensity word are used for housekeeping or other low bit rate data. The sixth word identifies the vertical and horizontal locations, within the image array, of the first intensity

word of the group of 8 and the tenth word indicates the presence of TV data. This last word is used to alert the computer, which displays the data, that a time exposure has been completed and that a readout cycle is underway. Each picture is composed of  $2^{16}$  pixels and takes 8 s to be transmitted; therefore, the greatest storage time for an image will be 12 s, i.e., the sum of the longest exposure plus the transmission time, and signal losses from the vidicon target will be minimal. The TV information is presented to the transmitter in parallel form through a cable of 8 wires, one for each bit of the data word. All the bits are clocked together and synchronized with the telemetry system so that after each word is sampled a new complete word is shifted into the transmitter buffer.

We have used a camera readout technique which we call 'dot scanning.' In contrast to the continuous sweeps used in standard cameras, each pixel in the  $256 \times 256$  square format is read by turning the electron beam on and off at each location. While the beam is off, the magnetic deflection fields are changed to select the next pixel location (see Figure 4 for a timing diagram of the read cycle). After a picture is read out, the charge pattern left on the target is the whole picture less the partially filled 'dotted holes.' The erasure scan that follows must charge the target uniformly, thereby reconditioning it for the next exposure. In order to assure complete erasure, the electron beam makes continuous sweeps during the erase cycle. To minimize the time between exposures, erasure is limited to a single scan and consequently a

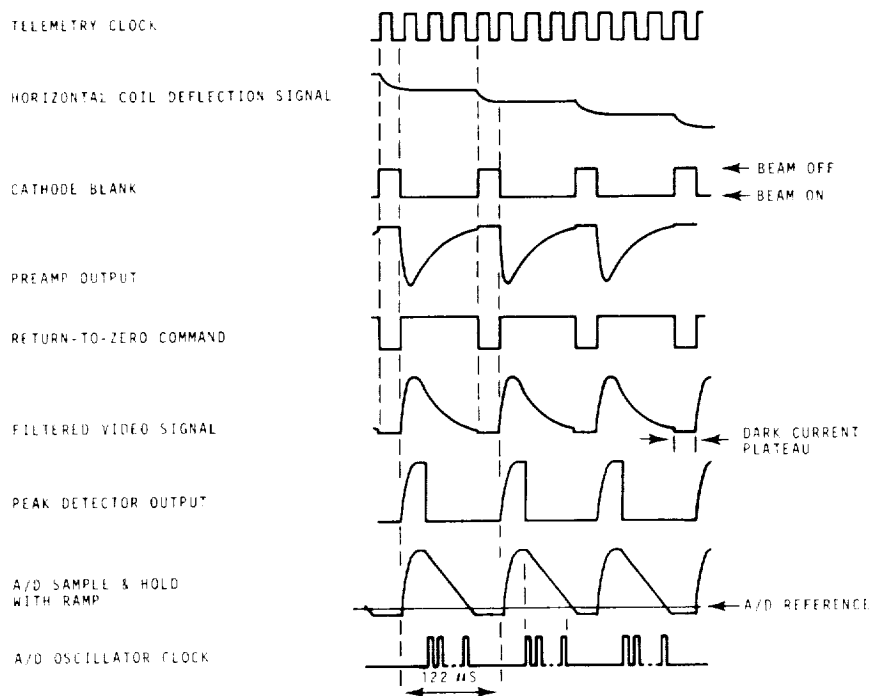


Fig. 4. The read cycle timing diagram.

small residual image may remain after the completion of the read-erase cycle. The residual image is a result of a combination of effects arising from the surface impedance of the photoconductor, the impedance of the scanning beam and the capacitance of the target. Several methods of improving the efficiency of the erase scan were investigated. They included increasing the beam current by increasing the target potential during the erase cycle and the superposition of a vertical 'dither' to the horizontal scan with an amplitude equal to the separation of the scan lines. Although the first method removed the residual traces of the highlights from the previous exposure, it substantially decreased the dynamic range by cutting off the low level signals. The dither system made only marginal improvements to the picture; therefore, in the interest of simplicity and reliability the changes in the erase scan were limited to the adoption of a continuous sweep cycle.

Although power consumption is not usually a severe problem on short duration rocket flights, low power circuits were used whenever possible and CMOS was chosen for the logic family. The total power required by the camera is 12 W which is supplied by 3 packs of high rate silver zinc batteries. The packs are mounted within pressurized battery boxes and are assembled to provide +28 V and  $\pm 18$  V. The +28 V supply is used for the vidicon heaters and for the focussing coil, in each case being independently current regulated. The  $\pm 18$  V packs are voltage regulated to +15 V and  $\pm 12$  V and are used for the biasing of the vidicon and the control of the logic circuits.

Finally, past experience has shown that electronic memory devices, such as flip flops, often reset, without any apparent reason, during typical rocket flights. We believe the cause to be momentary power interruptions, perhaps resulting from relay contact bounce, and to prevent this possibility affecting the camera operation, a diode capacitor network, capable of holding enough charge to maintain the circuit for a few milliseconds, has been built into the system wherever necessary.

### 3.2. THE VIDICON

To implement the design, several slow scan vidicons manufactured by General Electrodynamics [13] were tested. The tubes are part of a series of space qualified designs which have been used successfully on several Mariner missions. The preliminary tests resulted in the selection of a model 7290 vidicon. It has a custom-fitted fiber optic faceplate and combines magnetic focussing and deflection. The material of the target is amorphous red selenium. It has a dark resistivity of  $10^{13} \Omega \text{ cm}^{-1}$  which permits slow scan operation at room temperature. This particular model is not ruggedized, but since it was planned to launch the experiment with power off, it was considered to be mechanically adequate and this decision has been justified by flight experience.

The slow scan vidicon can be visualized as a special tetrode tube. Its essential elements are an electron gun, an electric field free region and a target (Figure 5). The electrons are generated in the gun by thermionic emission from the indirectly heated cathode. The number of free electrons, or beam current, is regulated by the

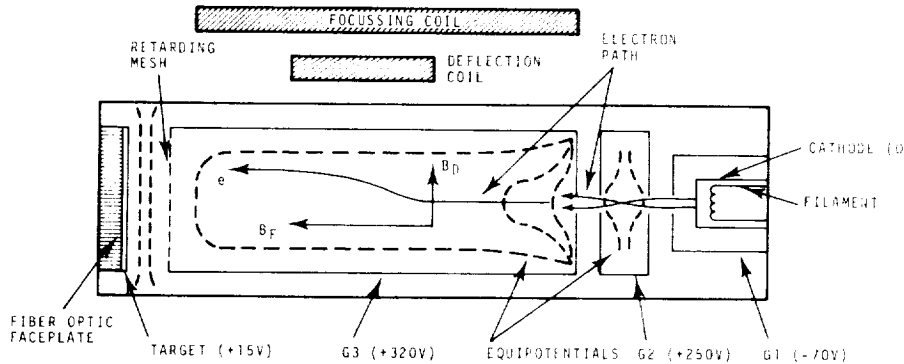


Fig. 5. Schematic diagram of the vidicon tube.

G1 electrode which plays the same role as the control grid in a triode. Leaving G1, the energy of the electrons is increased to +250 V by the accelerating grid G2. At this energy the electrons can be deflected without substantial dispersion arising from their Coulomb repulsion. This grid also acts as an electrostatic lens and focusses the beam into its first crossover point which occurs within the lens. The slightly divergent beam exiting from G2 is refocussed by the action of G3 which is set at +320 V. This grid provides a region free of electric fields where the beam can be magnetically deflected using coils aligned such that their field is normal to the electron beam. At the far end of G3 is a fine wire mesh placed directly in front of the target and held at the same potential as G3. The uniform electric field between the mesh and the target decelerates the electrons so that they strike the target at near-zero velocity. This 'soft landing' prevents the generation of secondary electrons which are a source of 'blooming'. Beam focussing, as in most high-resolution tubes, is achieved by using a separate coil to produce a uniform magnetic field aligned parallel to the electron beam. The field causes the electrons to spiral around their direction of motion and by adjusting its strength a node can be located at the target where the displacement due to the random perpendicular component of the velocity of the electrons is zero. Thus the field has the effect of focussing the first beam crossover point onto the target.

The control grid voltages are supplied from two separate d.c. to d.c. converters that operate on +28 V d.c. power. A custom made MIL power supply [14] provides the -70 V for G1 and the +250 V for G2. A separate Velonex [15] supply provides the +320 V for G3. The high audio chopping frequency of the converters was a significant source of noise and it would have been preferable if they had been synchronized to the basic camera clock frequency of 9.192 kHz or its first harmonic.

#### 4. Circuit Details

A functional block diagram of the camera electronics is shown in Figure 6. It consists of three major elements:



TABLE I  
Logic functions for the video camera

Mnemonic	Function
ZRZ	Video d.c. restoration command.
PDR	Peak Detector Reset; discharges the peak holding capacitor.
PIB	Peak Detector Inhibit; disables the input to the peak detector at the same time PDR is exercised.
ZSH	ADC sample and hold command.
HSH	Sampling command for the horizontal sweep sample and hold converts the linear ramp into a staircase.
CBK	Blanking signal for the tube cathode. It holds the beam off during the time when the beam is being switched from one pixel to the next and during exposure and beam retrace times.
HOR	Horizontal sweep integrator reset.
VER	Vertical sweep integrator reset.
IIG	Image intensifier gating; this is the electronic shutter command.
HAD & VAD	8-bit counters that are synchronized with the horizontal and vertical sweeps. They indicate the X and Y addresses of the pixel being read out.
EXS	Exposure sequence indicator; shows which one of the three exposures is being read out.
CIN	Input clock derived from the PCM transmitter.
FIN	Synchronizes the start of every read cycle with the PCM frame encoding. Its presence simplifies the frame decoding by the ground computer.

pixel, is due to the induced charge flow from that pixel through the target bias and preamplifier circuitry. To detect this charge flow a current-to-voltage preamplifier (Figure 7) was chosen because it reproduces the physical target discharge more directly and has high speed because of its relative independence of source and stray capacitances. Because the input is a virtual a.c. ground, almost all of the signal current goes to develop the output voltage. If a true current-to-voltage conversion is to be made, the input bias current to the preamplifier must be much less than the minimum signal current that is to be measured. The detectable signal above the dark noise, during a typical beam gating read cycle, is on the order of a few nano-amperes and therefore the bias current of the preamplifier input has to be lower than this value, which calls for an FET input stage.

The minimum dynamic range of the tube is specified by the manufacturer as 200 and therefore the preamplifier should not significantly degrade this value. The best compromise in terms of dynamic range and low bias is a pair of discrete low

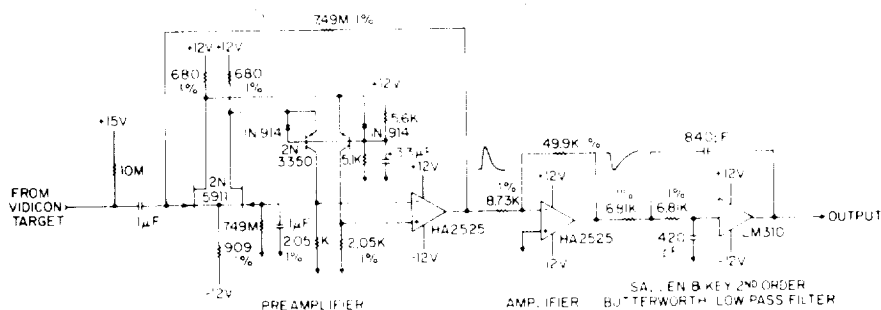


Fig. 7. The front end of the video chain showing the details of the preamplifier and the low pass filter.

noise FETs at the input of a fast, good quality, operational amplifier. This arrangement was preferred over an FET operational amplifier because discrete FETs offer much better noise characteristics. Secondly, a balanced differential configuration is preferred over a single FET input circuit because such an arrangement rejects common mode noise. However, the high frequency response is degraded because of the Miller effect which reflects the gate to drain capacitance back to the input, multiplied by the gain of the FET.

The addition of a pair of bipolar transistors connected in cascode with the FETs improves the high frequency response; however, in the present design a 'folded cascode' differential pair is used. The advantages it presents over the simple cascode are several: (a) it allows a larger input voltage swing; (b) the quiescent current of the FET and bipolar transistor can be biased separately; and (c) the output voltage of the stage swings closer to halfway between the supply voltages. Its gain expression is identical to a simple cascode, provided  $R_d > Z_e$  where  $Z_e$  is the input impedance of the common-base bipolar transistor and  $R_d$  is the drain resistor. This condition is easily met, because  $Z_e \approx 50 \Omega$ . The input differential FET pair used is a 2N5911 and the bipolars are implemented by a 2N3350, a dual PNP in a single can. The operational amplifier is the high slew-rate, dielectrically isolated Harris HA-2525. The closed-loop Bode plot of the preamplifier response is shown in Figure 8. The measured noise was  $120 \mu V_{\text{rms}}$ .

The second stage in the chain is the two-pole low-pass filter which is added to remove all high frequency noise from the video signal, especially that arising in the vidicon bias power supplies. It consists of a two-pole Butterworth-type active filter [16], built around a high-input impedance unity-gain buffer (Figure 7). Since all the time constants of the vidicon tube are invariant with the signal strength, some of the higher-frequency components can be attenuated without impairing the linearity of the amplitude response. It is important that the filter does not alter the dark current plateau (see Figure 4) from which the d.c. restoration is made. The minimum breakpoint frequency to meet this requirement was found experimentally to be 40 kHz.

As the target is a.c. coupled to the preamplifier it produces a signal with average

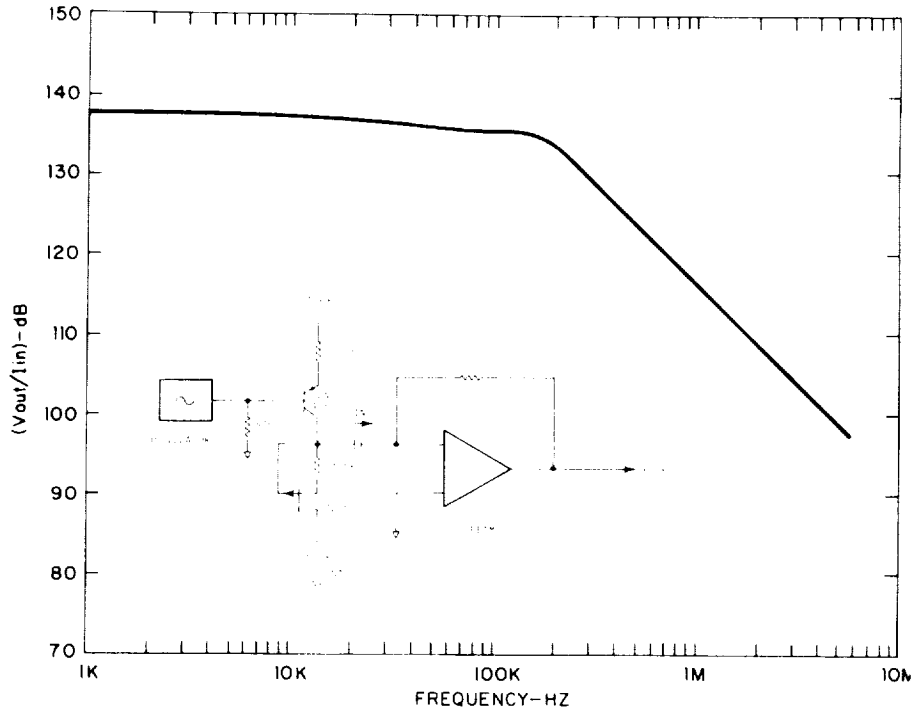


Fig. 8. The experimentally measured Bode plot of the video preamplifier. The insert shows the circuit used to obtain the result.

charge balanced around zero volts. Consequently d.c. restoration is required to bring the dark current plateau of the signal back to zero volts and is accomplished by subtracting the preamplifier signal from the continuous dark current level of the tube with the help of a sample and hold circuit.

Following d.c. restoration the peak amplitude voltage of the signal, within a specified time interval, is detected and held. Conceptually, a capacitor and a perfect diode are sufficient to perform this function; however, it is obvious that a real diode cannot provide good peak transfer linearity because diodes exhibit voltage drops in the forward biased condition. If instead, the diode capacitor combination is placed inside a negative feedback loop of an operational-amplifier, the offset is divided by the open loop gain of the operational-amplifier, thereby reducing it to a negligible error. A circuit based on this concept was built with the peak holding capacitor connected as the load of an emitter follower. The base to emitter junction of this transistor, besides replacing the diode, also supplied extra current gain in the forward direction. A discrete operational-amplifier is used, because integrated types are too slow. When the circuit was initially tested for fast rise input signals, the output carried a large overshoot. As this deviation disappeared when the input was slowed down, high frequency peaking, with a low damping ratio, was suspected

and a suitable two-pole, one-zero shunt filter designed for the appropriate frequencies cured the peaking problem without sacrificing the speed.

After each pulse detection, the holding capacitor is reset by a shorting switch. This switch is placed inside the feedback loop of an operational-amplifier so that the reset voltage remains constant. An input clamping switch protects the output stage of the circuit from being shorted to ground.

Finally the analog signal voltage is measured and converted, using a single-slope open loop circuit, into a digital output signal. This design was chosen because of its simplicity and because it provides sufficient accuracy for 6-bit resolution. It is accomplished by connecting the output of the peak detector to a constant discharge sample and hold. As long as the switch of this sample and hold is closed, the peak level of the signal is reproduced. But as soon as the switch opens the signal starts to decay at a constant rate. The decay time to a reference level is measured against a digital clock.

#### 4.2. THE DEFLECTION CIRCUITRY

This circuitry drives the horizontal and vertical deflection coils which produce the magnetic fields and which in turn control the sweep of the electron beam across the target. Two integrators generate the horizontal and vertical sweeps under logic control. The linear vertical sweep is applied directly to the vertical coil driver while the horizontal linear sweep is first transformed into a voltage staircase through the action of a sample and hold. Each step, when converted into coil current, deflects the beam into a particular horizontal pixel location. The block diagram of the deflection circuitry is shown in Figure 9.

During the reset, the capacitors of the integrators are discharged by JFET analog switches. Care was taken to assure stable operation. All critical resistors are precision types and the integrating capacitors are made of low leakage polycarbonate material.

Originally, instead of analog integrators, a natural binary counter followed by a CMOS digital to analog converter (DAC) generated the horizontal staircase signal. Unfortunately the DAC exhibited excessive differential non-linearities, which meant the distances between pixels were not always constant. As an example, in the camera, there are 8 pixel bits in each direction. If a 5% maximum differential linearity is allowed, then the DAC must have at least 13 bits. Such a DAC was not available in a low power version at the time the camera's design was completed.

Before the deflection coil drivers, the horizontal and vertical reference signals go through adjustable amplifiers in which both gains and offsets can be varied. The coil drivers are essentially closed loop voltage to current converters. The peak deflection currents for the horizontal coil driver are  $\pm 90$  mA. An integrated power operational-amplifier, the Fairchild  $\mu A$  791, was used for this purpose. The peak vertical deflection coil currents are only  $\pm 10$  mA, and here a monolithic LM301A operational-amplifier was employed.

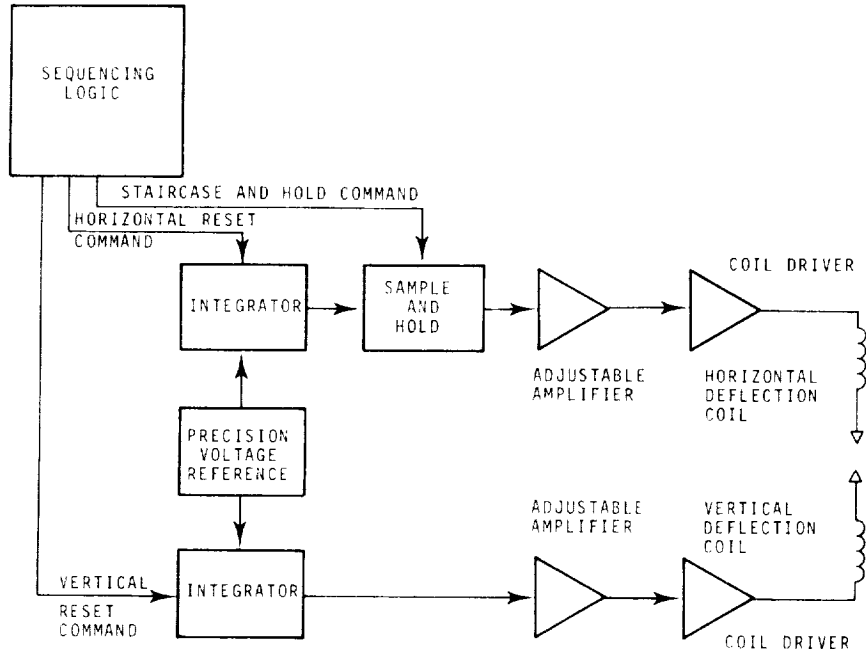


Fig. 9. Functional block diagram of the deflection circuits.

## 5. Performance

In the current application the parameters of major interest are the sensitivity, dynamic range and spatial resolution of the system and their evaluation was carried out in two stages. In the first stage the performance of the vidicon camera and electronics was optimized using visible light illumination of the camera. Once this was accomplished the performance of the whole system was studied using either X-ray or UV illumination.

### 5.1. DYNAMIC RANGE MEASUREMENTS

Since the solar X-ray corona has an intrinsic brightness variation in excess of 4 orders of magnitude it is most important that the dynamic range of the system be as large as possible in order to minimize the range of exposure times required to display the different phenomena. Consequently particular attention was paid, during the design of the video chain, to maintaining the inherent dynamic range of the vidicon. Once the camera was assembled the dynamic range was measured and the measurements repeated as the various parameters and circuits were adjusted and modified. The procedure followed consisted of illuminating the vidicon with a diffuse halogen light source operated at constant voltage. While the incident light intensity was held constant, the length of the exposure was varied using a com-

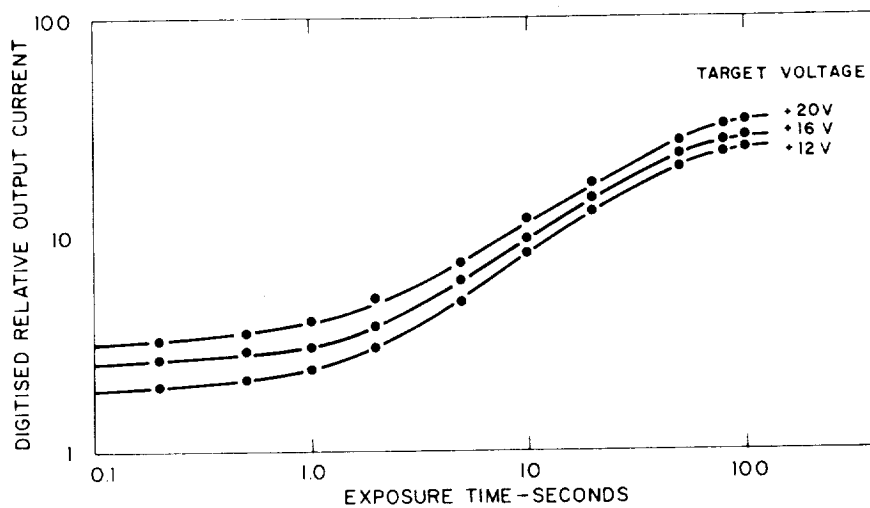


Fig. 10. The dependence of the dynamic range on the target bias voltage.

puter controlled shutter. The computer recorded the data and the integrated light output was formed from an average of the central  $50 \times 50$  point pixel array.

Typical response curves, for several values of the target bias voltage, are shown in Figure 10. Contrary to expectation the dynamic range is insensitive to this voltage, which controls the gain of the vidicon, and in all cases the dynamic range, defined as the ratio of the incident light required to saturate the tube to the noise signal, is in excess of 1000. A target bias of 15 V was ultimately chosen for the vidicon as this provides an optimum system gain. Too high a gain results in the formation of 'bright spots' caused by electrical breakdown in target surface non-uniformities.

These curves are only valid for exposure times which are sufficiently short for the integrated dark current to be negligible. Experimental data showed that, at room temperature (21 C), the dark current increased monotonically with time. However, for exposures of less than 15 s the noise contribution was at or below the level of detectability and therefore, since the longest exposure planned for the flight sequence was 4 s, the dark current does not limit the dynamic range of the system.

The total system response was measured in an analogous fashion except that 8.3 Å X-rays were used instead of visible light. The MCP was operated in vacuum at a pressure below  $1 \times 10^{-6}$  torr and was illuminated by a uniform monochromatic source of X-rays obtained by filtering a beam generated by electron bombardment of an aluminum anode. The instantaneous flux incident on the MCP was measured with a calibrated proportional counter. The measurements were performed using the flight program which generated exposures of 1/4, 1 and 4 s by using the MCP as a shutter and the average integrated intensity over the central  $50 \times 50$  pixel array was calculated by the computer as before. The response curves were generated by varying the incident X-ray flux and typical values are shown in Figure 11. It

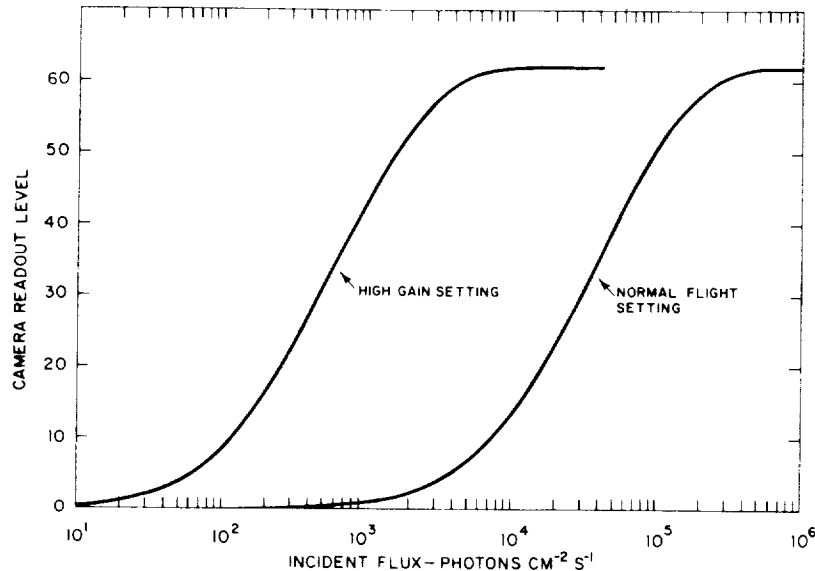


Fig. 11. The dynamic range of the electronic imaging system irradiated with 8.3 Å X-rays at the two flight MCP gain settings.

can be seen that the dynamic range of the system is approximately 1000. Note that even at the highest gains, where single photons are being detected, the noise contribution from the MCP itself is small. The curves for the two flight settings of the MCP gain are shown and inspection shows that a total range in incident energy of 5 orders of magnitude can be observed.

## 5.2. SPATIAL RESOLUTION

The spatial resolution of the total system is a result of folding together the modulation transfer functions (MTF) of the individual elements of the imaging system. These are the X-ray mirror, the MCP, the fiber optic and imagescope and the TV camera. Of these components only the camera is capable of adjustment and consequently its evaluation was performed first using visible light illumination.

Slow scan vidicons are inherently capable of much higher resolution than standard TV rate vidicons and for the tube chosen modulations of 50% at 800 TV lines are typical. However, because of telemetry limitations, the video picture was limited during flight to 256 lines per frame and this format was used throughout the test program. The MTF was evaluated using a Limansky mask [17, 18] and the computed maximum and minimum sine wave responses, which depend on the relative positions of the sampling elements and the lines in the Limansky mask, are shown in Figure 12. The result indicates that 50% modulation occurs at 12 line pairs/mm which is within the required specification.

Since our experimental apparatus did not permit us to reproduce this test at

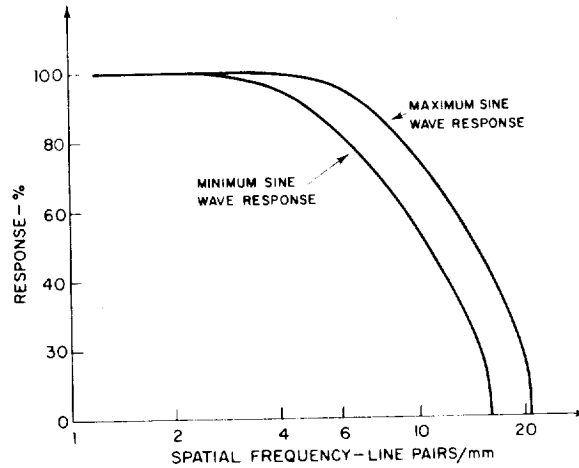


Fig. 12. The computed sine wave response of the vidicon.

X-ray wavelengths, we limited our studies of the total system response to the observation of its capability to resolve UV illuminated pinholes arranged in star patterns of varying sizes. The star patterns were placed at the focus of a 40-cm-diameter parabolic reflector to produce a collimated beam which was focussed by the X-ray mirror onto the MCP. The resulting images were displayed on a TV monitor. The tests showed that 3 arc second pinholes on 12 arc second centers could be resolved.

## 6. Conclusions

An electronic imaging system with a spatial resolution of better than 15 arc seconds has been designed and built from commercially available components for the observation of solar X-rays. The system was flown as part of a sounding rocket payload on 31 January, 1978. Unfortunately an interlock system, designed to prevent the MCP and the photographic camera from entering the focal plane at the same time, was activated during powered flight and prevented the MCP from leaving its stowed position. Consequently, no X-ray data were recorded. The images that were received showed the dark current patterns to be normal at both gain settings, and there is every reason to believe that satisfactory solar images would have been obtained if the MCP had been translated into the focal plane. The payload is scheduled for reflight in November, 1979.

In the introduction we indicated that one of the objectives of the development of electronic imaging systems was to replace the use of film as the recording medium in satellite experiments. If that goal is to be realized the resolution of the electronic imaging systems has to be improved by roughly an order of magnitude from that reported here, i.e., from approximately 10 to 1 arc second. This improvement is

essential because the detailed study of coronal phenomena requires a knowledge of the physical parameters of the plasma at this level.

The major factor limiting the resolution of systems of this type is the physical dimensions of the microchannels in the MCP. Although the technology exists for making glass channels with diameters down to 6 microns (a factor of 4 improvement over the present system), MCPs made with this size channel are reported by the manufacturers to have low gains. One suspects that within the immediate future 10 micron channels may be a practical limit. Charge coupled devices (CCDs) have also been proposed for X-ray detectors [19]. The most promising versions have square pixels with sides of 15 microns. CCDs have the advantage of a negligible dead space between pixels. However their sensitive areas are rather small; the largest CCDs currently planned, for instance, being  $800 \times 800$  arrays occupying an area of  $1.44 \text{ cm}^2$  [20]. In contrast MCPs are commercially available with circular sensitive areas in excess of  $44 \text{ cm}^2$ .

In the event that a limit to the pixel size exists at around 10 microns, the only alternative is to increase the focal length of the X-ray optical system. For instance the large space platforms, envisaged for the Shuttle era, will be capable of accommodating an instrument with a 5 m focal length. Such an instrument would have a plate scale of 24 microns per arc second and thus, with a channel size of 10 microns, angular resolution on the order of 1 arc second should be possible.

In conclusion, our experience indicates that even though electronic imaging systems are practical, if they are to replace film as the prime detector in the focal plane of high resolution solar X-ray imaging experiments, there will have to be modest improvements in the geometry of the detectors coupled with an increase in focal length of the optics. Our studies have shown that the sensitivity of electronic systems for X-ray detection is equal or superior to film. Therefore observations with improved time resolution will be possible since there will be no limitations on the number of images that can be recorded, provided that the telemetry systems are capable of handling the data rates. In summary, if the technological conditions are met, then the techniques of high resolution imaging using electronic detection will significantly augment our observational capabilities and will be extremely helpful in expanding our knowledge of coronal transient phenomena.

#### Acknowledgements

This project could not have been completed without the help of many individuals both within AS&E and throughout the industry. From among this large group we would, however, like to single out Dr Ann Hutchinson of GEC for her patience and her many helpful explanations, Mr Gary Bailey of JPL whose suggestions led to the preamplifier design and Mr Frank Hills of AS&E who developed the computer interface and software which formed an integral part of the instrument. One of us (JWT) would also like to thank Professor Denis Fermentat of Tufts University for

his guidance and encouragement. The work was supported by NASA under contract NAS2-8683.

### References

1. Vaiana, G. S., Reidy, W. P., Zehnpfennig, T., Van Speybroeck, L., and Giacconi, R.: *Science* **161**, 564 (1968).
2. Van Speybroeck, L. P., Krieger, A. S., and Vaiana, G. S.: *Nature* **227**, 818 (1970).
3. Vaiana, G. S., Krieger, A. S., and Timothy, A. F.: *Solar Phys.* **32**, 81 (1973).
4. Krieger, A. S., Davis, J. M., and Haggerty, R.: *Bull. AAS* **10**, 439 (1978).
5. Vaiana, G. S., Van Speybroeck, L. P., Zombeck, M. V., Krieger, A. S., Silk, J. K., and Timothy, A. F.: *Space Sci. Instrum.* **3**, 19 (1977).
6. Timothy, J. G.: *Space Sci. Instrum.* **2**, 289 (1976).
7. Galileo Electro-Optics Corp., Sturbridge, MA 01518, U. S. A.
8. Bjorkholm, P. J., Van Speybroeck, L. P., and Hecht, M.: *SPIE Proc.* **106**, 195 (1977).
9. Varian Vacuum Division, Waltham, MA 02154, U. S. A.
10. Raytheon Company, Microwave and Power Tube Division, Waltham, MA 02154, U. S. A.
11. Caruso, A. J.: *Applied Optics* **13**, 1744 (1974).
12. Henke, B. L., and Elgin, R. L.: *Advances in X-ray Analysis* **13**, 639 (1970).
13. General Electrodynamics Corp., Garland, TX 75042, U. S. A.
14. MIL Electronics, Inc., Lowell, MA 01854, U. S. A.
15. Velonex Division of Varian, Santa Clara, CA 95050, U. S. A.
16. Sallen, R. P., and Key, E. L.: *IRE Trans. Circuit Theory, CT-2*, 74 (1955).
17. Limansky, I.: 'A New Resolution Chart for Imaging Systems', *The Electronic Engineer*, June (1968).
18. Hall, J. A.: *Photoelectronic Imaging Devices*, Biberman, L. M. and Nudelman, S. (Eds.), Plenum Press, Vol. 2, 1971, p. 53.
19. Burstein, P., Krieger, A. S., Vanderhill, M. J., and Wattson, R. B.: *Proc. SPIE* **143**, 114 (1978).
20. Texas Instruments, Inc., Dallas, TX 75222, U. S. A.



4.5 Properties of Coronal Arches

John M. Davis and Allen S. Krieger

American Science and Engineering, Inc.  
Arlington, Massachusetts 02174

ORIGINAL PAGE IS  
OF POOR QUALITY



# PROPERTIES OF CORONAL ARCHES

JOHN M. DAVIS and ALLEN S. KRIEGER

*American Science and Engineering, Inc., Space Systems Division,  
37 Broadway, Arlington, MA 02174, U.S.A.*

(Received 6 May, 1980; in revised form 11 December, 1981)

**Abstract.** The properties of coronal arches located on the peripheries of active regions, observed during a sounding rocket flight on March 8, 1973, are discussed. The arches are found to overlie filament channels and their footpoints are traced to locations on the perimeters of supergranulation cells. The arches have a wide range of lengths although their widths are well approximated by the value  $2.2 \times 10^9$  cm. Comparison of the size of the chromospheric footprint with the arch width indicates that arches do not always expand as they ascend into the corona. The electron temperatures and densities of the plasma contained in the arches were measured and the pressure calculated; typical values are  $2 \times 10^6$  K,  $1 \times 10^9$  cm $^{-3}$ , and  $2 \times 10^{-1}$  dyne cm $^{-2}$ , respectively. The variation of these parameters with position along the length of the arch indicates that the arches are not in hydrostatic equilibrium.

## 1. Introduction

Observations of coronal X-ray and EUV emission (Vaiana *et al.*, 1973a, b; Tousey *et al.*, 1973; Noyes *et al.*, 1975) have shown that the topography of active regions can be described in terms of a hierarchy of loops or arches. Classified by their location within the active region they are:

(I) Loops of the active region core which connect regions of opposite polarity across the neutral line (Krieger *et al.*, 1971).

(II) Compact volume loops which surround the core and occupy a region somewhat larger in size than the H $\alpha$  or calcium plage (Švestka, 1976). The average pressure within this region decreases uniformly outward from the center (Davis *et al.*, 1975). The topography of such higher, often unresolved loops is well approximated by an extrapolation of the photospheric magnetic field using a potential field model (Poletto *et al.*, 1975).

(III) Loops which extend outward from the active region to form arcades that connect the compact volume to the surrounding photospheric field. The loops may provide connections between active regions (Chase *et al.*, 1976) or even between active regions on opposite sides of the equator (Švestka *et al.*, 1977).

A series of images which contained excellent examples of loops in category (III) were obtained on March 8, 1973, during a sounding rocket flight of a grazing-incidence X-ray telescope. The wavelength range of the images differs slightly from those obtained later with the S-054 experiment on Skylab (Vaiana *et al.*, 1974) for the short wavelength cutoff occurs at 8 rather than 3 Å. This is a characteristic of the surface material of the grazing incidence mirror (fused silica, chosen for its low scattering) and has the effect of reducing the contribution of the radiation from higher temperature material. The point response function of the mirror at 8 Å has a FWHM of about 2 arc sec while 50% of the energy

of the image of an on-axis point source is contained within a radius of 31 arc sec. The comparable values for the S-054 mirrors are 4 and 48 arc sec respectively and the difference between these two sets of specifications indicates the decreased scattering of the new mirror. The images were recorded on Eastman Kodak SO 212 film.

## 2. Morphological Properties of the Coronal Arcades

### 2.1. DETAILS OF THE ANALYSIS

The arcades containing the bright X-ray loops (identified by arrows in Figure 1a) are associated with the two active regions McMath 12259 and 12261. Their appearance at different exposure levels and through different wavelength filters is shown in Figure 1.

The X-ray images have been compared with both chromospheric spectroheliograms and photospheric magnetic field observations, using photographic overlay techniques, to study the correspondence between the structures seen at different levels in the solar atmosphere. The X-ray and H $\alpha$  observations were made at 18:00 UT on March 8 and the Ca K observations at 16:46 UT. The images can be overlaid either from a knowledge of the orientation of the X-ray images with respect to heliocentric north, determined from the measured roll orientation of the rocket payload, or by using features on the solar disk which are well separated and visible in all sets of images to manually align pairs of images. Both techniques allow pairs of images to be superimposed to an accuracy of  $\pm 1^\circ$  in rotation. The corresponding point to point uncertainty between different images then depends on their distance from Sun center. For features located in the McMath 12259 and 12261 active region complex, this uncertainty varies from  $\pm 3$  to  $\pm 12$  arc sec. To this must be added the uncertainty in superposing the solar limbs on the different images which is typically no worse than  $\pm 5$  arc sec. Adding the uncertainties quadratically leads to a range in the point to point uncertainties between  $\pm 6$  to  $\pm 13$  arc sec.

Efforts to obtain simultaneous magnetograms from a ground based observatory were foiled by inclement weather across the western United States. Although some data were obtained, no full disk magnetic field measurements were recorded before 17:00 UT on March 9, at which time data from the Mt. Wilson observatory are available. In an attempt to compare the X-ray observations with the photospheric magnetic field, the data from March 9 were used to reconstruct the photospheric magnetic field at the time of the rocket flight by correcting for solar rotation. Where information from KPNO exists it was used to cross-check the extrapolation. Since the magnetic field and X-ray data were obtained 23 hr apart any conclusions drawn from their comparison assume that the large scale features did not change significantly during that interval.

### 2.2. MORPHOLOGY OF CATEGORY (III) LOOPS

The category (III) loops occur in groups or arcades with the loops in each arcade separated from adjacent loops by a distance approximately equal to the loop's width. Comparison of the X-ray images with magnetograms (Figure 2) shows that the loops

ORIGINAL PAGE  
BLACK AND WHITE PHOTOGRAPH

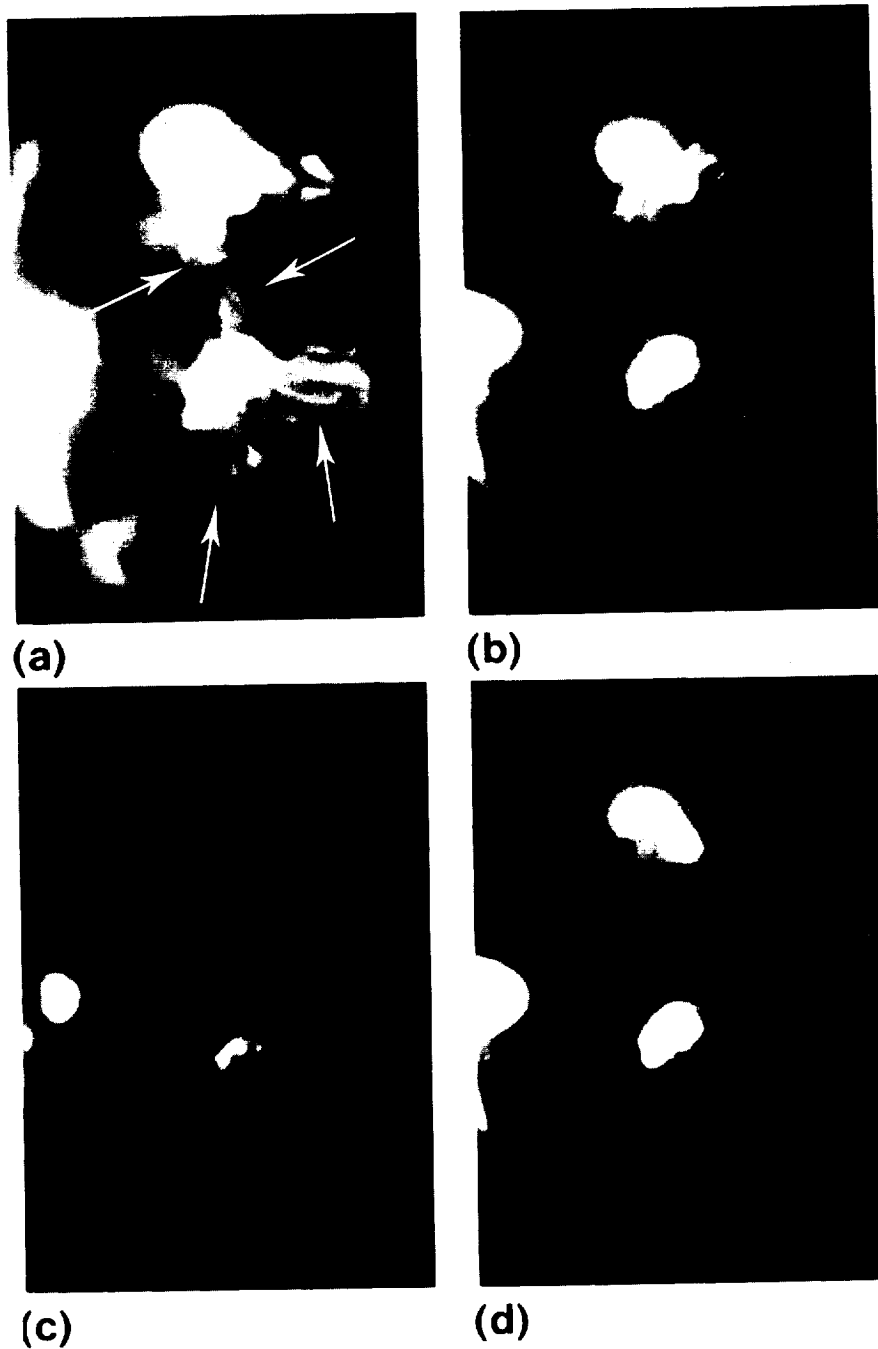


Fig. 1. The active region complex consisting of McMath 12259 (upper) and McMath 12261 (lower) observed at 18:00 UT on March 8, 1973. The coronal arches are indicated by arrows. The waveband and exposure levels are (a) 8-37, 44-60 Å, and 58.6 s; (b) 8-37, 44-60 Å, and 20.3 s; (c) 8-37, 44-60 Å, and 0.8 s; (d) 8-20 Å and 58.6 s.

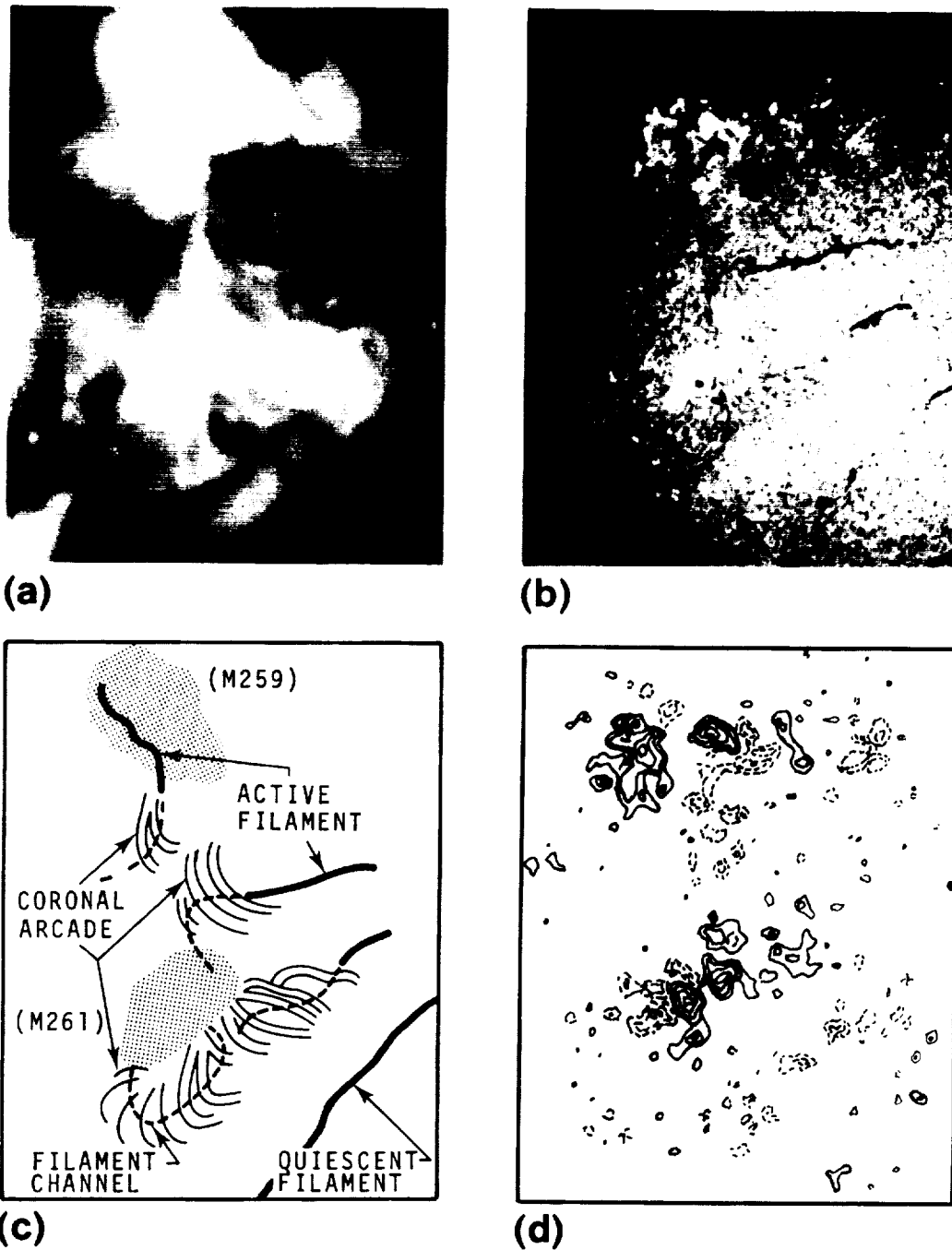


Fig. 2. The association of X-ray, H $\alpha$  and magnetic features. (a) X-ray image showing the arcades of bright loops and filament cavities. (b) Simultaneous H $\alpha$  photograph showing the location of the filaments and filament channels. (c) A schematic showing the location of coronal arcades above active filament channels. (d) The photospheric magnetic field obtained by correcting the Mt. Wilson magnetogram from 17:00 UT on March 9, 1973 for solar rotation.

emerge from localized areas within the active region where the field magnitude and gradients are high. The loops connect the field at the center of the active region to the surrounding background field and these connections are not restricted to fields originating on the same side of the equator. There is no preference for connecting to preceding or following polarity within the active region nor does the age of the active region appear to have any influence on the presence of arcades.

When the X-ray and H $\alpha$  images are overlaid the arcades of category (III) loops are found to be associated with active filaments. In particular the loops of each arcade span a particular filament thus forming a connection between areas which are separated by the neutral line of the longitudinal magnetic field.

The presence of these arcades creates a marked difference in the X-ray morphology of active and quiescent filaments. The latter, when seen in projection against the disk, appear as long, dark cavities surrounded by diffuse X-ray structures (Figure 2). Observations at limb crossings (Serio *et al.*, 1978) show that the cavities are closed by faint loops. The cavities contain little, if any, material at a high enough temperature to emit soft X-rays and have an average height of  $5 \times 10^9$  cm. In contrast the corresponding regions above the active filaments are the sites of the arcades of bright X-ray loops which are of a comparable height to the quiescent filament cavities.

In general the active filaments, seen in these images, extend into filament channels which show little or no H $\alpha$  absorption. However the channels do contain a neutral line around which the photospheric field shows the same orientation, interpreted from the fibril alignments, as the region surrounding the active filament. Close inspection of the overlaid images shows that the loops are located either above a filament channel or over a segment of the active filament where the H $\alpha$  absorption is weak. Loops are not present above strongly absorbing sections of the filament which are located beneath X-ray cavities similar to those found above quiescent filaments.

This contrast in X-ray morphology between the cavities observed above absorbing filaments and the bright loops above filament channels, with the loops occupying the same general volume as the cavities, provides circumstantial evidence for a connection between the appearance of bright X-ray loops and the subsequent development of a filament (Davis and Krieger, 1978, 1982).

The outer footpoints of the arches can be traced to localized brightenings in both the Ca K and H $\alpha$  spectroheliograms. Since adjacent loops have separations on the order of one arc minute and the images can be aligned to  $\pm 10$  arc sec, the identification of each loop with a specific brightening is relatively unambiguous even though the X-ray loops cannot be traced directly to the chromosphere. In Ca K the brightenings appear as enhancements of the normally bright boundaries of the supergranulation network (Figures 3 and 4). Only a segment of the network perimeter is enhanced suggesting that the loops are anchored to localized areas where the magnetic flux, concentrated by the convective motions in the cell, is dense, well ordered or both. In H $\alpha$  the brightenings appear as groups of bright convection cells with the surrounding fibrils aligned perpendicularly to their major axes, confirming that the footpoints are localized sections of the cell boundary. In one case (McMath 12259) two arches appear to originate from

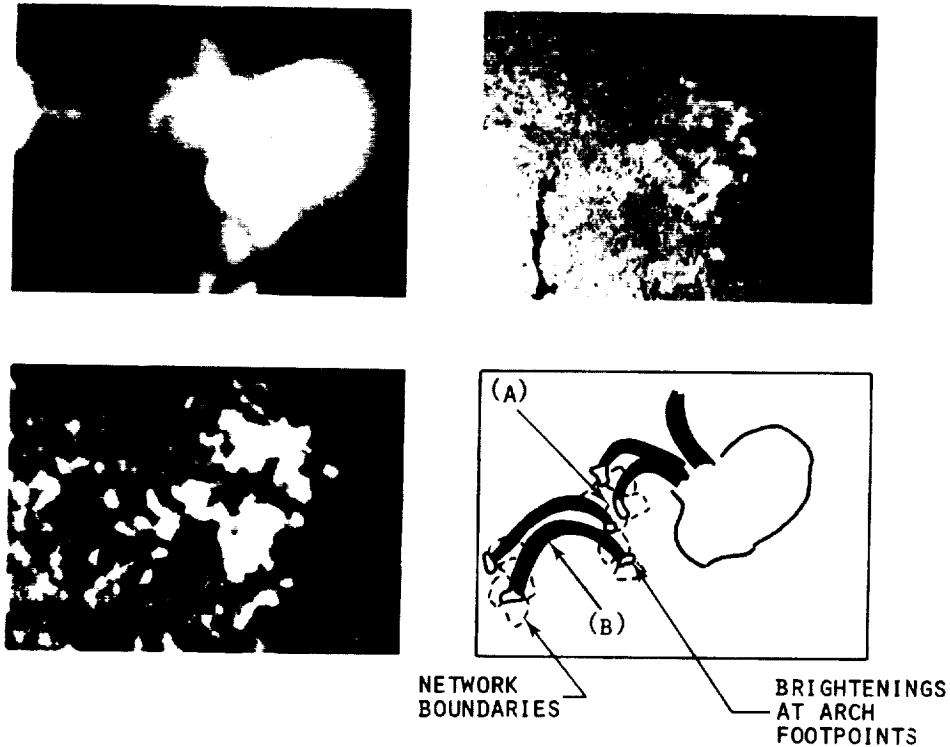


Fig. 3. X-ray, H $\alpha$  and Ca K images of McMath 12259 showing the termination of loops from different arcades in the same supergranulation cell (*A*) and the X-ray loop (*B*) which has neither termination within the compact volume of an active region.

opposite sides of the same network cell (identified as *A* in Figure 3). These arches are components of two separate arcades and there appear to be no cases where arches from the same system terminate in the same cell.

### 3. Properties of Individual Arches

#### 3.1. PHYSICAL DIMENSIONS

The physical dimensions, length and breadth, of individual category (III) arches were measured from the X-ray images. The arch lengths were measured directly and were corrected for projection effects resulting from both their position on the solar surface and their vertical extension. To determine the widths, the images were digitized, using a 3 arc sec square aperture, converted into incident energy and deconvolved to remove the effect of the telescope point response function. Sections were made across each arch at several locations and an average made of the measured full widths. The cross-sections

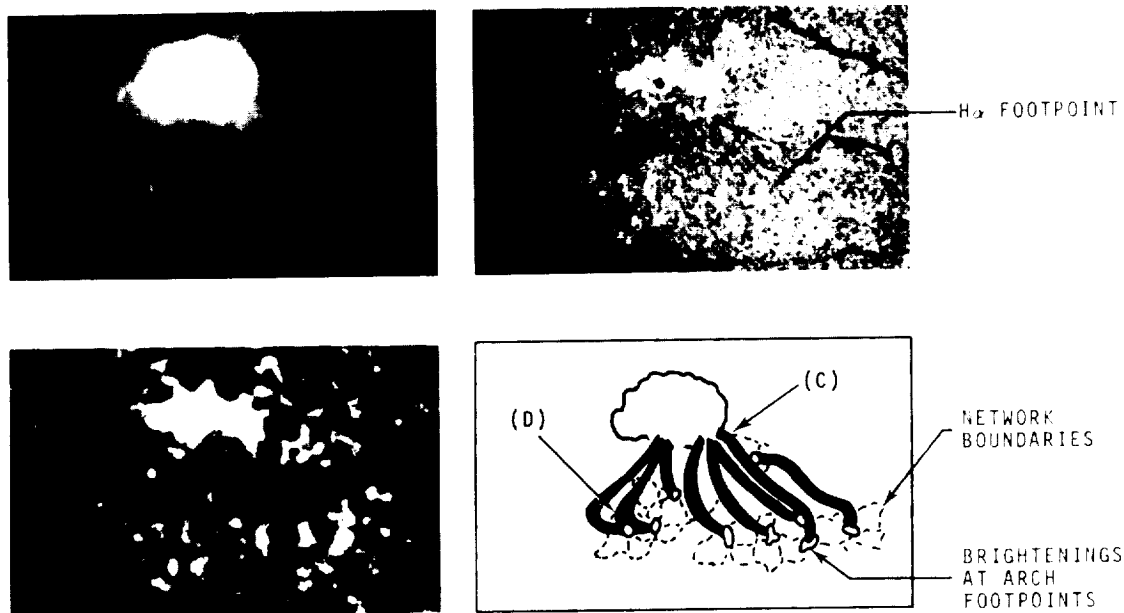


Fig. 4. X-ray, H $\alpha$ , and Ca K images of McMath 12261 showing the location of the arch footpoints in network brightenings and identifying the arches (C) and (D) whose properties are described in the text.

did not show any evidence of structure within the arch; however, the resolution of the telescope-film system is marginal for revealing the structure of emitting features at or below 15 arc sec unless they are accompanied by substantial intensity or temperature gradients.

Inspection of the data reveals the following points:

(i) The width and length distribution of the individual arches have lower limits of  $1.5 \times 10^9$  and  $5 \times 10^9$  cm, respectively. The dimensions of the arches are comparable to those of loop-prominence systems.

(ii) Arch widths appear to be independent of their lengths and are well approximated by a single, average, value of  $2.2 \pm 0.3 \times 10^9$  cm.

By comparison the loops of categories (I) and (II) are typically both shorter and narrower. The ranges of values of all three categories are summarized in Table I.

TABLE I  
Dimensions of active region loops

	Category (I) Active region cores	Category (II) Compact volume loops	Category (III) Outward extending loops
Width-cm	$7 \times 10^7 - 5 \times 10^8$	$5 \times 10^8 - 1.5 \times 10^9$	$1 \times 10^9 - 3 \times 10^9$
Length-cm	$7 \times 10^8 - 2 \times 10^9$	$1 \times 10^9 - 1 \times 10^{10}$	$5 \times 10^9 - 5 \times 10^{10}$

It has been suggested that the lengths of individual arches may be governed by a stability condition which equates the time scales for conduction and radiation (Tucker, 1973). By expressing the time scale for conduction in terms of the thermal diffusion coefficient for Coulomb collisions parallel to the magnetic field (Spitzer, 1962), and following Tucker and Koren (1971) for the radiative energy loss, the maximum length,  $L_{\max}$ , of an arch can be written as

$$L_{\max} \simeq 2.9 \times 10^5 \frac{T^{9/4}}{n_e} \text{ cm ,}$$

where  $T$  is the temperature in degrees K and  $n_e$  is the electron density in  $\text{cm}^{-3}$ .

The arches have observed densities between 0.7 and  $1.2 \times 10^9 \text{ cm}^{-3}$  and temperatures between 1.8 and  $2.5 \times 10^6 \text{ K}$ . These values correspond to maximum lengths ranging from  $2 \times 10^{10}$  to  $1 \times 10^{11} \text{ cm}$ . None of the observed arches exceed this limit and in general their measured lengths are less, by a factor of 2, than their respective limit.

### 3.2. THE STRUCTURE OF THE BASE OF CORONAL ARCHES

If the area of enhanced network identified with the footpoints of the coronal arches defines the chromospheric cross-section of the loop, then the change in the cross-section of the loop as it rises into the corona can be determined. Although the chromospheric brightenings have rather irregular shapes they are elongated along the network boundary. Consequently their cross-sections can be characterized by major and minor axes. The measured lengths of each set of axes, after correction for their projection on the solar disk, were found to vary over a factor of three. Since the X-ray cross-sections are roughly constant for all loops, the expansion of the loops from the chromosphere into the corona, for this data set, is inversely proportional to the size of the chromospheric major axis, when this parameter is used to characterize the size of the footpoint. Expansion factors varied from 0.8 to 3.2 with 40% of the loops showing a contraction rather than an expansion. Therefore we conclude that on average the loops tend to maintain the same cross-section as they ascend into the corona.

This result is contrary to the generally accepted view that the field lines at supergranule boundaries and hence by inference the field lines within loops diverge as they ascend into the corona (Pneuman and Kopp, 1978; Kopp and Kuperus, 1968). The observational results might be in error if the downward conducted energy from the coronal arch, which is assumed to be responsible for the chromospheric brightening, is greater than the energy density at this level of the chromosphere. In this case the excess energy may be transported into adjacent convection cells, creating an apparent increase in the size of the footpoint. The evaluation of conductive fluxes in the transition zone is difficult (see Athay, 1976), however the steep temperature gradient will have substantially reduced the flux at the level corresponding to  $\text{H}\alpha$  emission, say  $T = 10^4 \text{ K}$ , compared to the flux at the base of the corona. An order of magnitude calculation indicates that the conductive flux is not a significant fraction of the energy density and since at  $10^4 \text{ K}$  the radiative loss function has an extremely steep temperature dependence (Cox and

Tucker, 1969) the plasma at the base of the arch will easily adjust to a small increase in the energy input. Therefore we feel justified in assuming that the network brightening reflects the true loop cross-section and therefore that ascending loops are not automatically characterized by an increasing diameter.

### 3.3. PLASMA PARAMETERS AND HYDROSTATIC EQUILIBRIUM

When images are obtained through two filters with different wavelength passbands, it is possible to determine an average line of sight electron temperature,  $T$ , and emission measure,  $\int n_e^2 dl$  (Vaiana *et al.*, 1973b; Davis *et al.*, 1975). In the present study the images were converted into deconvolved energy arrays consisting of 3 arc sec by 3 arc sec image elements. The ratio, at any element point, of two such array values taken through different filters, provides a measure of the average line of sight temperature which can then be used to evaluate the emission measure at the same location from one of the images.

To evaluate the electron density, it is necessary to make assumptions about the structure of the emitting region along the line of sight. For the X-ray arches we have assumed that the emitting material is distributed uniformly within a circular cross-section and that the integrated line of sight density of the material emitting X-rays either above or below the arch is negligible. The electron density,  $n_e$ , can then be evaluated from the emission measure by dividing the latter quantity by the measured width of the arch at each point.

Where the parameters are presented as a function of position along the longitudinal axis of the arch, average energy arrays were formed from the pairs of image elements on either side of the axis. Ratios of these averaged arrays were used to obtain temperatures and densities which were then smoothed by forming the running average, along the axis, of pairs of values. Thus each value corresponds to a 6 arc sec by 6 arc sec area. Although the absolute values of the points may be subject to unknown systematic errors, the relative uncertainty between adjacent points is of the order of 2 to 3% and consequently the trends that are evident in the data are significant.

The measurements show that the loops have average temperatures of  $2.1 \pm 0.2 \times 10^6$  K and densities of  $1.0 \pm 0.2 \times 10^9$  cm<sup>-3</sup>. The material between the arches is both cooler and less dense. The upper limits placed on the temperature and density are  $1.5 \times 10^6$  K and  $1 \times 10^8$  cm<sup>-3</sup>. When the variation of the temperature with position along the longitudinal axis of the arches is studied, the arches are found to fall into two groups distinguished by temperature variations which are either approximately constant with position or which decrease steadily with distance from one termination; the latter temperature distributions are directly correlated with the location of the higher temperature termination within the compact volume of the active region.

When both footpoints lie outside the compact volume the data has the form shown in Figure 5 which shows the variation with position of the electron density and temperature for the arch identified as *B* in Figure 3. The pressure,  $n_e kT$ , has been calculated from the measured quantities and increases smoothly to a maximum, approximately 20% above the base value, at the center of the arch before decreasing. The pressure maximum

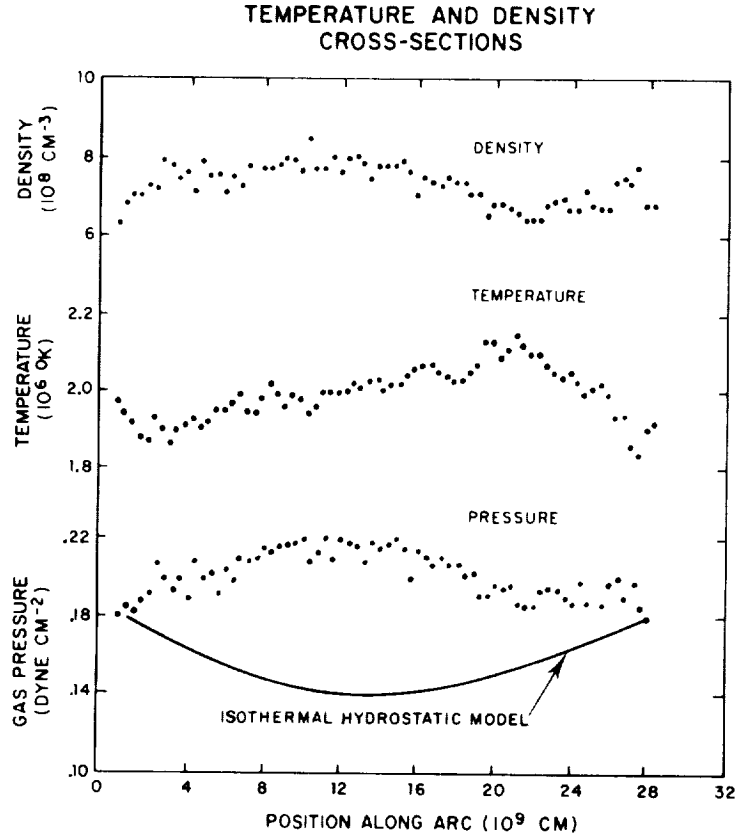


Fig. 5. The observed temperature, density and pressure profiles along the arch (B) of Figure 3. The solid curve depicts the pressure profile that would be obtained if the arch was isothermal and in hydrostatic equilibrium.

occurs in the vicinity of the peak, or highest vertical extension, of the arch which is estimated to be  $5 \times 10^4$  km above the base of the corona.

If the arch were in hydrostatic equilibrium and its temperature distribution were truly isothermal, the pressure within the arch would decrease exponentially with a scale height

$$H_0 = \frac{2kT}{\mu m_H g_0},$$

where  $\mu$  is the mean molecular weight of the plasma and the other constants have their usual meaning. Substituting the measured altitude profile of the arch into the exponential model and using an average temperature of  $2 \times 10^6$  K to calculate the scale height, the solid curve of Figure 5 is obtained. The difference between the predicted curve and the actual data is quite dramatic and illustrates that even seemingly stable arches do not necessarily exist in hydrostatic equilibrium.

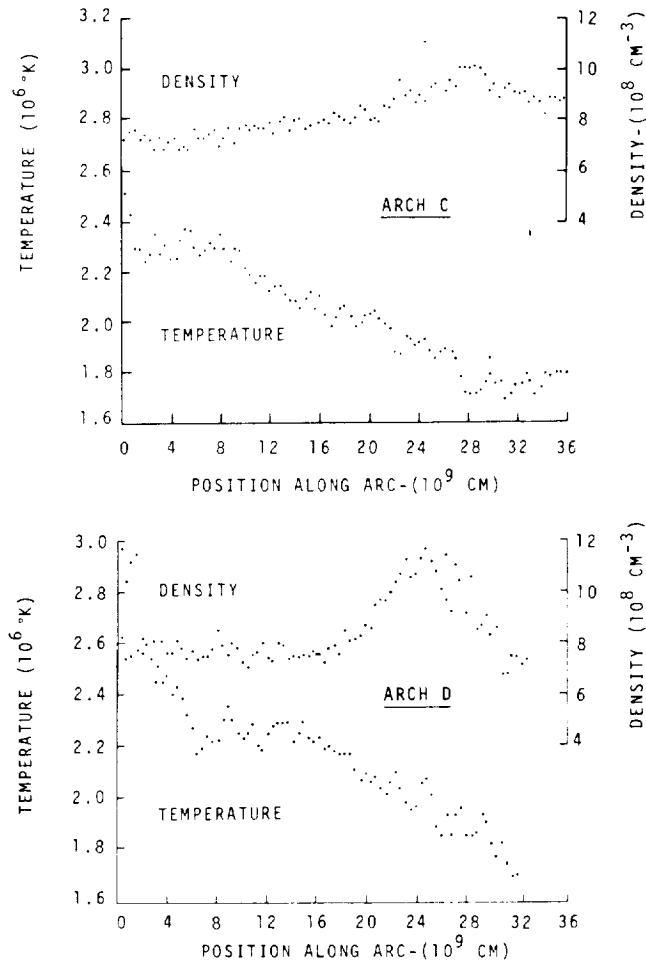


Fig. 6. Temperature and density profiles along the arches (C) and (D) of Figure 4 showing (a) the linear temperature decline with distance from the active region and (b) the density enhancement described in the text.

The observation that loops exist in non-hydrostatic equilibrium agrees with the observations of Foukal (1976) for the much cooler loops ( $10^4 < T < 10^6$  K) associated with sunspots, but is in contrast to the assumption made in several theoretical papers (e.g., Rosner *et al.*, 1978) where hydrostatic equilibrium has been used as the starting point in the development of a theoretical description of the geometry and thermal stability of X-ray loops.

When one of the footpoints lies within the active region the longitudinal variations of the temperature and density are similar to Figure 6 which shows the data for the loops identified as (C) and (D) in Figure 4. In both cases the temperature decreases linearly outward from the active region with a longitudinal temperature gradient between  $2-3 \times 10^{-3}$  deg K  $m^{-1}$ . In general the density increases slightly over the same distance

(Figure 6, above) although not sufficiently to compensate for the falling temperature in the pressure term which also decreases from one end of the arch to the other.

The second example (Figure 6, below) belongs to an arcade where several of the arches have bright knots at or near their apices. The analysis shows that the knots owe their increased brightness to a substantial increase in density. The knot in the example shown has a volume of  $1.5 \times 10^{28} \text{ cm}^3$ , a density of  $1.2 \times 10^9 \text{ cm}^{-3}$ , which is 50% above the value for the rest of the arch, and a mass of  $3 \times 10^{13} \text{ g}$ . We have rejected the hypothesis that the density increase is simply a projection effect because we are unable to duplicate the observed intensity distribution by numerically modelling the expected distribution for a variety of possible geometries. If this identification is correct then the violation of hydrostatic equilibrium is even more severe in this arch and its neighbors in the arcade which show the same characteristic.

#### 4. Conclusions and Discussion

Observations have been made of a category of coronal arches found on the periphery of active regions. The arches are associated with active filaments and they occur above filament channels rather than above regions where the  $H\alpha$  absorbing filament is clearly defined.

The terminations of the arches, where they are visible outside the active region, have been projected to locations on the boundaries of supergranulation cells. These locations are characterized by brightenings in  $H\alpha$  and if the bright areas are an accurate representations of the cross-section of the arch at this level in the solar atmosphere there is no clear evidence for a general expansion of arches as they ascend into the corona.

The arches were found to have a wide range of lengths coupled with a narrow distribution of widths which is well approximated by a single average value of  $2.2 \times 10^9 \text{ cm}$ .

The electron temperature, density and pressure of the material in the arches has been measured and typical average values are  $2 \times 10^6 \text{ K}$ ,  $1 \times 10^9 \text{ cm}^{-3}$  and  $2 \times 10^{-1} \text{ dyne cm}^{-2}$ , respectively. The coronal material surrounding and between arches is less dense, cooler and at a lower pressure than the material within arches. By determining the variation of these parameters along the longitudinal axis of the arch, i.e., as a function of altitude and in some cases as a function of distance from the active region, it was found that, in general, the material within the arches was not in hydrostatic equilibrium. Secondly, for those arches with one of their terminations lying within the compact volume of the active region, there existed an outward temperature gradient which is perhaps indicative of outward energy conduction from the center of the active region.

Arches were also observed with substantial density enhancements at their apices. It is tempting to interpret the enhancements as evidence of coronal condensations occurring within loops. Since the same arches are located above filament channels the obvious corollary is that the condensations are responsible for the subsequent development of a filament. This possibility has been explored in a companion paper (Davis and Krieger, 1982).

### Acknowledgements

The help and assistance of the AS & E Rocket Group and of the Sounding Rocket Division of the Goddard Space Flight Center in the launch of research rocket 13.027 is gratefully acknowledged. It is also a pleasure to acknowledge the help and encouragement provided by Dr Giuseppe Vaiana during the early stages of the work and the assistance of Ms Jadwiga Zmijewski in the photographic analysis.

The experimental observations were supported by NASA under contract NAS2-7424 and the analysis by NASA under contracts NAS2-8683 and NAS5-25496.

### References

- Athay, R. G.: 1976, *The Solar Chromosphere and Corona: Quiet Sun*, D. Reidel Publ. Co., Dordrecht, Holland, p. 406.
- Chase, R. C., Krieger, A. S., Švestka, Z., and Vaiana, G. S.: 1976, *Space Res.* **16**, 917.
- Cox, D. P. and Tucker, W. H.: 1969, *Astrophys. J.* **157**, 1157.
- Davis, J. M. and Krieger, A. S.: 1978, *Bull. Am. Astron. Soc.* **10**, 439.
- Davis, J. M. and Krieger, A. S.: 1982, *Solar Phys.*, (in press).
- Davis, J. M., Gerassimenko, M., Krieger, A. S., and Vaiana, G. S.: 1975, *Solar Phys.* **45**, 393.
- Foukal, P. V.: 1976, *Astrophys. J.* **210**, 575.
- Kopp, R. A. and Kuperus, M.: 1968, *Solar Phys.* **4**, 212.
- Krieger, A. S., Vaiana, G. S., and Van Speybroeck, L. P.: 1971, in R. Howard (ed.), 'Solar Magnetic Fields', *IAU Symp.* **43**, 397.
- Landini, M., Monsignori-Fossi, B. C., Krieger, A. S., and Vaiana, G. S.: 1975, *Solar Phys.* **44**, 69.
- Noyes, R. W., Foukal, P. V., Huber, M. C. E., Reeves, E. M., Schmahl, E. J., Timothy, J. G., Vernazza, J. E., and Withbroe, G. L.: 1975, in S. Kane (ed.), 'Solar Gamma, X-, and EUV Radiation', *IAU Symp.* **68**, 3.
- Pneuman, G. W. and Kopp, R. A.: 1978, *Solar Phys.* **57**, 49.
- Poletto, G., Vaiana, G. S., Zombeck, M. V., Krieger, A. S., and Timothy, A. F.: 1975, *Solar Phys.* **41**, 83.
- Rosner, R., Tucker, W. H., and Vaiana, G. S.: 1978, *Astrophys. J.* **220**, 643.
- Serio, S., Vaiana, G. S., Godoli, G., Motta, S., Pirronello, V., and Zappala, R. A.: 1978, *Solar Phys.* **59**, 65.
- Spitzer, L.: 1962, *Physics of Fully Ionized Gases*, (2nd edition), Interscience, New York.
- Švestka, Z.: 1976, in 'International Symp. on Solar-Terrestrial Physics', *Physics of Solar Planetary Environments*, Vol. I, p. 129.
- Švestka, Z., Krieger, A. S., and Chase, R. C.: 1977, *Solar Phys.* **52**, 69.
- Tousey, R., Bartoe, J. D. F., Bohlin, J. D., Bruechner, G. E., Purcell, J. D., Scherrer, V. F., Sheeley, N. R., Schumacher, R. J., and Van Hoosier, M. E.: 1973, *Solar Phys.* **33**, 265.
- Tucker, W. H.: 1973, *Astrophys. J.* **186**, 285.
- Tucker, W. H. and Koren, M.: 1971, *Astrophys. J.* **168**, 283.
- Vaiana, G. S., Davis, J. M., Giacconi, R., Krieger, A. S., Silk, J. K., Timothy, A. F., and Zombeck, M.: 1973a, *Astrophys. J.* **185**, L47.
- Vaiana, G. S., Krieger, A. S., and Timothy, A. F.: 1973b, *Solar Phys.* **32**, 31.
- Vaiana, G. S., Krieger, A. S., Petraso, R., Silk, J. K., and Timothy, A. F.: 1974, *Proc. SPIE* **44**, 185.



4.6 The Growth of Filaments by the Condensation of Coronal Arches

John M. Davis and Allen S. Krieger

American Science and Engineering, Inc.  
Cambridge, Massachusetts 02139

ORIGINAL PAGE IS  
OF POOR QUALITY



# THE GROWTH OF FILAMENTS BY THE CONDENSATION OF CORONAL ARCHES

JOHN M. DAVIS and ALLEN S. KRIEGER

*American Science and Engineering, Inc., Cambridge, Mass. 02139, U.S.A.*

(Received 11 December, 1980; in revised form 16 April, 1982)

**Abstract.** A model of filament formation based on the condensation of coronal arches is described. The condensation results from initiating the radiative instability within an arch by superimposing a transient energy supply upon the steady state heating mechanism. The transient energy supply increases the density within the arch so that when it is removed the radiative losses are sufficient to lead to cooling below the minimum in the power loss curve.

Times from the initial formation of the condensation to its temperature stabilization as a cool filament have been calculated for various initial conditions. They lie in the range  $10^4$  to  $10^5$  s with the majority of the time spent above a temperature of  $1 \times 10^6$  K.

Under the assumption that the condensation of a single arch forms an element of the filament, a complete filament requires the condensation of an arcade of loops. Using experimentally derived parameters, filament densities of  $10^{11}$  to  $10^{12}$   $\text{cm}^{-3}$  can be obtained.

## 1. Introduction

### 1.1. BACKGROUND

X-ray observations of the solar corona have shown that arcades of X-ray loops situated on the boundaries of active regions are frequently located above active filament channels (Davis and Krieger, 1982). The archetypal example is the active filament complex, consisting of filaments and filament channels, observed to the SE of McMath 12261 between 7 and 9 March 1973 (Figure 1). At the start of the observations the filament channel has an elliptical shape which shows little change for 24 hr. The X-ray observations, taken at this time, show that the filament channel is located directly beneath an arcade of loops having bright knots at their summits, which are the result of a local increase in the electron density. During the following 24 hours a filament is observed to develop within the channel. The observations suggest that filaments form out of coronal arches and it is tempting to identify the bright knots with the density perturbations proposed by Hildner (1974), Raadu and Kuperus (1973), and others (see Tandberg-Hanssen, 1974) to describe the initial stage of filament formation.

In these models a density perturbation grows and cools because the radiative losses are proportional to  $n_e^2$  and  $T^{-1}$ ; thus, the cooling produces a decrease in pressure, and the resulting compression by the surrounding medium will produce a further increase in density and increased cooling. The additional energy needed to halt this cycle cannot be supplied by the surrounding medium because conduction across the field lines, running through the perturbation, is inhibited. These models require a large initial compression to start the cooling cycle so that it will proceed fast enough to account for

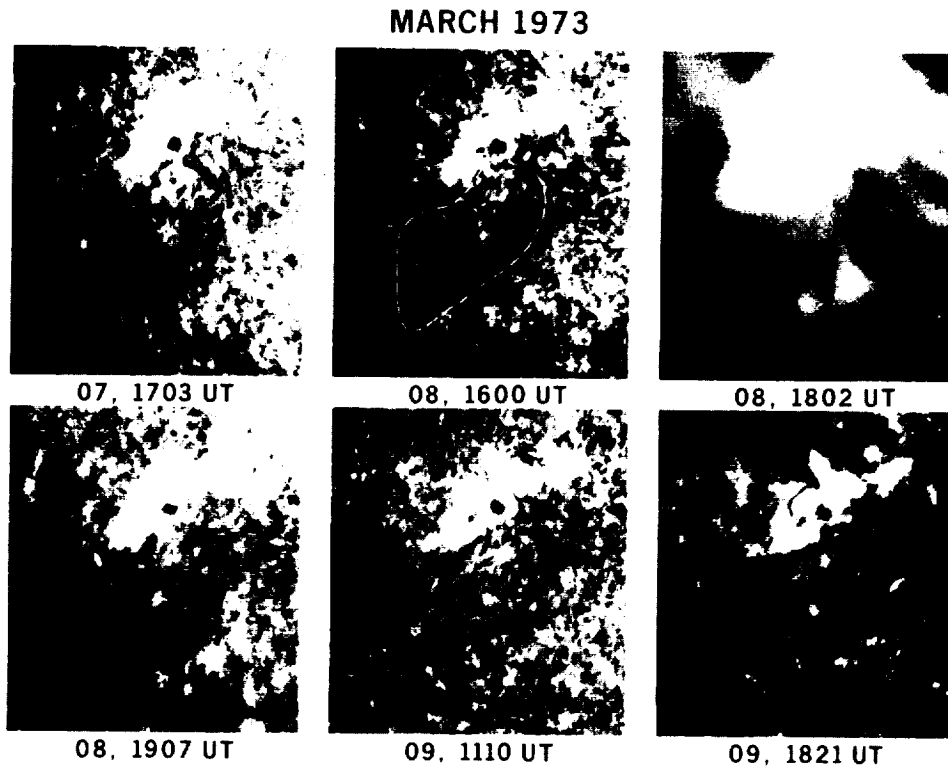


Fig. 1. The growth of an active filament associated with McMath 12261. The H $\alpha$  images show the development of the filament, outlined in frame 2, between 17:03 UT on 7 March 1973 and 18:21 UT on 9 March. (H $\alpha$  images courtesy of NOAA, Boulder, USAF Palehua, and the Canary Islands Observatories.)

the time scale of formation of active filaments (Tandberg-Hanssen, 1974). As an empirical alternative we have investigated a model based on initiating the radiative instability within a coronal arch by providing a transient increase in the energy supplied to the arch.

#### 1.2. MODEL

The model is based on the thermal equilibrium of active region arches described by Pye *et al.* (1978). They considered arches in their initial state to be essentially empty flux tubes which undergo a rapid rise in temperature when energy is deposited within the tube. Since their low density limits radiation, conduction becomes the dominant loss mechanism. The result is a transfer of the energy to the arch footpoints located in the lower atmosphere. The material at the footpoints responds to this conductive energy input by 'evaporating' into the flux tube, i.e., its increase in temperature, and therefore in scale height, allows it to rise into the flux tube (Rosner *et al.*, 1978). The subsequent increase in density within the arch increases the radiative losses and leads to an

ORIGINAL PAGE  
BLACK AND WHITE PHOTOGRAPH

equilibrium or steady state condition in which the radiative and conductive losses balance the rate of energy deposition.

Now consider the effect on the equilibrium condition of an additional, transient energy input. Initially the temperature of the arch will rise and the radiative losses,  $P_{\text{rad}}$ , which are inversely proportional to temperature under coronal conditions (Cox and Tucker, 1969; McWhirter *et al.*, 1975), will decrease while the conductive losses,  $P_{\text{cond}} \sim T^{5/2}$ , increase. Thus the energy of the transient source will be transferred via conduction to the lower atmosphere which will respond by evaporating additional material into the arch until a new equilibrium is reached in which the increase in the radiative losses balances the power supplied by the transient source. After the transient supply is turned off, the arch will be losing more energy than it is receiving and its temperature will start to fall; but since  $P_{\text{rad}} \sim T^{-1}$  at coronal temperatures, the classical conditions for the

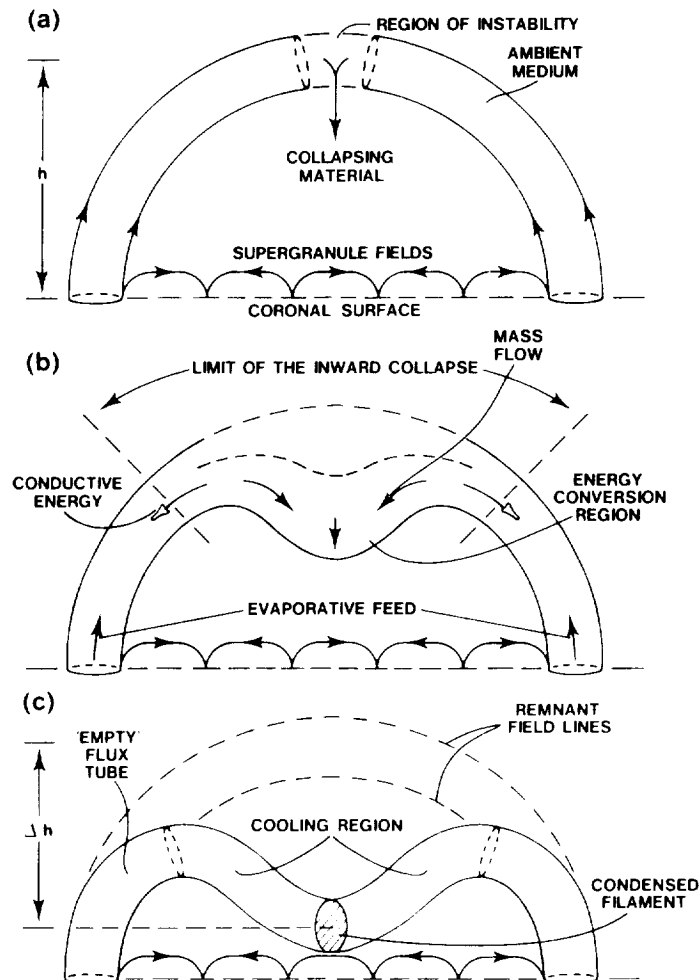


Fig. 2. A pictorial representation of the sequence of events which lead to the condensation of a coronal arch into an element of a filament.

radiative instability *may* be met. If they are, the temperature will continue to fall until a new balance is established. This occurs when the radiative losses equal the energy supply for as the temperature falls  $P_{\text{cond}}$  tends to zero.

To establish this sequence of events the arch must have a geometry which prevents the cooling material from immediately dissipating. For instance, if the radiative instability is established within the original magnetic configuration of the arch, the cooling material could return directly to the lower atmosphere without destroying the magnetic configuration of the arch (Pye *et al.*, 1978). The arch could then refill with material at a later time (Levine and Withbroe, 1977). Therefore the relationship between the transient supply and the geometry within which it is dissipated is important to the success of the model.

Observations have not identified the transient energy source. However the arches proposed as the source of the filament material extend to much greater heights than the resulting filaments. If the final configuration of the filament has the form proposed by Kippenhahn and Schlüter (1957) the arches must at least partially collapse to reach this state. If the collapse *precedes* the condensation, the release of potential energy during the collapse is itself a transient energy source and this assumption has been used to quantify the model. These ideas are shown schematically in Figure 2.

## 2. The Energetics and Time Scales for Filament Formation

To calculate the properties of a filament formed by this mechanism and to predict the time scales of formation as a function of the incremental density provided by the transient supply, the equations governing the initiation of the radiative instability in the presence of the external supply and conduction along the arch have been developed. To evaluate these equations, a standard arch has been defined (Table I) using experimentally determined values for the plasma parameters.

### 2.1. THE INCREMENTAL DENSITY REQUIRED TO OVERCOME CONDUCTION STABILIZATION

Coronal arches exist in a state of dynamic equilibrium in which a balance is maintained between the heating supply and the conductive and radiative losses. The balance is

TABLE I  
Physical parameters of the standard isothermal arch based on the observations of Davis and Krieger (1982)

Length	$l$	$3.0 \times 10^{10}$ cm
Radius	$r$	$1.1 \times 10^9$ cm
Electron density	$n_e$	$1.2 \times 10^9$ cm <sup>-3</sup>
Electron temperature	$T_e$	$2.0 \times 10^6$ K
Electron pressure	$P_e$	$3.3 \times 10^{-1}$ dyne cm <sup>-2</sup>
Cross section area	$A$	$3.8 \times 10^{18}$ cm <sup>2</sup>
Volume	$V$	$1.1 \times 10^{29}$ cm <sup>3</sup>
Height	$h$	$5.0 \times 10^9$ cm
Scale height	$H_0$	$2.0 \times 10^{10}$ cm
Sound speed	$V_s$	$1.3 \times 10^8$ cm s <sup>-1</sup>

maintained by adjusting the density of the arch by either evaporating from, or returning material to the lower atmosphere (Pye *et al.*, 1978). Once the arch is established within a conduction dominated regime, the equilibrium can be maintained by slight adjustments of its temperature. Consequently, if a positive density perturbation develops within an arch and attempts to cool due to its increased radiative losses, the cooling will be limited because conduction from adjacent regions in the arch connected by the same field lines will compensate for the increased radiative losses. This can be visualized with the aid of Figure 3 which is a schematic representation of the power loss of a coronal arch as a function of temperature. The major loss terms are radiation and conduction and the total loss curve is defined by the relation

$$P_{\text{total}}(T) = P_{\text{cond}}(T) + P_{\text{rad}}(T), \quad (1)$$

where  $P_{\text{rad}}(T)$  is the energy radiated by the whole arch and  $P_{\text{cond}}(T)$  is the energy lost through both footpoints when the material in the arch is at temperature  $T$ . When the arch is maintained in equilibrium by the steady state energy supply, it will exist on the conduction dominated branch of the total loss curve where an increase in temperature is accompanied by an increase in total losses. Increasing the arch density will increase the radiative losses at any temperature, thus moving the minimum loss point of the curve toward higher temperatures. However if  $P_{\text{total}} = P_{\text{source}} = \text{constant}$ , then if  $P_{\text{rad}}$  in-

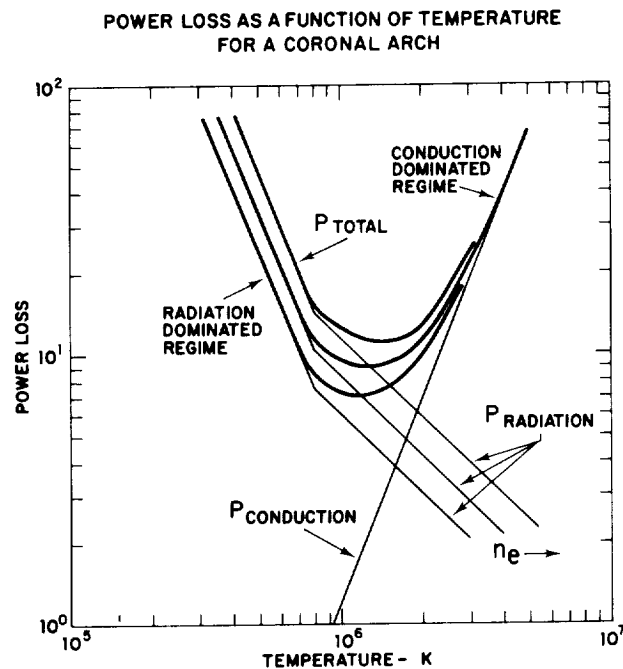


Fig. 3. A schematic diagram showing the dependence of the power losses of a coronal arch on its temperature. Since the functional dependence of the conductive and radiative losses have different signs, the total power loss curve exhibits a minimum at a temperature given by Equation (5).

creases, due to an increase in density,  $P_{\text{cond}}$  must decrease. This implies a reduction in temperature of the arch. Thus the net result of an increase in density will be a slight cooling of the whole loop. The new equilibrium temperature will be closer to the minimum loss temperature since the latter will have moved to a higher temperature. To establish the radiative instability, the increase in density must be sufficient to drive the arch through the minimum in the total power loss curve onto the radiation dominated branch, where a decrease in temperature increases the total losses, thus precipitating further decreases in temperature.

Following Jordan (1976) and assuming that conduction occurs uniformly across the cross-section of the arch, the conduction losses through both ends of the arch are given by

$$P_{\text{cond}}(T) = 1.6 \times 10^{-10} (2\pi r^2) (T^{5/2} - T_b^{5/2}) \approx k_c T^{5/2}, \quad (2)$$

where  $T_b$  is the temperature at the base of the arch and is on the order of  $2-5 \times 10^4$  K. Although Equation (2) is strictly valid only for  $T_b \geq 10^5$  K, the effect of neglecting  $T_b$  has little impact on  $P_{\text{total}}$  for, by the time a temperature is reached where the value of  $T_b$  has any effect on the magnitude of the conductive losses, the latter are less than 1 percent of the radiative losses.

Above  $8 \times 10^5$  K the radiative losses (Hildner, 1974) are

$$\begin{aligned} P_{\text{rad}}(T) &= 5.5 \times 10^{-17} n_e^2 V T^{-1} \\ &= k_r T^{-1}. \end{aligned} \quad (3)$$

Therefore the total loss curve is given by

$$P_{\text{total}}(T) = k_c T^{5/2} + k_r T^{-1}. \quad (4)$$

This function will have a minimum at a temperature given by

$$T_{\text{min}} = \left( \frac{2k_r}{5k_c} \right)^{2/7} = (6.9 \times 10^{-8} n_e^2 l)^{2/7}. \quad (5)$$

Consequently, to establish the radiative instability and cool the arch below  $T_{\text{min}}$ , the added density,  $\Delta n_e$ , must be sufficient to increase the radiative losses so that the total losses at  $T_{\text{min}}$ , i.e.,  $P_{\text{total}}(T_{\text{min}})$ , exceed the energy input to the arch evaluated at the steady state condition. Thus

$$P_{\text{rad}}(n_e + \Delta n_e, T_{\text{min}}) + P_{\text{cond}}(T)_{\text{min}} \geq P_{\text{source}}(n_e, T). \quad (6)$$

By expressing  $P_{\text{source}}$  in terms of the conductive and radiative losses at the steady state temperature, and evaluating the LHS of Equation (6) using Equations (4) and (5), Equation (6) can be solved for  $\Delta n_e$ . Thus

$$\begin{aligned} \Delta n_e \geq [n_e^{4/7} l^{-5/7} (9.0 \times 10^{-3} n_e^2 l T^{-1} + 5.2 \times 10^4 T^{5/2} - \\ - 0.4 n_e^{10/7} l^{5/7})]^{1/2} - n_e. \end{aligned} \quad (7)$$

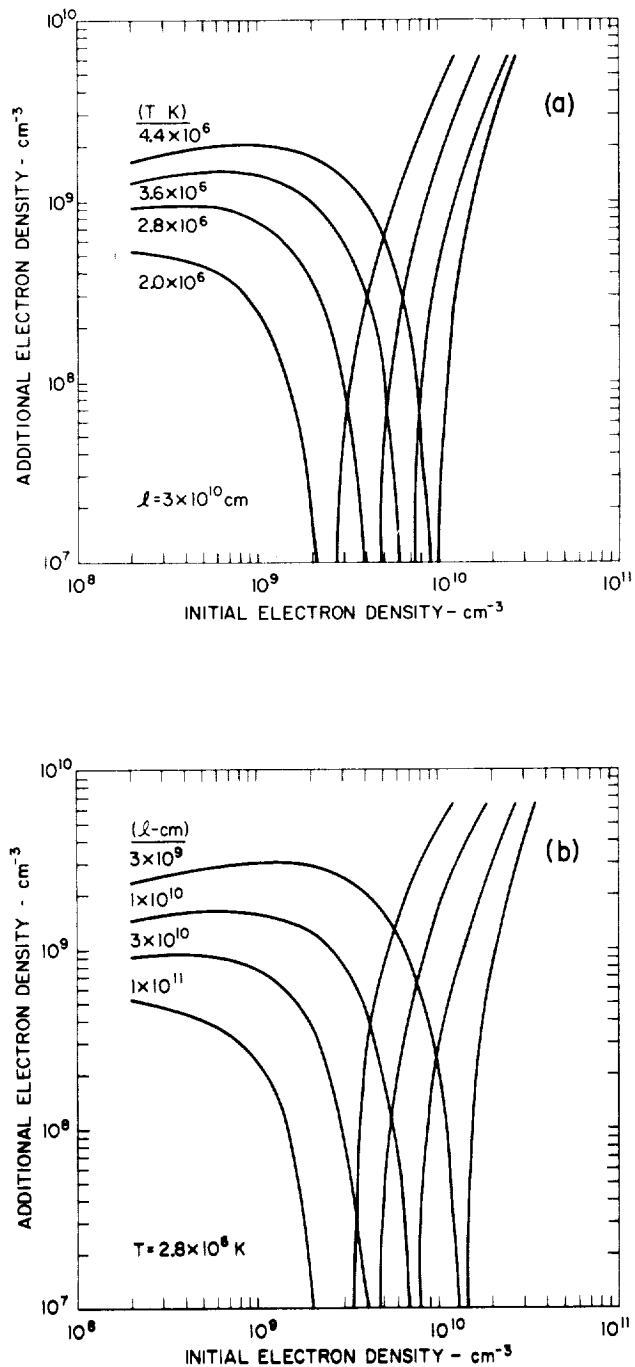


Fig. 4. The increase in density required to establish the radiative instability in a coronal arch as a function of the steady state density  $n_e$ , for (a) a constant length and various electron temperatures and (b) a constant electron temperature and various lengths.

By substituting the parameters for the standard arch (Table I), we find that  $\Delta n_e$  must exceed  $2.5 \times 10^8 \text{ cm}^{-3}$  if a new equilibrium is not to be established at some lower temperature which is above the temperature of the minimum of the power loss curve. For greater values of  $\Delta n_e$ , conduction will not be able to stabilize the temperature and cooling will continue until typical filament temperatures are reached.

Equation (7) has been evaluated to determine the dependence of  $\Delta n_e$  on the initial density for various values of the length  $l$  and initial temperature  $T$ . Inspection of the resulting curves (Figure 4) shows that: (1) For all arches there exist specific values of  $n_e$  and  $T$  for which the density perturbation required to initiate the radiative instability becomes very small. For constant  $l$  (Figure 4a) the value of the initial density for which this occurs is a positive function of temperature, while for constant  $T$  (Figure 4b) the critical value of the initial density is proportional to a negative power of the length. (2) For constant  $l$  and  $T$ , as the ambient density increases, corresponding to an increase in the loop heating supply, the density perturbation  $\Delta n_e$  required to drive the arch through the minimum in the loss curve remains fairly constant for ambient densities below  $1 \times 10^9 \text{ cm}^{-3}$  but falls off rapidly above this value.

From these results and the measured distribution of  $n_e$ ,  $l$ , and  $T$  among active filament arches the cooling mechanism can be expected to occur preferentially among the longer, cooler loops of the observed distribution. They require a smaller increase in density to establish the radiative instability which in turn places less stringent requirements on the transient supply.

## 2.2. THE RELEASE OF POTENTIAL ENERGY AS THE TRANSIENT ENERGY SUPPLY

Our model considers filaments to be supported in a Kippenhahn-Schlüter configuration which has been reached through the collapse of a coronal arch. If the collapse is the initial stage in this sequence, the release of potential energy during the collapse would appear as a transient energy source. For this particular mechanism to establish the radiative instability the energy released must be sufficient to increase the density of the whole arch to the required level and in the process to raise the temperature (i.e., the internal energy) of the material to coronal values.

To estimate the latter quantity the material is assumed to reach the temperature characteristic of the minimum of the power loss curve for the particular arch. This allows the energy required to be expressed in terms of  $n_e$  and  $l$  by using Equation (5) to eliminate temperature.

The integral energy equation has the form

$$\Delta PE_{\text{arch}} \geq \Delta PE_{\text{evap}} + \Delta IE_{\text{evap}} + Q_{(\text{rad} + \text{cond})}, \quad (8)$$

where  $\Delta PE_{\text{arch}}$  is the change in potential energy of the collapsed material,  $\Delta PE_{\text{evap}}$  and  $\Delta IE_{\text{evap}}$  are the increase in potential and internal energy of the evaporated material respectively, and  $Q_{(\text{rad} + \text{cond})}$  is the sum of the radiative and conductive losses of the evaporated material as it ascends into the arch. The second term dominates the RHS of the equality and in comparison the radiative and conductive loss term can be

neglected for evaporation times less than  $10^4$  s. In this limit their inclusion would change the result by less than 10%.

Based on the energy equation, the maximum increase in density provided by the collapse of an arch can be evaluated in terms of  $h$ , the height of the arch, and  $\Delta h$ , the distance fallen during the collapse. Thus,

$$n'_e = \frac{m_p n_e \bar{g}_h \Delta h}{1.5 m_p \bar{g}_h (h - \Delta h) + 6k(T_{\min} - T_b)} \tag{9}$$

and  $\bar{g}_h$  is the acceleration due to gravity averaged over height. By setting  $h = 5 \times 10^9$  cm and  $\Delta h = 3.5 \times 10^9$  cm, values which are typical of experimental observations, and evaluating the coefficients, Equation (9) can be reduced to

$$n'_e = n_e (5.0 \times 10^{-8} n_e^{4/7} l^{2/7} - 0.1)^{-1} \tag{10}$$

Equation (10) has been evaluated for arches of three sizes which cover the range of

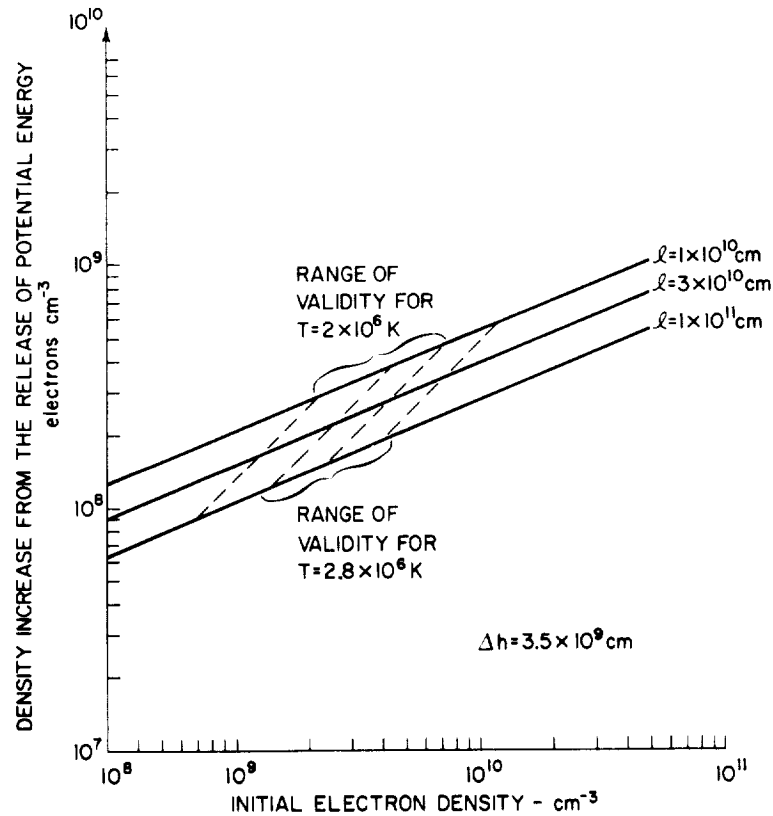


Fig. 5. The density increase to be expected from the release of potential energy in the collapse of arches of various lengths through a height of  $3.5 \times 10^9$  cm as a function of the initial arch density. The broken lines show the range in added density needed to initiate the radiative instability for various temperature arches. For arches whose parameters lie within these limits, the proposed model of filament formation is energetically feasible.

observed values and the results are shown in Figure 5. By comparing the result for the maximum density obtainable by this mechanism with the evaluation of Equation (7) (Figure 4) for the density increase necessary to initiate the radiative instability, one can specify the ranges of values of  $n_e$ ,  $l$ , and  $T$  for which the model is energetically feasible. Ranges for two coronal temperatures are superimposed on Figure 5, and it can be seen that the arches for which the model is successful are quite typical of coronal observations.

### 2.3. THE TIME SCALES OF FILAMENT FORMATION

Two times are relevant for comparing the model with observation. They are the time for establishing the radiative instability,  $\tau_1$ , which consists of the duration of the transient energy supply and its subsequent conversion into increased density within the arch, and the time,  $\tau_2$ , once this has happened for the arch to cool and condense into a filament.

A lower limit can be placed on  $\tau_1$  by considering the collapse occurs instantaneously throughout the arch, that the material then falls freely under gravity during which time the conversion of potential energy to internal energy occurs and that the energy conduction and the evaporated return are governed by the sound speed. The free-fall time through  $3.5 \times 10^9$  cm is approximately  $5 \times 10^2$  s. The sound speed,  $V_s = (kT/m_p)^{1/2}$ , for the plasma within the standard arch is  $1.3 \times 10^2$  km s<sup>-1</sup> and therefore the conduction-evaporation time will be approximately  $2.0 \times 10^3$  s. Thus, the minimum time required to establish the radiative instability will be on the order of  $2.5 \times 10^3$  s.

Once the transient source ceases, the new material which has entered the arch will cause the arch to cool. The cooling time  $\tau_2$  is defined as the time taken for the arch to cool from its ambient, precollapse, temperature  $T_1$  to the final temperature  $T_2$  reached by the filament.  $T_2$  has been chosen for the purpose of calculation as  $2 \times 10^4$  K. The cooling time can be estimated by evaluating the integral

$$\tau_2 = \int_{T_1}^{T_2} \frac{E_{\text{total}} dT}{P_r(T) + P_c(T) - Q_{ss}} \quad (11)$$

$Q_{ss}$  is the steady state energy supply which is assumed to be directly proportional to the total electron density and its magnitude has been evaluated by assuming that, in the pre-collapse condition, the heating supply is in equilibrium with the conductive and radiative losses.

Substituting for the various quantities the cooling time integral becomes

$$\tau_2 = \int_{T_1}^{T_2} \frac{3(n_e + n'_e)kl dt}{k_r(T)l(n_e + n'_e)^2 + 2k_c T^{5/2} - n_e^{-1}(n_e + n'_e) [k_r n_e^2 l T_1^{-1} + 2k_c T_1^{5/2}]} \quad (12)$$

Numerical evaluations using the temperature dependence of the radiative loss function proposed by Hildner (1974) for several values of  $n_e'/n_e$ ,  $l$ , and  $T_1$ , which are within the range of permissible values, are shown in Figure 6. The cooling times generally fall in the range of  $10^4$  to  $10^5$  s (3 to 30 hr) with the longer times being more realistic since they require smaller increases in density and are therefore energetically preferred.

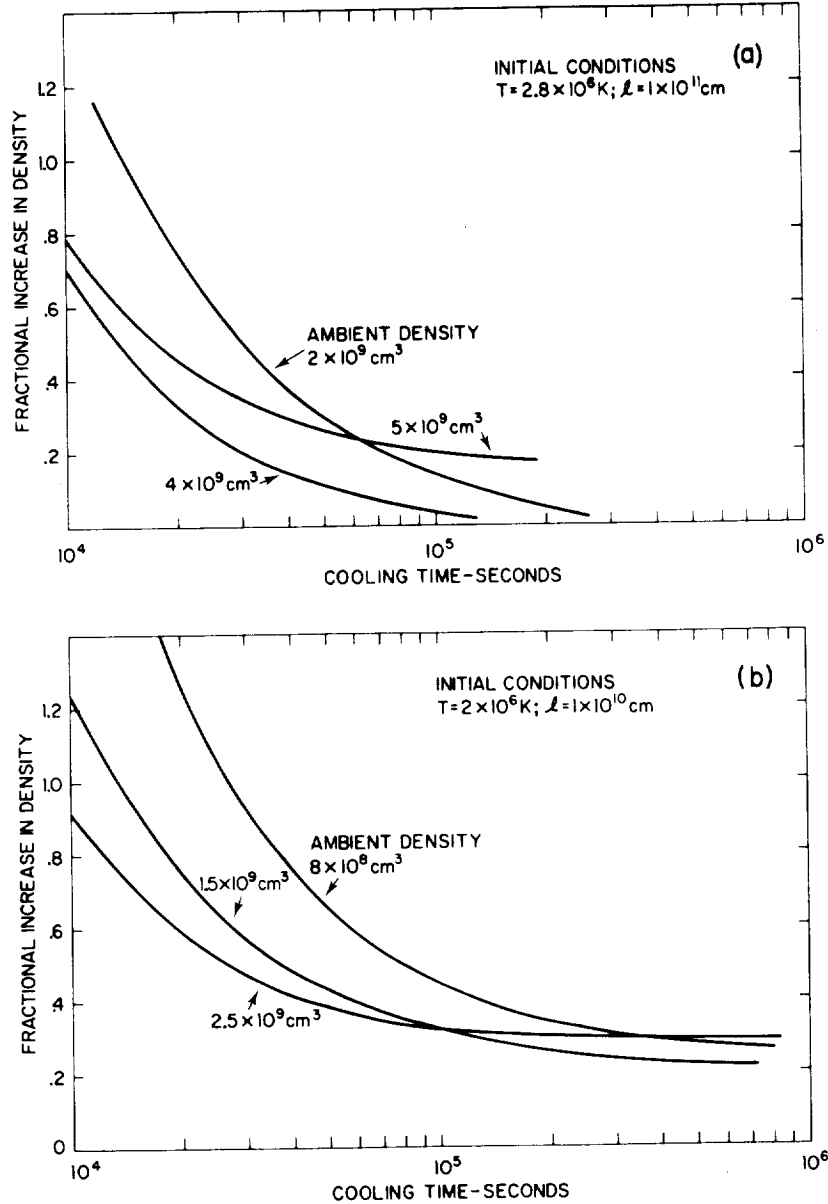


Fig. 6. The dependence of the cooling times of the proposed coronal condensations on the fractional increase in density produced by the transient energy supply. (a) For  $T = 2 \times 10^6 \text{ K}$  and  $l = 1 \times 10^{10} \text{ cm}$ . (b) For  $T = 2.8 \times 10^6 \text{ K}$  and  $l = 10^{11} \text{ cm}$ .

Inspection of the cooling curves shows that the condensations cool rather slowly above  $1 \times 10^6$  K and very rapidly below. For example the two typical condensations, shown in Figure 7, spend 98% of their time above one million degrees which, in the higher temperature case corresponds to 12 hr, compared to 14 min below. Although inclusion of dynamic effects may well alter these values, observations at the wavelengths associated with temperatures below  $1 \times 10^6$  K are unlikely to yield information about the formation of the condensation which occurs at much higher temperatures.

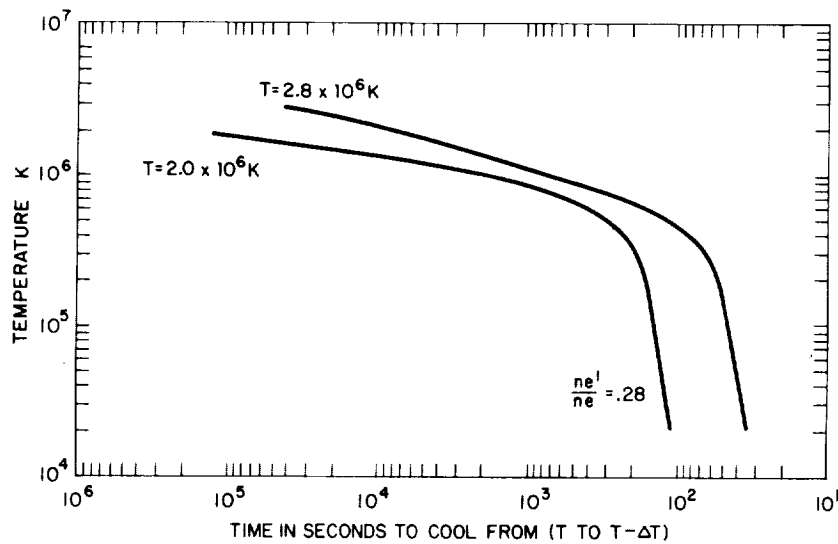


Fig. 7. Cooling curves for two coronal condensations starting from different temperatures. The curves show the length of time required to cool between two temperatures and demonstrate that the condensations cool slowly above  $1 \times 10^6$  K.

The length of time spent at the higher temperatures provides an explanation for the current failure to have observed filament appearances and associated changes in the structure of X-ray arches. Such a study was performed by one of the authors (JMD) using the S-054 Skylab data. It was restricted to single orbits ( $10^3$ – $4 \times 10^3$  s) since this was the period over which sequences of good time resolved images were available. If the present model is realistic correlations would be expected only over much longer periods. Ideally such a study requires observations from the intermediate temperatures, for otherwise the association of the filament appearance in  $H\alpha$  with a short lived X-ray event occurring 20–30 hr earlier may be unconvincing.

#### 2.4. THE MASS AND DENSITY OF THE FILAMENT

The model is based on the assumption that the condensation of a single arch will form an element of length of a filament. This assumption is derived from the experimental observations which show *arcades* of loops above filament channels, their absence over existing filaments and, for irregular filaments, the location of arches only above sections

of the filament where the H $\alpha$  absorption is weak or missing (Davis and Krieger, 1982). Since the arches within an arcade are separated by distances roughly equal to their diameters (Figure 1), the length of the element is assumed to be twice the diameter of the original arch.

It is also assumed that material from only half of the precollapse arch flows into the condensation, under the action of both gravity and the pressure differential generated by the falling temperature of the condensation. Therefore the mass of material that will condense into an element of the filament will be

$$M_c = m_p \rho_a \pi r_a^2 \frac{l_a}{2} + \Delta M, \quad (13)$$

where the subscript  $a$  refers to the parameters of the arch in its pre-collapse condition and  $\Delta M$  is the added mass required to initiate the radiative instability. On the basis of Figure 6,  $\Delta M$  is set equal to  $0.3M_c$ . If the filament has an elliptical cross-section with a ratio between major and minor axes of  $\frac{5}{3}$ , the mass of the filament will be given by

$$M_f = m_p \rho_f \frac{3\pi}{5} r_f^2 4r_a, \quad (14)$$

where  $4r_a$  is the length of the element of the filament formed by the condensation of the arch of radius  $r_a$ . Thus since  $M_f = 1.3M_c$ , if no mass is lost,

$$r_f = \left[ 0.271 r_a l_a \frac{\rho_a}{\rho_f} \right]^{1/2}. \quad (15)$$

Thus for density ratios ( $\rho_f/\rho_a$ ) in the range  $10^2$  to  $10^3$  corresponding to filament densities from  $10^{11}$  to  $10^{12}$  cm $^{-3}$  the thickness of the filament would vary from  $8 \times 10^3$  to  $3 \times 10^3$  km. Condensation of the five individual arches seen in Figure 1 would result in a filament with a mass of  $6 \times 10^{14}$  g. These values are in reasonable agreement with observation and indicate that sufficient material exists within coronal arches to form filaments.

Finally the remaining material in the arms of the arch may either fall back into the lower atmosphere or by a siphon action (Pikel'ner, 1971; Serio *et al.*, 1978) flow into the condensation. In either case the result will be a dense, cool condensation supported in a virtually empty flux tube. If the steady state heating mechanism continues to operate, the energy dissipated in the empty tube will continue to be available for evaporating material into the arch providing a continuous mass feed to the filament. This will compensate for the material that is frequently observed draining from the filament because of the imperfect nature of the supporting mechanism and may explain the long lifetimes of quiescent filaments.

### 3. Conclusions

A model has been proposed to condense filaments from coronal arches by invoking a transient energy source to establish the radiative instability. The model provides a

mechanism for cooling the arch through the minimum in the power loss curve ensuring that the arch will cool to the temperature associated with filaments. The energy required for this is not large and the parameters of coronal arches observed above filament channels are adequate to generate the requisite density. Time scales for cooling the condensation are quite long, ranging from  $10^4$  to  $10^5$  s with the majority of the time spent above  $1 \times 10^6$  K. Establishing a direct connection between the X-ray arch and the appearance of the filament will require observations over a broad spectral range.

Since the X-ray observations have demonstrated that arcades of loops occur above filament channels, the model assumes that the formation of a complete filament requires the condensation of the arcade. In this way sufficiently massive filaments can be obtained.

A logical extension of the basic concept suggests that the mechanism which originally maintained the X-ray arches may continue to operate thus providing a method for continually feeding material into the filament. Such a mechanism would explain the extended existence of quiescent filaments.

Although the model successfully describes the broader aspects of filament formation it is still in a very preliminary stage. In particular the identification of the transient energy source with the release of potential energy of the collapsing arch is open to question.

However the basic premise of the model that transient heating can lead to cooling is not affected by these questions and hopefully will provide a useful addition to the continued studies of filament formation.

#### Acknowledgements

It is a pleasure to acknowledge the many useful discussions held with our colleagues at AS & E since the inception of this project in 1973. The work has been supported by NASA under contracts NAS2-7424, NAS2-8683 and NAS5-25496.

#### References

- Cox, D. P. and Tucker, W. H.: 1969, *Astrophys. J.* **157**, 1157.  
 Davis, J. M. and Krieger, A. S.: 1982, *Solar Phys.* **80**, 295.  
 Hildner, E.: 1974, *Solar Phys.* **35**, 123.  
 Jordan, C.: 1976, *Phil. Trans. Roy. Soc.* **A281**, 391.  
 Kippenhahn, R. and Schlüter, A.: 1957, *Z. Astrophys.* **43**, 36.  
 Levine, R. H. and Withbroe, G. L.: 1977, *Solar Phys.* **51**, 83.  
 McWhirter, R. W. P., Thonemann, P. C., and Wilson, R.: 1975, *Astron. Astrophys.* **40**, 63.  
 Pikel'ner, S. B.: 1971, *Solar Phys.* **17**, 44.  
 Pye, J. P., Evans, K. D., Hutcheon, R. J., Gerassimenko, M., Davis, J. M., Krieger, A. S., and Vesecky, J. F.: 1978, *Astron. Astrophys.* **65**, 123.  
 Raadu, M. A. and Kuperus, M.: 1973, *Solar Phys.* **28**, 77.  
 Rosner, R., Tucker, W. H., and Vaiana, G. S.: 1978, *Astrophys. J.* **220**, 643.  
 Serio, S., Vaiana, G. S., Godoli, G., Motta, S., Pirronello, V., and Zappala, R. A.: 1978, *Solar Phys.* **59**, 65.  
 Tandberg-Hanssen, E.: 1974, *Solar Prominences*, D. Reidel Publ. Co., Dordrecht, Holland.

4.7 X-Ray and Microwave Observations of Active Regions

D.F. Webb and J.M. Davis

American Science and Engineering, Inc.  
Cambridge, Massachusetts 02139

and

M.R. Kundu and T. Velusamy

Astronomy Program  
University of Maryland  
College Park, Maryland 20742

ORIGINAL PAGE IS  
OF POOR QUALITY



# X-RAY AND MICROWAVE OBSERVATIONS OF ACTIVE REGIONS

D. F. WEBB and J. M. DAVIS

*American Science and Engineering, Inc., Cambridge, MA 02139, U.S.A.*

and

M. R. KUNDU and T. VELUSAMY\*

*Astronomy Program, University of Maryland, College Park, MD 20742, U.S.A.*

(Received 30 March; in revised form 15 October, 1982)

**Abstract.** We compare coordinated, high spatial resolution (2–3 arc sec) observations at 6 cm and in soft X-rays with photospheric magnetograms and optical filtergrams of two active regions. The correspondence of the brightest centimetric components in these regions with coronal loops, sunspots and pores, chromospheric structures and the photospheric magnetic field was determined. Our principal results are: The association between the microwave components and coronal X-ray and photospheric magnetic field structures is complex; in general X-ray emission was not associated with the microwave components. A majority of the components were *not* associated with sunspots, although the brightest ( $T_b \geq 4 \times 10^6$  K) components overlay regions of strong photospheric field or high field gradients. Several of the components coincided with the apparent bases of shorter coronal loops and 4 with the tops of X-ray loops.

The X-ray and magnetic field observations are used to constrain possible centimetric emission mechanisms. Thermal bremsstrahlung can not be a significant contributor to this bright microwave emission. Thermal gyro-resonance absorption is consistent with some of the observations, but untenable for those components which are bright in microwaves, lack X-ray emission, and overlie regions of weak magnetic field. As an explanation for the brightest ( $T_b \geq 4 \times 10^6$  K) components, the g-r theory requires coronal loops with significant currents but very low densities. Alternatively, a nonthermal mechanism implies that the emission arises from the transition region and suggests that discrete regions of continuous particle acceleration may be common in active regions.

## 1. Introduction

Much recent work in solar physics has focussed on the problem of the structure of active regions (ARs) in the transition region and low corona. This study has been paced by observations from rockets and satellites, which can observe X-ray and EUV emission with high spatial and spectral resolution, and with large ground-based arrays at centimeter radio wavelengths. The high spatial resolution (a few arc sec) of the instruments has substantially altered our view of the transition region and corona, and prompted the development of more realistic models of active regions.

The slowly varying component of the radio emission over ARs has a spectral maximum at centimeter wavelengths. Only recently has this emission been examined with sensitivity and spatial resolution approaching that of other wavelengths. Observations have shown that the brightest centimetric components are associated with structures near sunspots, transverse fields over neutral lines or filaments (Kundu, 1977,

\* Presently at the Tata Institute of Fundamental Research, Bombay, India.

1980, 1981), and emerging flux regions (Kundu and Velusamy, 1980). The fact that these latter features are also associated with X-ray loops and that thermal bremsstrahlung can produce emission at both microwave and X-ray wavelengths leads us to suspect that at least part of the microwave emission in active regions arises in coronal loops. Recent high resolution centimeter observations with the Very Large Array (VLA) have revealed loop-like structures reminiscent of those observed in X-rays and EUV (Kundu and Velusamy, 1980). Previous comparisons of imaging observations in soft X-rays and microwaves have shown that most of the general plage-related emission in ARs is due to thermal bremsstrahlung (Gerassimenko *et al.*, 1976; Pallavicini *et al.*, 1979). The brighter centimetric components require an explanation in terms of low harmonic gyromagnetic emission (e.g., Kundu *et al.*, 1980; Alissandrakis *et al.*, 1980; Felli *et al.*, 1981).

This paper presents the initial results of a long term study whose purpose is to measure the plasma parameters and the properties of the magnetic field in coronal structures through the use of combined high spatial resolution X-ray, magnetogram and microwave data. Although this first paper is primarily observational, the results are sufficient to constrain possible centimetric emission mechanisms. In particular we conjecture that the results imply a significant small-scale, nonthermal component to the slowly varying radiation from ARs.

We describe the analysis of two active regions observed on 16 November 1979. The data include soft X-ray filtergrams from a sounding rocket flight, microwave radio maps of total intensity and circular polarization obtained with the VLA, photospheric magnetograms and optical filtergrams, all of comparable high spatial resolution (1–3 arc sec). This is the first time that such coordinated, high spatial resolution observations in microwaves and X-rays of active regions have been available. In the next section we describe the observational data. In Section 3 we discuss the observational results. The key results are summarized in Section 4 and discussed in the last section.

## 2. The Observations and Data Analysis

### 2.1. SOFT X-RAY DATA

On 16 November 1979 American Science and Engineering (AS&E) launched the second of two rocket flights designed to obtain a complete view of the solar corona at solar maximum. This payload utilized a metallic mirror previously flown many times (Vaiana *et al.*, 1973). Full-disk images of the corona with an on-axis spatial resolution of 2–3 arc sec were obtained between 17:02 and 17:05 UT. The images were recorded with two Kodak emulsions, SO-212, a moderate-speed emulsion, and SO-253, a fine-grain holographic emulsion which permits improved definition of coronal features (Davis *et al.*, 1979).

### 2.2. MICROWAVE DATA

The radio observations were made at 6 cm with the VLA of the National Radio Astronomy Observatory between 15:00 and 16:45 UT on 16 November 1979. Seven-

teen antennas were available during the observations, providing good determination of the two-dimensional brightness distribution. The system was sensitive to structures smaller than 3 arc min because the shortest spacing used for these maps was  $1200 \lambda$ . The observing procedure and calibration and cleaning methods were similar to those discussed by Kundu and Velusamy (1980). The observations alternated between two active regions, Hale Nos. 16419 and 16421. The centers of the regions used for continuous tracking were located at N10 W23 and N32 W33 in heliographic coordinates at 00 UT. Synthesized maps of total intensity and circular polarization were obtained of a field of view of  $6.4 \times 6.4$  arc min around each active region. The synthesized beam was  $3 \times 6$  arc sec with the long axis oriented in the north-south direction. The dynamic range on these maps was greater than a factor of 10.

### 2.3. CHROMOSPHERIC AND PHOTOSPHERIC DATA

Full-disk photospheric magnetograms were obtained at Kitt Peak National Observatory (KPNO). The magnetograms used for our study were obtained at 15:43, 17:43, 18:28, 19:17, 20:07, and 21:00 UT. In addition, a full disk He I - 10830 Å filtergram was obtained at KPNO at 16:47 UT. The magnetograms at 15:43 and 17:43 UT bracketed the times of the X-ray and radio observations and therefore were used in our detailed analysis. No significant changes in the general magnetic field in either of the two ARs was observed on the magnetograms. In addition, video magnetograph (VMG) images were obtained from Big Bear Solar Observatory (BBSO) and used to verify the KPNO data.

Chromospheric data were obtained in collaboration with BBSO. Nearly continuous H $\alpha$  observations with time resolution of 10 s of both active regions were obtained on 16 November from 15:55 to 22:00 UT. Most of these images were centered on H419; only 5 min of high resolution data were taken of H421 starting at 21:54 UT. A cine version of these data was used to select individual frames for enlargement and to study the evolution of chromospheric and photospheric structures in H419. Frames enlarged for the detailed study were recorded at 16:58, 19:35, and 19:37 UT in H $\alpha$ , H $\alpha$  wings and continuum, respectively, and in H $\alpha$  at 21:57 UT for H421. Full-disk patrol H $\alpha$  data obtained at 19:37 UT (H $\alpha$ ) and 21:40 UT (near-H $\alpha$  continuum) were used in the alignment scheme.

### 2.4. METHOD OF COMPARISON

A selection of the X-ray and visible light images, the microwave maps, and the optical images were converted to transparencies with a scale of  $4.8 \text{ arc sec mm}^{-1}$  (40.6 cm solar disk diameter). To compare the locations of the X-ray and microwave features, the heliographic positions of the centroids of the sunspots that lay within the field of the radio maps were determined, using a Mt. Wilson sunspot chart and an H $\alpha$  image from NOAA-Boulder. These positions were converted to celestial coordinates at 17:00 UT and plotted on the radio maps. Visible light images from the AS&E experiment revealed sunspots which were used as an intermediary to coalign the X-ray, radio and optical data. The magnetograms were coaligned by using the fact that H $\alpha$  plage emission tends

to occur in areas of strong vertical magnetic fields. Up to 6 spot groups were used for alignment. The alignment accuracy between the X-ray data and the radio maps was about 5 arc sec. The overall accuracy including the optical data was 5–10 arc sec.

### 3. Observational Results

Figure 1 presents the 6 cm maps in total intensity (left) and circular polarization (right) of active region H421 (top) and H419 (bottom), observed on 16 November, 15:00–16:45 UT. The crosses denote the centers of the large sunspots lying within the area of the radio maps. To illustrate the relation of the microwave emission to hot ( $T_e > 10^6$  K) coronal loops and to the photospheric magnetic field, we show the radio intensity contours of AR H421 (Figure 2) and AR H419 (Figure 3) superimposed on a soft X-ray image (top) and on a photospheric magnetogram (bottom).

Table I lists the brightest microwave components in each region in approximately decreasing order of brightness temperature ( $T_b$ ). For each source its estimated size, dominant polarity and degree of polarization ( $V/I$ ), and possible physical association are also listed. For each active region the source components are indicated on the intensity maps in Figure 1. It should be emphasized that we studied only the *brightest* microwave components in these regions. The VLA configuration used was not sensitive to large structures or low brightness sources (e.g., plages), but was optimal for observation of the compact, bright coronal structures typical of ARs. The noise level of the maps was about  $T_b = 4 \times 10^5$  K. We concluded that the X-ray and microwave sources in these two regions were quiescent, i.e. that no obvious flares or bursts occurred there during the period of observation. The limitations of this statement are discussed in the final section.

#### 3.1. ACTIVE REGION H421

Active region H421 was closer to disk center than H419 ( $r \sim 0.75$  from Sun center) on 16 November and therefore suffered less from projection effects and off-axis vignetting and scattering in X-rays. It was apparently evolving rapidly, because BBSO observations on 18 November showed a dramatic change in the region with considerable emerging flux in the area to the northwest of the main spot. Region H421 contained one dominant sunspot with penumbra of negative polarity and many small spots or pores. The large spot had an area of 50 millionths of a solar hemisphere and a field strength  $\leq 2000$  G (*Solar Geophysical Data*, 1980).

The bright coronal X-ray structure of AR H421 consisted of two loop arcades crossing the N–S magnetic inversion lines of the region. The arcades were potential-like, with their loops oriented orthogonally to the inversion line. The salient X-ray feature was a short, bright loop (arrow, Figure 2a) which bridged the inversion line in an area of high field gradient near the spot. The western foot of the loop ended at the edge of the spot penumbra. The length ( $\sim 2 \times 10^4$  km), shape and location of this loop are typical of a class of X-ray loops called penumbral loops (Webb and Zirin, 1981). The inversion line swung in toward the spot and was marked by a short  $H\alpha$  filament; the

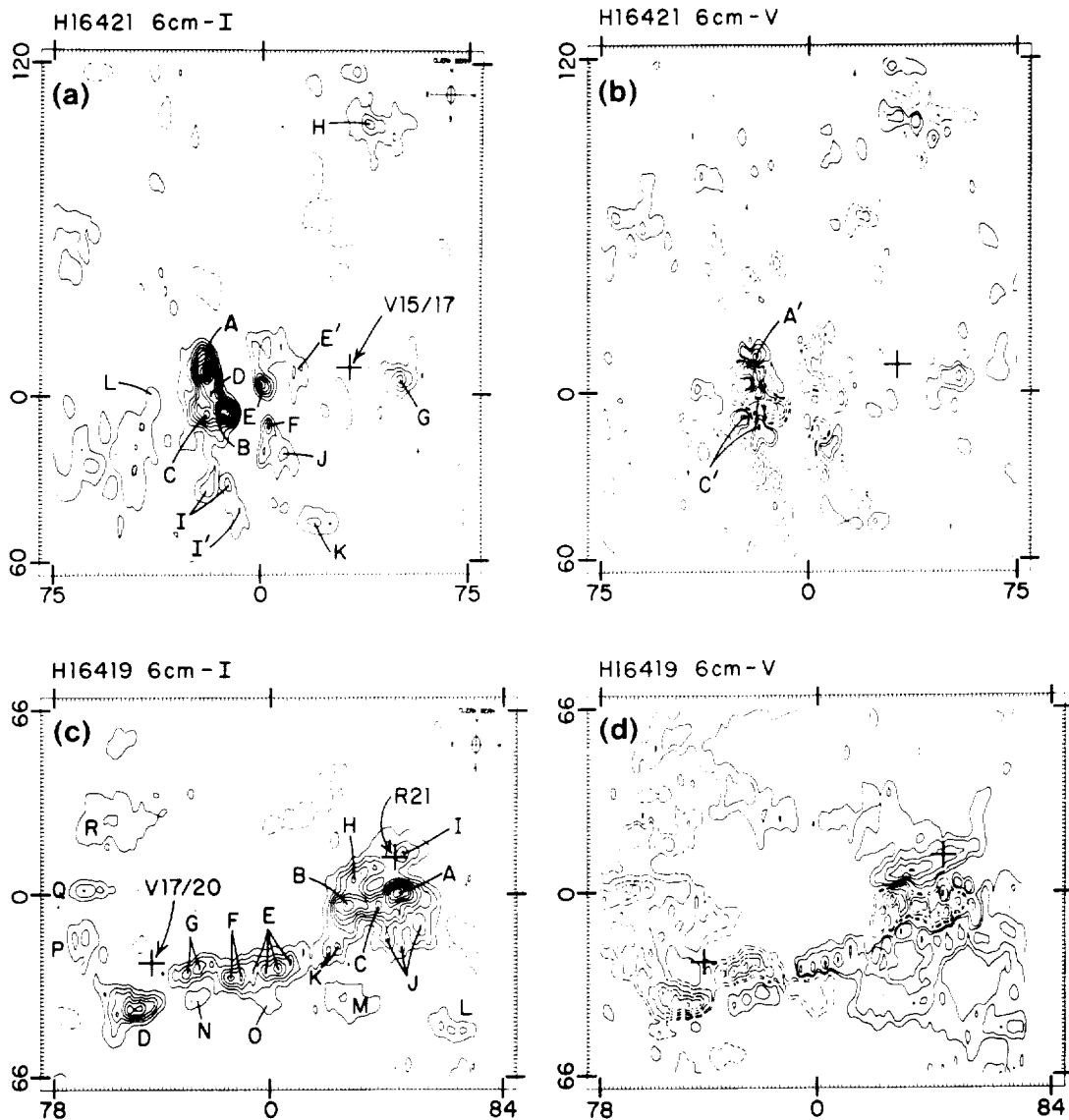


Fig. 1. 6 cm VLA maps of active regions H 16421 (top) and H 16419 (bottom) on 16 November 1979. The size of the synthesized beam was  $6 \times 3$  arc sec. Geocentric north is at the top and east to the left. The center (0, 0) of the H 16421 map was at 263 arc sec north and 316 arc sec west of disk center at 16:00 UT, and the center (0, 0) of the H 16419 map was at 660 arc sec north and 342 arc sec west of disk center. (a) Total intensity (R + L) map of H 16421. The lowest contour and the contour interval is  $8 \times 10^5$  K. The cross shows the centroid of the large sunspot V15/17 in Mt. Wilson group No. 21042; the length of the arms of the cross is 10 arc sec, which is representative of the alignment uncertainties. The letters designate individual microwave components. (b) Circularly polarized (R - L) intensity map of H 16421. The first two contours are 4 and  $8 \times 10^5$  K, respectively, and the contour interval for the higher contours is  $8 \times 10^5$  K. The solid (broken) contours represent positive (negative) values. (c) Total intensity map of H 16419. The contour levels are the same as (a). The crosses show the centroids of sunspots V17/20 and R21 in the Mt. Wilson group No. 21041. (d) Circularly polarized intensity map of H 16419. The contour levels are the same as (b).

TABLE 1  
List of the brightest microwave components in the ARs H 16421 and H 16419

Source	Peak $T_b$ ( $10^6$ K)	Size <sup>a</sup> (arc sec)	Polarity <sup>b</sup>	Reversed? <sup>c</sup>	Polarization (%) <sup>d</sup>	Association
421 A	10.5	7 × 9	L	R	23	Photospheric pores – emerging flux loops
421 B	8	7 × 5	L	R	~30	Foot of bright loop?
421 C	6.5	6 × 6	L	R	30	?
421 D	6.5	<2	L	R	62	?
421 E	4.8	4 × 5	L	?	33	Foot of bright loop?
421 E'	1.5	4 × 5	L	S	–	Top of bright loop
421 F	3.2	3 × 11	L	R	25	Foot of bright loop or of arcade loop
412 G	3.2	5 × 5	R	?	25	Penumbra or neutral line
421 H	2.5	8 × 6	R	S?	33	Top of coronal arcade
421 I	1.5	3 × 9	L	R?	100	Foot of filament arcade loop
421 I'	1.5	3 × 12	L	–	–	Top of filament arcade loop
421 J	1.5	3 × 4	R	?	50	Foot of arcade loops
421 K	1.5	3 × 5	R?	R?	–	Foot of filament arcade loop
421 L	~1	diffuse	R	R	–	Small loop over magnetic cell
419 A	7.2	7 × 5	L	R	22	Photospheric pore and/or penumbra
419 B	6.5	11 × 6	L	R	50	Photospheric pore and/or penumbra
419 C	4.8	2 × 3	L	R	40	Photospheric pore and/or penumbra
419 D	4.8	12 × 6	L	S	83	Penumbral loops
419 E	1.5–4.8	15 × 7	R	S and R	40–100	Neutral line with high field gradients
419 F	4	7 × 4	L?	S?	?	Top of loop?
419 G	4	12 × 5	L	S	80	Penumbral loops
419 H	4	6 × 4	R	S	60–80	Photospheric pore and/or penumbra
419 I	3.2	4 × 5	R	S?	50	Sunspot umbra
419 J	1.5–2.5	15 × 8	R	S	33–100	Loop arcade crossing NL
419 K	2.5	5 × 3	R	S	33	?
419 L	1.5	10 × 3	R	?	50	?
419 M	1.5	12 × 6	R	?	50	Top of long X-ray loop
419 N	1.5	6 × 3	R	S or R	–	Magnetic cell or foot of penumbral loops
419 O	~1	diffuse	L	?	–	Foot of loops
419 P	1.5	6 × 5	L	?	100	Foot of X-ray loop?
419 Q	2.5	9 × 5	L	R?	100	Foot of X-ray loop?
419 R	1.5	diffuse	L	?	?	Foot of filament arcade loop?

<sup>a</sup> The approximate FWHM dimensions of the total intensity along the short and long axis of each component. These have not been corrected for the beam shape.

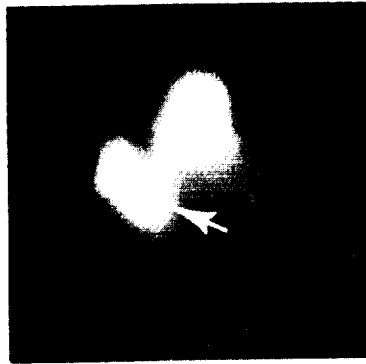
<sup>b</sup> The sense of circular polarization at the peak intensity of the component. L is left CP (negative) and R is right CP (positive).

<sup>c</sup> Whether the sense of circular polarization (b) is the same (S) or reversed (R) with respect to the underlying photospheric magnetic field. This assignment does not account for projection effects.

<sup>d</sup> Degree of polarization  $\% (V/I)$  at the peak intensity of the component.

ORIGINAL PAGE  
BLACK AND WHITE PHOTOGRAPH

H 421



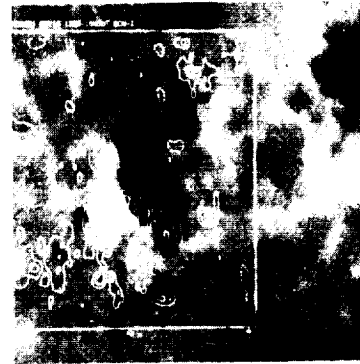
a) X-RAY: 1704 UT



b) X-RAY + 6 CM



c) MAG: 1742 UT



d) MAG + 6 CM

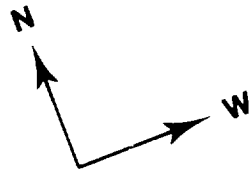
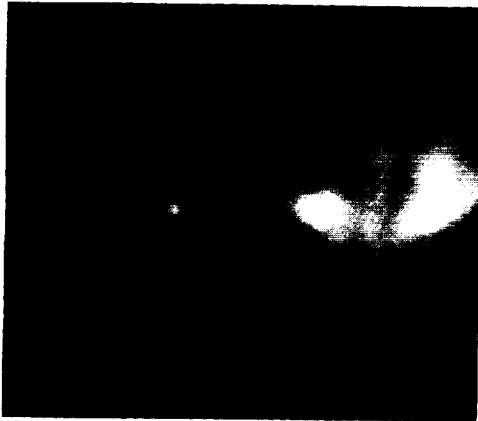
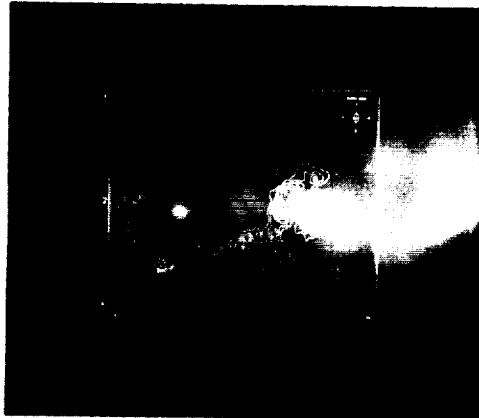


Fig. 2. Coaligned, high resolution images in soft X-rays (top), of the photospheric magnetic field (bottom) and at 6 cm of active region H 16421 on 16 November 1979. The X-ray image is a 60 s exposure on Kodak SO-253 emulsion. The 6 cm total intensity map from Figure 1a is superimposed on the X-ray and magnetogram images (b and d, respectively), which are shown separately on the left side for clarity. The direction arrows at the bottom denote heliographic directions.

# H 419



a) X-RAY: 1704 UT



b) X-RAY + 6 CM



c) MAG: 1742 UT



d) MAG + 6 CM

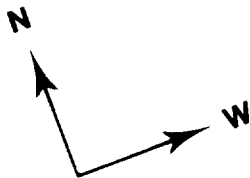


Fig. 3. Coaligned images similar to Figure 2 for active region H 16419 on 16 November 1979.

ORIGINAL PAGE  
BLACK AND WHITE PHOTOGRAPH

bright loop appeared to cross over this structure at a small angle, indicative of a high degree of shear in the coronal magnetic field. The bright loop and the eastern arcade crossed the area of the highest field gradients in the region.

In order to determine parameters of the coronal magnetic field, it is important to identify components of the bright X-ray loop in the microwave map (e.g., Kundu *et al.*, 1980). Unfortunately, the 6 cm components in this region were tightly clustered precluding an unambiguous identification. The component 421E appeared to be coincident with the eastern foot of the loop, and the weak component  $E'$  to the west with the top of the loop. But component  $E$ , left circularly polarized (LCP), also appeared to straddle the photospheric inversion line. If  $E$  was at the loop footpoint, then it lay east of the inversion line but was of reversed polarity to the photospheric field. Alternatively  $E$  might have marked the location of a neutral sheet or arcades crossing the inversion line.

The brightest microwave components in AR H 421 were  $< 2$  to  $7$  arc sec in diameter. Components  $A$ ,  $B$ ,  $C$ , and  $D$  lay south of the eastern X-ray arcade and well east of the inversion line (Figure 2). The photospheric field, especially underlying  $A$ , was strong and of positive polarity. Although the central polarization of this group was LCP, it was surrounded by islands of RCP indicating the bipolar nature of the group (Figure 1b). The component  $A$ , which had the brightest peak ( $T_b = 10.5 \times 10^6$  K) observed in either active region, was of LCP, weakly polarized ( $\sim 20\%$ ) and was coincident with an H $\alpha$  patch which later brightened and with several pores. Just north of  $A$  was a region of strong RCP ( $A'$ ). This suggests that  $A$  and  $A'$  were at the feet of an arcade of short loops. The proximity of the pores and the H $\alpha$  brightening suggests that strong emission around  $A$  might have been associated with neutral sheets in the corona over emerging flux (Kundu and Velusamy, 1980). The optical coverage was not adequate to definitely identify such emerging flux.

There were no obvious features underlying components  $B$  and  $C$  in the southern part of this group.  $C$  was flanked by two compact sources of RCP ( $C'$  in Figure 1b) suggesting bipolarity. All of the brightest sources in H 421 had lower circular polarization (20–30%) except for  $D$  which was highly polarized ( $\geq 60\%$ ).

An inclusion of negative photospheric polarity east of the neutral line (arrow, Figure 2c) was adjacent to an area of H $\alpha$  brightening and faint X-ray and microwave emission, but the alignment accuracy precluded a definite association.

The components  $I$ ,  $J$ , and  $K$  straddled a large, quiescent filament which ran generally E–W and bounded the active region to the south. Since large coronal arcades are known to overlie filaments and filament channels (McIntosh *et al.*, 1976; Webb and Zirin, 1981), the radio sources  $I$  and  $K$  probably were emission from the legs or feet of loops crossing the filament. Component  $I'$ , the southern extension of  $I$ , overlaid the filament; its emission probably came from the top of an arcade loop. The opposite polarization of the components  $J$  and  $F$  indicates that they outlined compact loop structures crossing a second inversion line north of the filament. The proximity of these two inversion lines suggests that this area was magnetically complex with high field gradients.

North of the sunspot was a classic arcade structure with X-ray loops joining opposite

polarity plage divided by a faint filament. The brightest X-ray structure was a large, diffuse arch defining the northern limit of the arcade. Superimposed near the top of this arch was component *H*, a bipolar source with peak  $T_b \sim 2.5 \times 10^6$  K. The component was of predominantly RCP.

Finally, the component *G* was compact, bright and entirely of RCP. It was  $\sim 25$  arc sec west of the center of the spot in an area of mixed photospheric polarity. It could have been associated with the penumbral field, especially since there were no bright X-ray or  $H\alpha$  structures in the vicinity.

### 3.2. ACTIVE REGION H 419

Region H 419 was 2–3 rotations old and appeared stable. However, it was magnetically more complex than region H 421 with a dominant preceding spot with a large penumbra and some pores, and two trailing spots. The large *p* spot, numbered R21 by Mt. Wilson, had an area of 270 millionths and a field strength of  $\sim 2500$  G. The smaller central negative spot, V17/20, and the trailing positive spot, R20, were of nearly equal size. Two of the sunspots (R21 and V17/20) lay within the field of the radio map (Figures 1 and 3). The large leading spot had many, bright microwave components clustered nearby.

The AR was characterized by diffuse X-ray emission spreading linearly in an E–W band. The most notable X-ray feature was a bright, compact structure, which was *not* associated with 6 cm emission, on the perimeter of the central spot penumbra. Several bright loops to the west were just outside of the field of view of the radio observations. Within this field of view the coronal emission generally bridged inversion lines.

We first discuss the microwave components surrounding the leader sunspot. Figure 4a shows details of the spot structure as seen in the continuum at 19:35 UT. A small spot lay within the southeast border of the penumbra, and several pores lay just outside the penumbra. The BBSO film revealed no appreciable changes in the leader sunspot and the pores around it between about 16:00 UT, when the radio and X-ray data were obtained, and 19:35 UT.

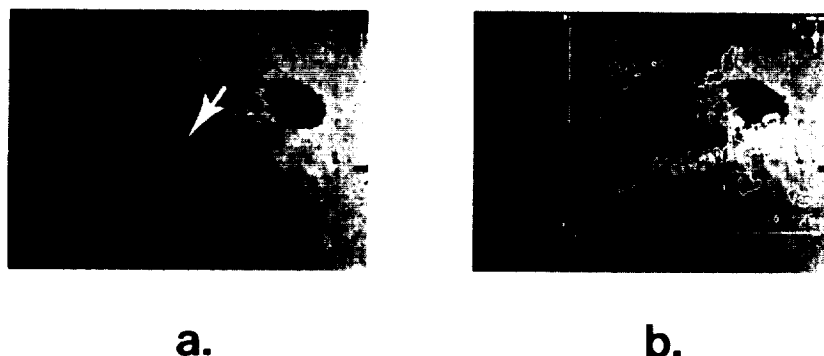


Fig. 4. (a) Near- $H\alpha$  continuum image of AR H 16419 at 19:35 UT on 16 November 1979 showing the sunspot structure. The arrow points to a pore that appeared after 17:00 UT. (b) The same image with the 6 cm total intensity map of Figure 1c superimposed on it.

Figure 4b shows the microwave components superimposed over the same continuum image. This comparison illustrates the following points: (1) The brightest components (*A*, *B*, *C*, and *H* with  $T_b = 4 - 7.2 \times 10^6$  K) were clustered in the vicinity of the penumbral spot and pores about 20–25 arc sec south of the umbral center; the spots and pores were all of the same polarity; (2) The strongest components (*A*, *B*, and *C*) were all LCP or of reversed polarity to the photosphere; (3) The small penumbral spot was associated with a region of low  $T_b$ , i.e., a 'hole' surrounded by bright emission. The components *A*, *B*, and *C* were in areas devoid of significant H $\alpha$  or X-ray emission. Their higher  $T_b$ , lower polarization (20–50%), and association with the high field strengths and gradients of the penumbra and pores suggest that this emission was due to a gyromagnetic mechanism.

About 30 arc sec south of the sunspot umbra was a bright V-shaped area of X-ray emission associated with H $\alpha$  fibrils. The multiple, elongated radio components *J* overlay this area. The N–S orientation of this microwave pattern, the X-ray structure, and the H $\alpha$  fibrils suggest that the emission arose from an arcade of low-lying loops crossing the inversion line.

The central sunspot in AR H419 (Figure 4a) like the spot in AR H421, had a well developed penumbra with no X-ray or microwave emission above it. The nearest radio components were *D* and *G*, 15–20 arc sec away, at the perimeter of the penumbra.

The area surrounding this spot was the scene of significant activity in the visible in the H $\alpha$  film. The brightest X-ray feature coincided with a negative magnetic spot in a moat of positive flux at the northern edge of the penumbra (top arrow; Figure 3c). Of flare-like brightness in H $\alpha$  from 16:50 to 17:20 UT, this area was active all day and reminiscent of the hot transient penumbral spots studied by Webb and Zirin (1981). This spot was not bright in microwaves, a point we will discuss later. A pore (arrow; Figure 4a) adjacent to the location of the magnetic knot emerged after our observing period.

The small positive polarity arc visible south of the sunspot (bottom arrow; Figure 3c) represents an inclusion of opposite polarity in the general field of the spot. It coincided with dark H $\alpha$  fibrils emanating from the edge of the spot and was located between the microwave components *D* and *N*. The arc was more likely associated with *N* because this component was RCP, of the same polarity as the magnetic arc, and projection effects would have shifted it to the northwest.

The component *D* was a bright ( $T_b \sim 5 \times 10^6$  K), compact source which lay just south of the sunspot penumbra. It was highly polarized (83%) in LCP, the same sense as the nearby spot polarity. Component *G* was a double source which overlay the penumbra. Both components *D* and *G* were likely associated with penumbral loops.

The chain of components labelled *E* in Figure 1c overlay an area of negative polarity to the east and positive polarity to the west, an area of high field gradients. The component *F* was bright and overlay a patch of H $\alpha$  emission, but was weakly polarized or unpolarized. This suggests emission from the top of a loop.

Three fainter components, *M*, *P*, and *Q*, appeared to be associated with X-ray loops. The large component *M* coincided with the top of a long, narrow X-ray loop, in a manner

similar to that of component *H* in AR H421. The X-ray loop may have been evolving since its feet were brighter than its midsection (Figure 3a); most quiescent X-ray loops are isobaric.

#### 4. Summary

The key results of our comparative study for 16 November 1979 are:

(1) The association between the microwave components and coronal X-ray structures is complex. In general X-ray emitting structures were *not* associated with the microwave components. This result is supported by Schmahl *et al.* (1982).

(2) The association between the microwave components and photospheric magnetic fields is likewise complex. Although about half of the radio components were associated with strong photospheric fields, such strong fields did not always produce centimetric emission. The *brightest* microwave components were associated with areas of strong longitudinal magnetic fields or high field gradients, but *not* with sunspot umbrae.

(3) About one-third of the sources appeared to be associated with only the feet or legs of coronal loops of size  $\leq 5 \times 10^4$  km. However, only some of these loops were observed in X-rays. The existence of others was deduced from the geometry of the surrounding magnetic field.

(4) There were five cases of possible microwave emission from the tops of coronal loops (Table II). Four of these loops, or loop arcades were identified by their emission in X-rays. These components were fainter ( $T_b \leq 2.5 \times 10^6$  K) and more diffuse than the other components, but had one dominant polarization.

TABLE II  
Sources at tops of coronal loops

Source	Peak $T_b$ ( $10^6$ K)	Peak polarity	X-radiation	Association
421 <i>E'</i>	1.5	L	yes	Bright penumbral loop
421 <i>H</i>	2.5	R	yes	Bright loop arcade over neutral line
419 <i>J</i>	1.5–2.5	R	yes	Loop arcade over neutral line
419 <i>M</i>	1.5	R	yes	Long single loop
421 <i>I'</i>	1.5	L	no	Possible filament arcade loop

(5) None of the sunspot umbrae studied had overlying X-ray emission; i.e., there is little if any material at coronal temperatures over spots. This agrees with previous coronal observations (Pallavicini *et al.*, 1979; Webb and Zirin, 1981; Webb, 1981; Nicolas *et al.*, 1981). Two of the 3 sunspot umbrae and the largest pore for which we had radio observations had no significant microwave emission over them. This result is also supported by other recent measurements at high spatial resolution (Kundu and Velusamy, 1980; Kundu *et al.*, 1981; Pallavicini *et al.*, 1981). The one sunspot with associated microwave emission (component 419I) was also the largest in both area and

magnetic field strength. This observation is consistent with the recent model of Pallavicini *et al.* (1981), which shows that thermal g-r emission may arise only over umbrae of sufficiently large size.

(6) Finally, the sense of 6 cm circular polarization was often reversed with respect to the underlying photospheric field, especially for the bright components. Also, in nearly every case where we interpreted the centimetric components as denoting the legs or feet of loops, one or both components had reversed polarization. We believe that these reversals are related to mode coupling in a quasi-transverse region (Kundu *et al.*, 1977; Bandeira, 1982).

### 5. Discussion

A major result of this study is that a *majority* of the individual bright microwave components we identified were *not* associated with sunspots. This result is contrary to the low resolution radio observations, i.e., that the centimetric core emission from ARs is *only* associated with spot umbrae. To quantify our assertion we drew circles with diameters equal to the largest measured diameters of the penumbra and centered on the umbra of each of the 3 spots we observed. In addition we drew concentric circles 10 arc sec in diameter larger to allow for alignment uncertainties. Sources which lay within or touched these circles were defined to be 'associated' with the sunspot. Thirty-two components for both ARs are listed in Table I. Of these only seven lay within the three inner circles and a total of 13 lay within the three outer circles. Therefore, 19, or 59% of the components were definitely *not* associated with sunspots using our criteria. This number is conservative because we did not correct for penumbral foreshortening and we grouped similarly structured sources together (e.g., 419E).

The existence of such a large number of strong components, not all associated with regions of strong photospheric magnetic field, and with a low correlation with X-ray structures means that mechanisms invoked to explain the radio sources must apply over a large range of magnetic field strengths and outside of the range of plasma parameters typical of ARs.

We can use the X-ray observations to constrain these emission mechanisms. First, although low brightness temperatures suggestive of thermal bremsstrahlung may be typical of the extended, plage-associated component of active regions (Kundu *et al.*, 1977; Pallavicini *et al.*, 1981; Felli *et al.*, 1981), we can rule out bremsstrahlung as a significant contributor to the bright radio emission studied here. Most of the material in a typical active region is at coronal temperatures ( $T_e > 10^6$  K), and is visible in broadband X-rays (see Webb, 1981 for a review). Therefore, since the corona is optically thin to bremsstrahlung in both broadband X-rays and at 6 cm, we can estimate the contribution of bremsstrahlung to the observed brightness temperature,  $T_b$ , of those centimetric components associated with X-ray structures. The 4 components associated with the X-ray loops (Table II) have brightness temperatures consistent with their being optically thin to bremsstrahlung (quiescent X-ray loops invariably have

$T_e = 2-3 \times 10^6$  K). In the optically thin case the predicted  $T_b$  is

$$T_b = \frac{\xi}{\nu^2 T_e^{1/2}} \int n_e^2 dl,$$

where  $\int n_e^2 dl$  is the thermal emission measure along the line of sight derived from X-ray observations,  $\nu$  is the frequency of the radio observations, and  $\xi$  has a value of 0.16 in the corona (Kundu, 1965). Using an appropriate value for  $n_e^2 dl$  in X-ray loops of  $\sim 10^{28} \text{ cm}^{-5}$ ,  $T_b \sim 5 \times 10^4$  K at 5 GHz, a value too low to explain the bright radio emission.

Gyromagnetic emission mechanisms provide the only known alternative explanation to bremsstrahlung for the bright components of the slowly varying radiation. Nonthermal gyrosynchrotron processes have been invoked, but these require continuous acceleration of electrons to explain the long lifetime of the bright components and more polarization diversity than observed. The fact that the radio brightness temperatures and the coronal electron temperatures are often nearly equal argues for a thermal mechanism (e.g., Kundu *et al.*, 1980), such as resonance absorption at harmonics of the gyrofrequency.

This theory predicts that in coronal loops, which should be optically thin to bremsstrahlung, the gyroresonance (g-r) absorption process makes the radio emission optically thick where the magnetic field strength is high and where the angle  $\theta$  between the magnetic field direction and the line of sight is large (Kundu *et al.*, 1977; Gel'freikh and Lubyshv, 1979). This mechanism has been invoked in an interpretation of bright

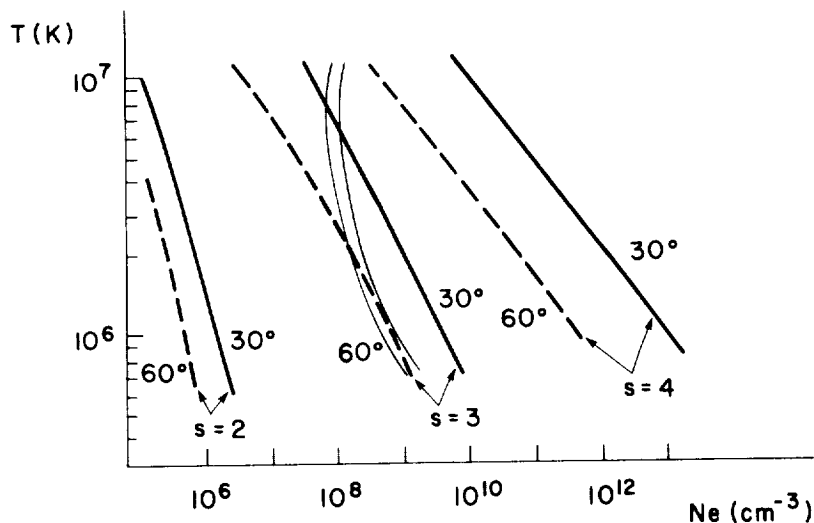


Fig. 5. Loop temperatures and electron densities required to reach unit optical depth at resonant harmonics,  $s$ , of the gyrofrequency. The observing frequency is 5 GHz and the scale length of the magnetic field strength is assumed to be  $10^9$  cm. The optical depth is larger (smaller) than unity on the right (left) side of each curve. The curved lines represent the limiting sensitivity to X-ray structures and are discussed in the text. (After Kundu *et al.*, 1980, Figure 2.)

non-sunspot components in terms of neutral sheets overlying emerging flux (Kundu and Velusamy, 1980), or emission from the tops of loops bridging magnetic inversion lines (e.g., Kundu *et al.*, 1977). In support of these interpretations, we find that generally the microwave components we observed were in regions where strong magnetic fields or high field gradients might be expected.

Figure 5 is a plot of the resonant optically thick layers as a function of temperature and electron density from the g-r theory. The curved lines indicate the limiting sensitivity of the AS&E X-ray rocket experiment for the detection of coronal loops at two fixed diameters, the maximum diameter (left) of typical AR X-ray loops and the average diameter (right) of loops in one well-studied AR (Pye *et al.*, 1978). Structures which lie to the left of these curves in terms of their electron temperature and density could not be detected in X-rays. Figure 5 implies that for those components lacking significant X-ray emission, resonance emission can only occur at the second harmonic or at high values of  $\theta$  at the third harmonic. Six cm emission at these harmonics requires fields of 900 and 600 G, respectively, in the corona. But about half of the components overlie regions where the *photospheric* magnetic field is less than these values. Even for those components with possible, faint X-ray emission (e.g., 421F) it is very unlikely that harmonics higher than 3 (and therefore lower field strengths) can be responsible for the g-r emission. Therefore, for many of the microwave components, the g-r theory implies unreasonably high magnetic field strengths in the corona.

A different problem arises in interpreting the emission from the brightest ( $T_b > 4 \times 10^6$  K) components in each region. Most of these components were associated with reasonably strong photospheric magnetic fields, but not with X-ray emission or sunspot umbrae. For a thermal interpretation of the radio emission,  $T_b \leq T_e$ . Therefore, a g-r explanation demands very high electron temperatures, low densities ( $< 10^8$  cm<sup>-3</sup>) and high coronal field strengths. We speculate on two possible explanations for this emission. High field strengths could be produced in coronal loops with significant currents. But it is difficult to understand why such currents would not also heat the loops sufficiently to emit in X-rays unless they have very low density. Hollweg (1981) recently reviewed mechanisms for producing nonthermal radio emission from runaway electrons in the corona. But 'hot' loops, which were not observed here, and high electric fields are requirements for such *coronal* radio emission. It is possible that such large electric fields are produced in the transition region, where the large temperature gradient and strong magnetic fields can readily accelerate electrons (J. Ionson, private communication). If such an interpretation for the bright, non-sunspot microwave sources is correct, then our observation of numerous, nonvarying bright sources in two undistinguished ARs suggests that continuous acceleration of particles may be common in ARs.

It is possible that we failed to detect small-scale transient or burst activity in these sources. We did not observe such activity within the limitations of our study. For instance, no H $\alpha$  flares were reported in the *Solar Geophysical Data* bulletins in either region on 16 November nor were any detected in H 419 on the BBSO film. There were no significant fluctuations observed in soft X-rays between 10:00 and 20:30 UT by the NOAA/GOES satellite at 1–8 Å. There were no changes observed on the six KPNO

magnetograms obtained between 15:43 and 21:00 UT. Finally, no statistically significant time variations in the *integrated* microwave flux were observed during continuous scanning from 15:00–16:45 UT. However, we cannot rule out the possibility of some significant variability in one or more of the bright components. In addition, the spectral characteristics of the radiation useful in distinguishing thermal and nonthermal contributions were unknown.

We find that the presence of strong, longitudinal magnetic fields is not a sufficient condition for bright microwave emission. Although many of the brightest microwave components were associated with regions of strong photospheric fields, there were other regions of apparently strong field that had no bright emission. For example, in AR H421 single pores and clusters of pores north of the main sunspot had no associated microwave emission. Also, the presence of an isolated magnetic knot north of the central sunspot of AR H419 was cospatial with bright, flare-like patches in H $\alpha$  and X-rays, but was void of microwave emission. The dependence of g-r emission on the geometry of the magnetic field and the plasma distribution apparently restricts this emission to only a limited number of coronal structures with high magnetic fields.

If the microwave emission at  $T_b = 1-4 \times 10^6$  K is due primarily to the g-r process, we can understand the lack of association between the X-ray emitting structures and the bright centimetric components. High g-r opacity is a function of a strong magnetic field and the angle  $\theta$ . If the field is too weak, the resonance layer will not be optically thick and no emission will be observed. Since X-ray emitting plasma is confined by the magnetic field in loops and the corona is highly conducting, the internal loop field strength should be low. For instance, the equipartition field strength in typical AR loops is only a few gauss and potential field extrapolations yield values of a few to tens of gauss in some AR loops (e.g., Poletto *et al.*, 1975; Levine and Withbroe, 1977). Although X-ray emission certainly arises from some loops associated with strong field regions (e.g., Webb and Zirin, 1981), most quiescent AR X-ray loops do not terminate in such regions. Therefore, we should not necessarily expect bright centimeter emission from typical AR X-ray loops.

#### Acknowledgements

The authors are grateful to the following individuals for participating in and providing data for the observations discussed in this paper: J. Harvey of KPNO for the magnetograms, H. Zirin and A. Patterson of BBSO for the optical filtergrams, R. Howard of the Mt. Wilson Observatory for sunspot positions, and P. McIntosh of the NOAA Space Environment Laboratory for an H $\alpha$  image. We thank S. Bichisecchi of the AS&E photographic laboratory for his assistance with the imagery used in this study. We benefited from discussions with E. Schmahl, S. Kahler, and A. Krieger. DFW and JMD were supported at AS&E by NASA Contract NAS5-25496. MRK and TV were supported at the University of Maryland by NSF Grant ATM 81-030839, NASA Grant NGR 21-002-199, and NASA Contract NSG 5320.

## References

- Alissandrakis, C. E., Kundu, M. R., and Lantos, P.: 1980, *Astron. Astrophys.* **82**, 30.
- Bandeira, R.: 1982, *Astron. Astrophys.* **112**, 52.
- Davis, J. M., Krieger, A. S., Silk, J. K., and Chase, R. C.: 1979, *SPIE* **184**, 96.
- Felli, M., Lang, K. R., and Willson, R. F.: 1981, *Astrophys. J.* **247**, 325.
- Gelfreikh, G. B. and Lubyshev, B. I.: 1979, *Soviet Astron.* **23**, 316.
- Gerassimenko, M., Nolte, J. T., and Petrasso, R. D.: 1976, *Solar Phys.* **48**, 121.
- Hollweg, J. V.: 1981, in F. Q. Orrall (ed.), *Solar Active Regions*, Colorado Associated University Press, Boulder, Colorado.
- Kundu, M. R.: 1965, *Solar Radio Astronomy*, Interscience, New York.
- Kundu, M. R. and Velusamy, T.: 1980, *Astrophys. J.* **240**, L63.
- Kundu, M. R., Alissandrakis, C. E., Bregman, J. D., and Hin, A. C.: 1977, *Astrophys. J.* **213**, 278.
- Kundu, M. R., Schmahl, E. J., and Gerassimenko, M.: 1980, *Astron. Astrophys.* **82**, 265.
- Kundu, M. R., Schmahl, E. J., and Rao, A. P.: 1981, *Astron. Astrophys.* **94**, 72.
- Levine, R. H. and Withbroe, G. L.: 1977, *Solar Phys.* **51**, 83.
- McIntosh, P. S., Krieger, A. S., Nolte, J. T., and Vaiana, G.: 1976, *Solar Phys.* **49**, 57.
- Nicolas, K. R., Kjeldseth-Moc, O., Bartoe, J.-D., and Brueckner, G. E.: 1982, *Solar Phys.* **81**, 253.
- Pallavicini, R., Sakurai, T., and Vaiana, G. S.: 1981, *Astron. Astrophys.* **98**, 316.
- Pallavicini, R., Vaiana, G. S., Tofani, G., and Felli, M.: 1979, *Astrophys. J.* **229**, 375.
- Poletto, G., Vaiana, G. S., Zombeck, M. V., Krieger, A. S., and Timothy, A. F.: 1975, *Solar Phys.* **44**, 83.
- Pye, J. P., Evans, K. D., Hutcheon, R. J., Gerassimenko, M., Davis, J. M., Krieger, A. S., and Vesecky, J. F.: 1978, *Astron. Astrophys.* **65**, 123.
- Schmahl, E. J., Kundu, M. R., Strong, K. T., Bentley, R. D., Smith, J. B., Jr., and Krall, K. R.: 1982, *Solar Phys.* **80**, 233.
- Solar Geophysical Data*, 1980, U.S. Department of Commerce, NOAA, Boulder, Colorado.
- Vaiana, G. S., Krieger, A. S., and Timothy, A. F.: 1973, *Solar Phys.* **32**, 81.
- Webb, D. F.: 1981, in F. Q. Orrall (ed.), *Solar Active Regions*, Colorado Associated University Press, Boulder, Colorado.
- Webb, D. F. and Zirin, H.: 1981, *Solar Phys.* **69**, 99.



4.8 Comparison of Coronal Holes Observed in Soft X-Ray and HeI 10830 Angstrom Spectroheliograms

S.W. Kahler and J.M. Davis

American Science and Engineering, Inc.  
Cambridge, Massachusetts 02139

and

J.W. Harvey

Kitt Peak National Observatory  
Tucson, Arizona 85726

ORIGINAL PAGE IS  
OF POOR QUALITY



# COMPARISON OF CORONAL HOLES OBSERVED IN SOFT X-RAY AND HE I 10830 Å SPECTROHELIOGRAMS

S. W. KAHLER and J. M. DAVIS

*American Science and Engineering, Inc., Fort Washington, Cambridge, MA 02139, U.S.A.*

and

J. W. HARVEY

*Kitt Peak National Observatory\*, Tucson, AZ 85726, U.S.A.*

(Received 31 December, 1982)

**Abstract.** We compare coronal holes observed in solar soft X-ray images obtained with rocket-borne telescopes during 1974 to 1981 with holes observed on nearly simultaneous 10830 Å maps. Hole boundaries are frequently poorly defined, and after 1974 the brightness contrast between the large scale structure and holes appears substantially diminished in both X-rays and 10830 Å. We find good agreement between soft X-rays and 10830 Å for large area holes but poor agreement for mid and low latitude small area holes, which are generally of low contrast. These results appear inconsistent with the popular view that the quiet corona is sharply separated into open magnetic field regions consisting of coronal holes and closed field regions consisting of the large scale structure.

## 1. Introduction

Coronal hole research was greatly stimulated by the solar soft X-ray and XUV observations during the Skylab mission in 1973–1974. High resolution images showing coronal holes devoid of coronal emission were available on at least a daily basis and over many solar rotations. The holes were found to be regions of magnetic field open to the interplanetary medium and inferred to be the sources of high speed wind streams. The Skylab results of coronal hole studies were summarized by Zirker (1977).

The end of the Skylab mission stimulated a search for alternative sources of information to identify coronal holes. During the mission a number of full disk spectroheliograms were obtained at Kitt Peak National Observatory in the D<sub>3</sub> line of He I at 5876 Å. A qualitative comparison by Harvey *et al.* (1974) of the KPNO D<sub>3</sub> spectroheliograms with the AS&E soft X-ray images from Skylab showed promising results for detecting coronal holes in the D<sub>3</sub> line. Improved signal-to-noise ratio observations, using He I 10830 Å, became possible at KPNO by the end of the Skylab mission. One such observation was compared with a Skylab He II 304 Å observation by Harvey and Sheeley (1977) and confirmed that a coronal hole was indeed detectable with 10830 Å. However, because routine 10830 Å observations were started just after the Skylab mission, no direct comparisons between the 10830 Å and Skylab soft X-ray data could be made.

\* Operated by the Association of Universities for Research in Astronomy, Inc., under contract with the National Science Foundation.

The contrast between coronal holes and the quiet corona viewed in the 10830 Å line is due to the enhanced population in the quiet corona of the triplet state of He I, which absorbs the continuum radiation from below. The physical problem posed by the observations is why the excited  $1s2s$  ground state of the 10830 Å transition should be so abundant when it is 19.7 eV above the ground state in an ion formed at chromospheric temperatures. Helium is unique in this respect since coronal holes cannot be discerned in lines of other abundant elements formed at chromospheric or transition region temperatures (Huber *et al.*, 1974). Goldberg (1939) suggested that an excess of ultraviolet radiation in the 500 Å region could ionize He I from its ground state. This enhanced ionization mechanism, together with the metastability of the  $1s2s$  triplet state, would thus explain the depleted population of singlet levels.

Zirin (1975) found that calculations of a model in which He is photoionized by coronal radiation and then recombines to populate the upper states were in good agreement with line intensity observations. He dismissed attempts to explain the He lines with collisional excitation models, specifically that of Milkey *et al.* (1973), as hopeless. His model as the dominant process for He line formation was soon attacked by Milkey (1975) on the grounds of an incompatibility with the observed line profiles. Shortly afterwards, Shine *et al.* (1975) developed a model of thermal diffusion of He ions into the transition region resulting in an enhanced rate of excitational collisions with high temperature electrons. Although Skylab XUV observations of the center-to-limb variations of He lines by Mango *et al.* (1978) and Glackin *et al.* (1978) suggested collisional excitation of the He I  $1s2s$  triplet state, the question of the primary excitation process still remains unsettled.

For our purposes the important fact is that the presence of the triplet state and consequent 10830 Å absorption in the chromosphere is closely coupled to the presence of overlying hot coronal material. Because of this, the distinction between active regions and the quiet corona is sharp in the 10830 Å images as it is in X-ray images. However, the correspondence between X-ray coronal holes and holes inferred from the 10830 Å maps has been examined only for the 27 June, 1974 X-ray image obtained with an AS&E rocket observation (Harvey and Sheeley, 1979). In that case only one large hole near central meridian was seen, and no detailed comparisons of the 10830 Å and X-ray hole boundaries was made. Since the 10830 Å images are now widely used to infer coronal holes (Sheeley and Harvey, 1981), it is appropriate to compare in detail the coronal holes observed in the X-ray images obtained in the AS&E solar rocket program with those of the corresponding KPNO 10830 Å images.

## 2. Data Analysis

### 2.1. INSTRUMENTATION

Since the Skylab period the X-ray Sun has been observed with AS&E grazing incidence telescopes on seven rocket flights. On each flight full disk solar X-ray images were recorded on Kodak SO-212 film using a combination of filters and exposure times.

During this time daily He I 10830 Å spectroheliograms have been recorded continually at KPNO, except for some coverage gaps ranging from several days to several months in extent. A large coverage gap occurred at the time of the 17 November, 1976 flight, so that observation, described by Nolte *et al.* (1977), is not used in this analysis. Each 10830 Å observation was taken during a 40 min period by scanning the Sun in 4 swaths each 512 arc sec wide. Except for 27 June, 1974, the scans were made in the solar east–west direction. Times shown in the figures are the midpoints of the observing periods. Details of the observations are presented in Harvey and Sheeley (1977).

The dates and times of the rocket images are listed in Table I. Two sets of paraboloid-hyperboloid mirrors have been used in the X-ray rocket program. The reflecting surfaces of the older mirrors, used primarily in pre-Skylab observations, are layers of a nickel alloy, Kanigen, deposited on beryllium. The details of that telescope were discussed by Vaiana *et al.* (1968) and Giacconi *et al.* (1969). The newer mirrors, consisting of fused silica (glass), are compared with the Kanigen mirrors in Table 1 of Davis *et al.* (1977).

TABLE I  
Rocket X-ray images

Date	Time (UT)	Mirror	Exposure and filter <sup>a</sup>	Wavelength (Å)
27 June, 1974	19:48	glass	59 s pp	8–39, 44–64
16 Sept., 1976	18:03	Kanigen	59 s pp	3–37, 44–60
31 Jan., 1978	18:41	glass	60 s pp	8–39, 44–64
7 Nov., 1979	20:53	glass	3 s Al	8–100 <sup>b</sup>
16 Nov., 1979	17:03	Kanigen	3 s Al	3–100 <sup>b</sup>
13 Feb., 1981	19:16	glass	45 s pp	8–39, 44–64

<sup>a</sup> pp is nominally 1 micron of polypropylene (C<sub>3</sub>H<sub>6</sub>) coated with 1500 Å of Al plus a 1500 Å Al prefilter. Al is 1500 Å of aluminium without a prefilter.

<sup>b</sup> The sensitivity of the photographic emulsion at the long wavelength cut-off is unknown and may well limit the bandpass to shorter wavelengths.

The principal differences between the two sets of mirrors are that the glass mirrors are characterized by a factor of 2.6 larger effective collecting area at 44 Å and by a substantially reduced point spread function.

Variations among the rocket images in mirrors, filters, and exposure times preclude the use of a uniform set of X-ray images for this study. For each flight, the exposure duration and filter of the image judged best for showing coronal holes is listed in the fourth column of Table I. Images obtained through the polypropylene (pp) filter during the Skylab mission (Vaiana *et al.*, 1977) were normally used to study coronal holes. Images were obtained through a similar filter on each rocket flight and are used here except for the two cases shown in Table I where images obtained through an ultra-thin aluminium filter were used. On 7 November, 1979 instrumental scattering from a flare at S 13 E 20 washed out the faint regions in the pp image, while the optimum 16 November, 1979 pp image was blurred from a pointing rotation. The wavelength

passbands at the 1% transmission levels for the chosen filters are given in the last column of the table.

## 2.2. DETERMINATION OF BOUNDARIES

Using transparencies overlaid on 10830 Å full disk prints, one of us (JWH) traced the apparent boundaries of inferred coronal holes. In some cases the low brightness intensity rendered the identification of the hole questionable, and these boundaries are indicated in the figures by dashed lines. In a similar manner one of us (SWK) traced the boundaries of coronal holes on transparencies overlaid on high contrast X-ray transparencies. These boundaries were first drawn to include all possible hole areas. Shaded regions were used to indicate areas where the existence of an X-ray coronal hole was questionable. These shaded regions encompassed both entire small hole candidates and the diffuse boundaries of well established holes. The high contrast of the X-ray features in and around holes allowed the X-ray hole boundaries to be traced in greater detail than those of the 10830 Å maps. Each set of hole boundaries was independently traced on images with 10.8 cm disk diameters before the comparisons were made. It should be appreciated that this determination of the position of holes and hole boundaries in both the X-ray and 10830 Å data is a subjective process. One can anticipate differences in hole boundaries determined by different observers or by the same observer at different times.

For two dates the daily 10830 Å maps were not obtained, and it was necessary to project hole boundaries from adjacent dates forward or backward in time to compare with the X-ray hole boundaries. Boundaries from the 2 February, 1978 map were projected back to 31 January, 1978, and those of 5 November, 1979 and 9 November, 1979 were projected forward and backward respectively to 7 November, 1979. In each case the Newton–Nunn rotation rates (Allen, 1963) determined the displacements traced with Stonyhurst disks.

The 10830 Å and X-ray images were aligned to within an estimated 10 arc sec by means of the active region features which were bright on the X-ray transparencies and dark on the 10830 Å prints. In the three figures the X-ray and 10830 Å boundaries are superposed for each set of images.

## 2.3. DETAILED COMPARISONS OF HOLE BOUNDARIES

Large coronal holes show a general correlation in the X-ray and 10830 Å images. The best case is that of 27 June, 1974 shown in Figure 1a. The prominent X-ray hole extends from the north pole to about 25° S in latitude and about 50° in longitude at the equator. The eastern boundaries of the X-ray and 10830 Å holes are in good agreement, but elsewhere the X-ray hole is larger, generally by several heliocentric degrees. A small but distinct neck connecting the polar and equatorial X-ray holes is absent in the 10830 Å image. The brightness contrast between the hole and the background corona is higher in this X-ray image than in the others shown here, but even so, we see that extensive parts of the hole boundaries are indistinct as indicated by shaded areas in Figure 1a.

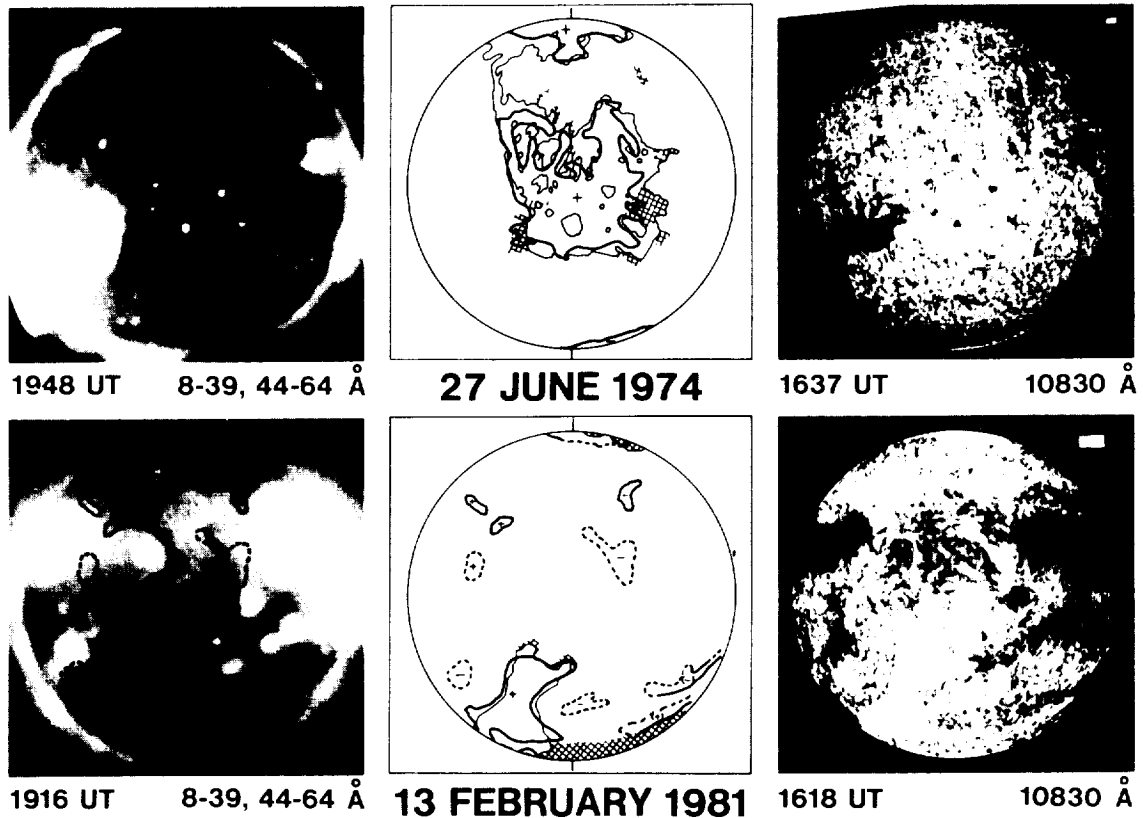
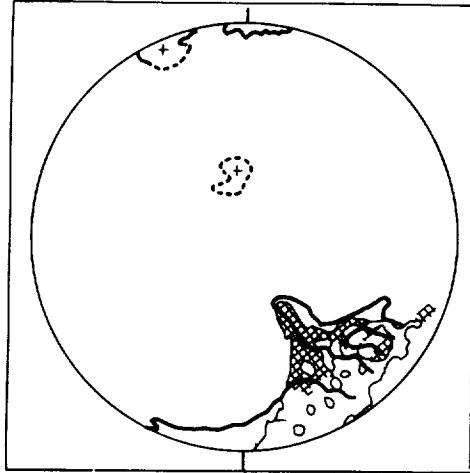


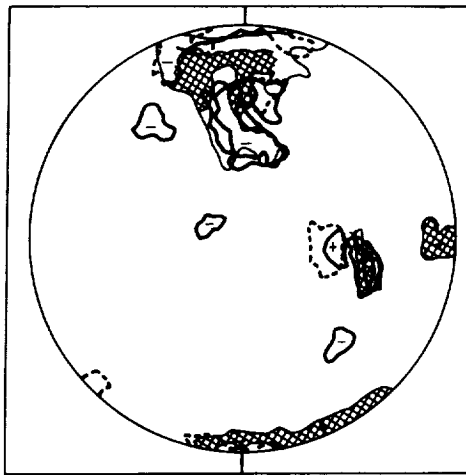
Fig. 1. *Top*: The comparison of the aligned X-ray and 10830 Å images and coronal hole boundaries for 27 June, 1974. The 10830 Å boundaries are shown in the middle panel by heavy lines, the X-ray boundaries by light lines. Hatched areas indicate uncertain X-ray holes. The north and south poles are indicated by the vertical marks on the limbs in the middle panel. *Bottom*: The same for 13 February, 1981. The heavy dotted lines are uncertain boundaries of 10830 Å holes. The 10830 Å boundaries are projected on the X-ray image.

X-ray and 10830 Å boundaries of the large polar holes observed on 13 February, 1981 (Figure 1) and 31 January, 1978 and 7 November, 1979, shown in Figure 2, also agree well to first order. The best agreement in detail is that of 13 February, 1981, but that is the only one of the three dates for which simultaneous X-ray and 10830 Å data exist.

The worst agreement between hole boundaries appears in the mid and low latitude small holes of 13 February, 1981 (Figure 1) and 7 November, 1979 (Figure 2). In the first case no evidence of the five northern latitude holes appears in the X-ray image. Similarly, there is no X-ray analog of the negative polarity hole in the southeast, but the east-west 10830 Å holes near the south pole do correspond to regions of decreased X-ray brightness. However, these latter features appear to be empty filament channels (McIntosh *et al.*, 1976), rather than holes, when compared to H $\alpha$  synoptic maps published in *Solar-Geophysical Data*.



1841 UT 8-39, 44-64 Å X-RAY AND 10830 Å HOLES  
**31 JANUARY 1978**



2053 UT 20-100 Å X-RAY AND 10830 Å HOLES  
**7 NOVEMBER 1979**

Fig. 2. *Top*: The X-ray image and comparison of X-ray and 10830 Å coronal hole boundaries for 31 January, 1978. The 10830 Å boundaries are projected back in time from the 17:29 UT image of 2 February, 1978 using the Newton–Nunn differential rotation rate. The 10830 Å hole boundaries are projected on the X-ray image. *Bottom*: The same for 7 November, 1979. The 10830 Å hole boundaries have been projected forward from the 18:25 UT image of 5 November, 1979 and backward from the 17:32 UT image of 9 November, 1979 using the Newton–Nunn rotation rate. Both sets of boundaries are shown.

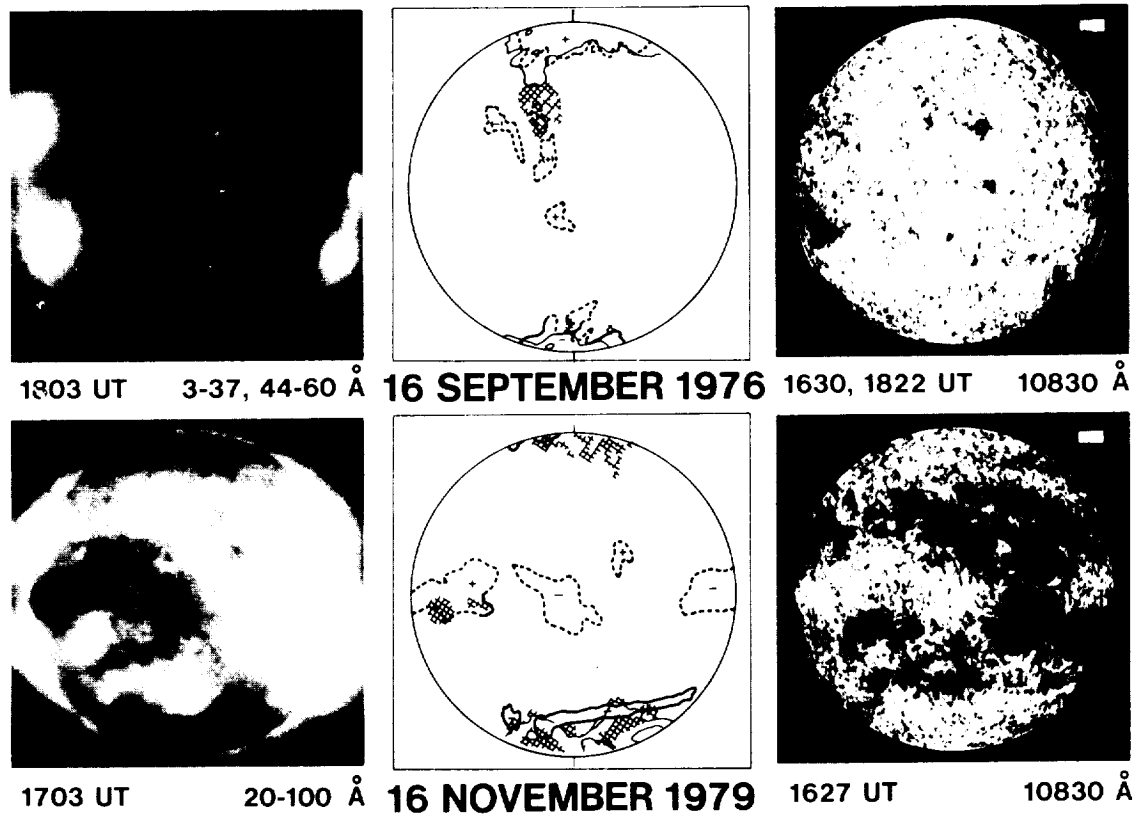


Fig. 3. The same as Figure 1 for 16 September, 1976 (*top*) and 16 November, 1979 (*bottom*). The 16 November, 1979 image is a composite of two images at the times shown.

The 7 November, 1979 comparison is compromised by the lack of simultaneous data, but here again, four small 10830 Å holes within 40° of central meridian are not associated with obvious holes in the X-ray image, although they do lie in regions of relatively low emission. In addition, an X-ray hole on the equator at the west limb was not associated with a 10830 Å hole.

To a lesser degree the data of Figure 3 also illustrate the poor correspondence of the mid and low latitude holes. The four such holes observed in 10830 Å on 16 September, 1976 are all faint and uncertain, as indicated by the dashed lines, and while they correspond to regions of low X-ray brightness, other regions of the X-ray corona are of comparable or lesser brightness. This X-ray image was obtained near solar minimum and shows a generally faint corona. The 16 November, 1979 X-ray image reflects a more active Sun, and here again the uncertain 10830 Å hole boundaries correspond only roughly to regions of low X-ray brightness. Only two small, doubtful regions appeared as low latitude X-ray holes in that image. The region of 10830 Å emission elongated in the east-west direction at S 40° is a filament channel seen in the H $\alpha$  synoptic charts of *Solar-Geophysical Data*.

One might expect to detect polar holes more easily in 10830 Å than in X-rays as a result of the obscuration of X-ray polar holes by adjacent bright coronal features such as loop arcades (McIntosh *et al.*, 1976). This does appear to be the case in the 31 January, 1978 north and south polar holes (Figure 2), but in general the X-ray holes appear larger at the poles than do the 10830 Å holes. The best example of this is the 27 June, 1974 north polar hole in which the X-ray eastern boundary is substantially farther from the pole than is that of the 10830 Å boundary. The X-ray polar hole is also substantially larger than the 10830 Å hole in those cases where we consider the hatched (uncertain) area of the X-ray hole. The south pole of 13 February, 1981, the north pole of 16 September, 1976, and both poles of 7 and 16 November, 1979 all illustrate this result.

### 3. Discussion

The Skylab X-ray images have formed the observational basis for the implicit assumption that coronal hole (CH) boundaries are sharp and well defined. Bohlin (1977) has briefly discussed the displacement of apparent hole boundaries due to foreground coronal emission, and Nolte *et al.* (1976) pointed out the occasional presence of faintly emitting X-ray regions within or near the hole boundaries which rendered those boundaries uncertain, but otherwise no indication of ambiguity in hole boundaries is found in the literature. In fact, in their quantitative Skylab X-ray study of CH1, Maxson and Vaiana (1977) concluded that the transition from coronal hole to large scale structure is sharp. However, they offered no quantitative definition of 'sharp', and both their contour plots of the boundaries and histograms of photographic density in and around hole areas suggest that the uncertainties in hole areas are large fractions of the areas themselves. Thus, past studies provide no support for the usual assumption that coronal hole boundaries are well defined.

The contrast between the X-ray brightness of the large coronal hole and that of the large scale structure in the 27 June, 1974 image (Figure 1) appears comparable to that of the Skylab images (cf. Zirker, 1977). This contrast appears considerably diminished in the X-ray images of later dates as shown in the figures. Without a quantitative photometric analysis of the X-ray holes and large-scale structures of these images, a definitive statement about possible brightness changes can not be made. However, this apparent decrease in X-ray contrast is accompanied by a comparable contrast decrease in the 10830 Å data, as indicated by the dashed 10830 Å hole boundaries in the figures. It therefore appears that non-polar holes appearing near solar minimum and during the rise phase of the current cycle are not so clearly discerned from the large scale structure as was the case during the declining phase in 1973–1974. This result, coupled with the observation that the hole boundaries are often diffuse, implies that drawing hole boundaries with either X-ray or 10830 Å data is a far more subjective process than previously believed.

Even with the above caveats, we have found a good correlation between the X-ray and 10830 Å data for the presence of large area coronal holes. In two cases (31 January,

1978 and 13 February, 1981) the large holes were at the south pole and in the other at the equator (27 June, 1974). Since the 10830 Å data allows one to infer holes at the chromospheric level, and intervening coronal emission renders polar holes less visible in X-rays, we might expect that these holes would be larger in the 10830 Å data. Evidence of this effect can be seen in the 31 January, 1978 polar hole, but it is not the rule. The dominant X-ray polar hole is distinctly larger than the corresponding 10830 Å hole on 27 June, 1974, 7 and 16 November, 1979, and 13 February, 1981, although in the last three cases the excess X-ray hole areas are uncertain as indicated by hatched areas.

We have found the worst agreement between the X-ray and 10830 Å holes at low and mid latitudes. For the period 1976 to 1981, these holes, generally seen in the 10830 Å data as weak holes, were small in diameter (10–20 solar degrees) and usually did not correspond to obvious X-ray holes. In the cases of 16 November, 1979 and 13 February, 1981 there are weak holes well away from central meridian, so the poor agreement with X-ray holes could be due to projection effects of foreground coronal material. However, all the 10830 Å maps except that of 27 June, 1974 have weak holes near central meridian with poor agreement in X-rays, so this effect is not due to projection problems.

Weak 10830 Å holes were reported by Sheeley and Harvey (1981) and appeared most often in their Bartels display during 1976–1977. They also found that the correlation between coronal holes and solar wind streams established during the Skylab period (cf. Zirker, 1977) degraded since 1976. Some recurrent holes had no observed associated wind streams, and in other cases the recurrent streams had lower peak velocities than those of Skylab. Nolte *et al.* (1977) had also found similar results using the 1976 rocket X-ray images. The role of the weak holes in the deterioration of the wind stream correlation is unclear. Most of the Sheeley and Harvey recurrent holes, confined to  $\pm 40^\circ$  latitude, were well defined, whereas in this study the low and mid latitude holes are mostly weak. On the other hand, some of the well defined holes of the Sheeley and Harvey study may well correspond to the weak holes of this study.

On the basis of the Skylab X-ray images Maxson and Vaiana (1977) have claimed that the quiet solar corona is sharply separated into two different components – the open magnetic field regions associated with coronal holes and closed field regions associated with the large scale structure. The existence of low contrast holes and indistinct hole boundaries in both the 10830 Å and X-ray images of this study is difficult to understand in the context of this two component description. These results suggest the presence of regions where closed and open field lines may be mixed. Evidence for this more complex picture was presented by Levine *et al.* (1977) based on a comparison of a harmonic analysis of the solar magnetic field with the Skylab X-ray pictures. They found evidence that the formation of open field regions preceded the occurrence of coronal holes by as much as a solar rotation. They also concluded that closed magnetic fields occupied a significant part of the area of coronal holes. More recently, Levine (1982) has presented examples of apparently open magnetic structures which cannot be identified unambiguously in He I 10830 Å spectroheliograms. Their results and ours suggest that the magnetic field in the quiet corona is complex in a way that is not yet understood.

### Acknowledgements

We are pleased to acknowledge many helpful discussions with D. F. Webb and the assistance of M. Rizza in the preparation of the photographic evidence. Support for the study at AS&E was provided by NASA under contracts NASW-3586 and NAS5-25496.

### References

- Allen, C. W.: 1963, *Astrophysical Quantities*, Athlone Press, London, p. 179.
- Bohlin, J. D.: 1977, in J. B. Zirker (ed.) *Coronal Holes and High Speed Wind Streams*, Colorado Associated University Press, Boulder, p. 27.
- Davis, J. M., Golub, L., and Krieger, A. S.: 1977, *Astrophys. J.* **214**, L141.
- Giacconi, R., Reidy, W. P., Vaiana, G. S., Van Speybroeck, L. P., and Zehnpfennig, T. F.: 1969, *Space Sci. Rev.* **9**, 3.
- Glackin, D. L., Linsky, J. L., Mango, S. A., and Bohlin, J. D.: 1978, *Astrophys. J.* **222**, 707.
- Goldberg, L.: 1939, *Astrophys. J.* **89**, 673.
- Harvey, J. W. and Sheeley, N. R., Jr.: 1977, *Solar Phys.* **54**, 343.
- Harvey, J. W. and Sheeley, N. R., Jr.: 1979, *Space Sci. Rev.* **23**, 139.
- Harvey, J., Krieger, A. S., Timothy, A. F., and Vaiana, G. S.: 1974, *Osserv. Mem. Oss. Arcetri* **104**, 50.
- Huber, M. C. E., Foukal, P. V., Noyes, R. W., Reeves, E. M., Schmahl, E. J., Timothy, J. G., Vernazza, J. E., and Withbroe, G. L.: 1974, *Astrophys. J.* **194**, L115.
- Levine, R. H.: 1982, *Solar Phys.* **79**, 203.
- Levine, R. H., Altschuler, M. D., Harvey, J. W., and Jackson, B. V.: 1977, *Astrophys. J.* **215**, 636.
- Mango, S. A., Bohlin, J. D., Glackin, D. L., and Linsky, J. L.: 1978, *Astrophys. J.* **220**, 683.
- Maxson, C. W. and Vaiana, G. S.: 1977, *Astrophys. J.* **215**, 919.
- McIntosh, P. S., Krieger, A. S., Nolte, J. T., and Vaiana, G.: 1976, *Solar Phys.* **49**, 57.
- Milkey, R. W.: 1975, *Astrophys. J.* **199**, L131.
- Milkey, R. W., Heasley, J. N., and Beebe, H. A.: 1973, *Astrophys. J.* **186**, 1043.
- Nolte, J. T., Krieger, A. S., Timothy, A. F., Vaiana, G. S., and Zombeck, M. V.: 1976, *Solar Phys.* **46**, 291.
- Nolte, J. T., Davis, J. M., Gerassimenko, M., Lazarus, A., and Sullivan, J. D.: 1977, *Geophys. Res. Letters* **4**, 291.
- Sheeley, N. R., Jr. and Harvey, J. W.: 1981, *Solar Phys.* **70**, 237.
- Shine, R., Gerola, H., and Linsky, J. L.: 1975, *Astrophys. J.* **202**, L101.
- Vaiana, G. S., Reidy, W. P., Zehnpfennig, T., Van Speybroeck, L., and Giacconi, R.: 1968, *Science* **161**, 564.
- Vaiana, G. S., Van Speybroeck, L., Zombeck, M. V., Krieger, A. S., Silk, J. K., and Timothy, A.: 1977, *Space Sci. Instr.* **3**, 19.
- Zirin, H.: 1975, *Astrophys. J.* **199**, L63.
- Zirker, J. B. (ed.): 1977, *Coronal Holes and High-Speed Wind Streams*, Colorado Associated University Press, Boulder.

4.9 X-Ray Bright Points and the Sunspot Cycle: Further Results and Predictions

John M. Davis

American Science and Engineering, Inc.  
Cambridge, Massachusetts 02139

ORIGINAL PAGE IS  
OF POOR QUALITY



# X-RAY BRIGHT POINTS AND THE SUNSPOT CYCLE: FURTHER RESULTS AND PREDICTIONS

JOHN M. DAVIS

*American Science and Engineering, Inc., Fort Washington, Cambridge, MA 02139, U.S.A.*

(Received 28 January; accepted 26 April, 1983)

**Abstract.** X-ray images obtained during two rocket flights near the maximum of sunspot cycle 21 now allow the study of the variation of X-ray bright point number over an eleven-year period covering the maxima of the last two cycles. The new data are consistent with the earlier conclusion that the temporal variation of bright point and sunspot number are out of phase. The quantities are related through a power law with a negative exponent of  $2/3$ .

## 1. Introduction

The current interest in solar variability and the solar terrestrial connection has focused attention on the Sun's magnetic activity cycle both as a source for, and as a baseline against which the variability of other phenomena can be compared. Recent studies have been wide ranging and have included the variation of the total UV flux (Cook *et al.*, 1980; Torr *et al.*, 1980), the large scale coronal structure and the solar wind (Sheeley and Harvey, 1978, 1981) and the polar solar wind (Coles *et al.*, 1980). Our efforts have been directed at understanding the behavior of regions of small scale flux emergence known as coronal or X-ray bright points (XBP). Their interest lies both in their direct relation to the solar magnetic field and in their identification as a possible source for the solar wind (Akasofu, 1983; Davis and Krieger, 1982; Mullan and Ahmad, 1982; Pneuman, 1983).

It will be remembered that bright points appear as small emission features in soft X-ray spectroheliograms. Comparison with photospheric magnetograms (Golub *et al.*, 1977) has revealed their bipolar nature and thus their similarity to ephemeral active regions (Harvey and Martin, 1973). However both this and a more recent study (Tang *et al.*, 1983) have indicated the lack of a one-to-one correspondence between bright points and ephemeral regions. For although all bright points can be directly associated with a magnetic bipole, the reverse is not true. The particular characteristics which distinguish those magnetic bipoles which are also coronal bright points from the general class of ephemeral regions remain unclear.

Davis *et al.* (1977) and Golub *et al.* (1979) have shown that the frequency of occurrence of coronal bright points is periodic and varies out of phase with sunspot number. The phase difference is close to  $180^\circ$ , i.e., the two quantities appear to be anticorrelated. This result was based upon X-ray observations made during the Skylab mission and during six sounding rocket flights covering the period 1970–1978. The Skylab data covering a six-month period in 1973, provided a continuous set of observations against which the single data points obtained during each rocket flight can be

judged. Results are now available from two further rocket flights, launched on 16 November, 1979 and 13 February, 1981, respectively, during the maximum phase of sunspot cycle 21. The addition of these two points to the data set extends the coverage to an eleven-year period containing the maxima of cycles 20 and 21.

## 2. Results and Discussion

Representative images from the two flights are shown in Figure 1. Inspection shows that there are few coronal bright points and that the background corona appears brighter than found in images taken at other times of the sunspot cycle. The increased background emission is important because of the problem of obscuration (Golub *et al.*, 1976). This governs the difference in visibility of a small feature when viewed against a background of either the weakly emitting, large scale structure or the essentially emissionless background of a coronal hole. To eliminate this difference the standard procedure for counting bright points uses short exposures where the background is at or below the threshold of detection. Although this lowers the number of bright points that are observed, it removes the bias between regions containing different structures. For the Skylab data a 4 s exposure was used.

7 NOVEMBER 1979



13 FEBRUARY 1981



Fig. 1. Full-disk X-ray images recorded on 16 November, 1979 and 13 February, 1981.

The relevant instrumental parameters for the two rocket experiments are collected in Table I. On each flight nominal exposure times of 1, 3, 9, and 27 s are available. To normalize the rocket data the bright points were counted on exposures where the product of the relative efficiency and exposure time approximates 4 s. The relative efficiency is defined as the product of the filter and prefilter transmissions and the mirror's effective collecting area at 44 Å. For these two flights 9 and 3 s images were

ORIGINAL PAGE  
BLACK AND WHITE PHOTOGRAPH

selected and the values listed in Table I are the actual exposure times measured from the telemetry record.

Although an understanding of the origin of the increased background is not essential to this study, it is useful in providing a quantitative estimate for the obscuration correction. Analysis suggests that the background arises from the presence of extended, low density loops associated with, and having temperatures typical of, active regions. This conclusion is based upon interpretation of the images and a preliminary analysis of coronal spectra recorded during the second of the two flights. The spectra came from a  $1 \text{ arc min}^2$  field centered at S03 W42. The field was located between three active regions and contained emission only from the large-scale structure. A line ratio analysis of various hydrogen-like and helium-like ions leads to a plasma temperature of  $2.5 \times 10^6 \text{ K}$ . This is above the range of  $1.5$  to  $2.1 \times 10^6 \text{ K}$  previously reported for the quiet Sun (Withbroe, 1975; Maxson and Vaiana, 1977; Mariska and Withbroe, 1978) and which has at other phases of the sunspot cycle formed the background against which the earlier bright point counts were made.

For X-ray telescopes the power emitted by a plasma in the temperature range  $1$  to  $6 \times 10^6 \text{ K}$ , integrated over all wavelengths, reaching the focal plane is proportional to the second power of the electron temperature (see Vaiana *et al.*, 1977, Figure 32). Thus an increase in coronal temperature from  $2.0$  to  $2.5 \times 10^6 \text{ K}$  will raise the detected emission by a factor of  $1.5$ . That is, the background on a  $4 \text{ s}$  exposure from the rocket flights at solar maximum should be comparable to that on a  $6 \text{ s}$  exposure from the earlier period. This is found to be the case, and although this analysis is almost certainly an oversimplification, it has been used as the basis for correcting the data for the increased obscuration. The approach can be justified by noting that the temperature of the large-scale structure is likely to vary over the solar surface and will almost certainly be lower outside the active region zone. Thus the correction factor should be conservative. However one might also expect an accompanying increase in the amount of material at these temperatures with the increased background arising from a combination of both these factors. The increase in density of the large-scale structure must be rather modest for the emission measure, estimated from the spectrometer data, is not inconsistent with the results of Maxson and Vaiana (1977). Thus the higher temperature appears to make the dominant contribution to the increased background and applying the correction factor of  $1.5$  to the observations from the whole disk is more likely to cause the number of bright points to be over- rather than underestimated.

On balance the factor of  $1.5$  is believed to be a reasonable correction for the increased obscuration. Using this value the corresponding decrease in bright point visibility is approximately  $30\%$  (see Golub *et al.*, 1976, Figure 1). Therefore the measured values have been increased accordingly by a factor of  $1.3$ . A final correction was applied to compensate for the fraction of the observable disk occupied by active regions at the time of the observations and which were therefore excluded from the area in which bright points were counted. The data are summarized in Table I.

The variation with time over sunspot cycles 20 and 21 of the corrected bright point counts is shown in Figure 2 where they are compared with the yearly averaged sunspot

TABLE I  
Instrumental characteristics and bright point statistics

Date	Relative efficiency at 44 Å	Exposure (s)	$N_{\text{meas.}}$	Active region correction	$N_{\text{corrected}}$
16 Nov., 1979	0.433	8.94	9	1.16	$13.6 \pm 3.5$
13 Feb., 1981	1.233	2.84	7	1.27	$11.6 \pm 3.4$

number. The new data provide additional support to our previous conclusion that the temporal variation of large and small scale flux emergence is out-of-phase. Both sets of measurements have been normalized to their greatest values which occur for sunspots at the maximum of cycle 21 and for bright points at the minimum between the two cycles. It is possible that this presentation overemphasizes the single peak in the bright point data and the absolute amplitude of the bright point curve should be viewed with this in mind since we do not yet know whether the magnitude of the peak is typical of bright point behavior.

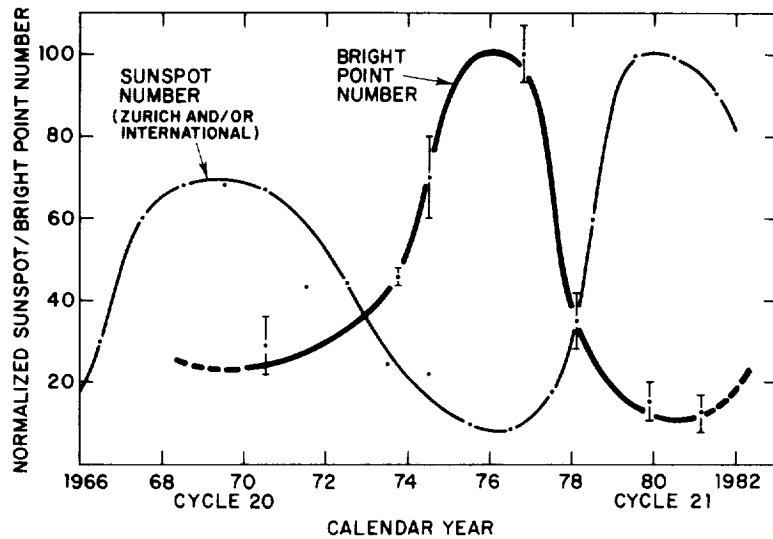


Fig. 2. Variation of the number of X-ray bright points over sunspot cycles 20 and 21.

To test for interdependence between these indicators of large and small scale flux emergence we have compared the corrected bright point counts with the weekly average sunspot number, centered on the day of the bright point observation (Figure 3). A weekly sunspot average was used to provide a measure of global, rather than local activity. The data fit a power law of the form

$$N_{\text{XBP}} = 421.1 N_{\text{SS}}^{-0.662}.$$

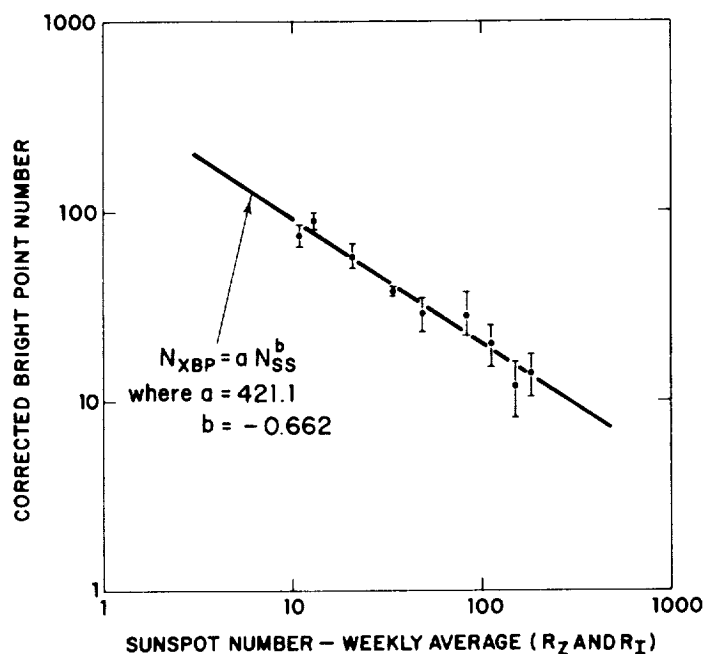


Fig. 3. The dependence of the number of bright points on the weekly average sunspot number.

The reduced  $\chi^2$  for the fitted curve is 0.9 and  $P(\chi^2)$  is 0.5 indicating an acceptable fit to the data. The fact that the data points are from two sunspot cycles suggest that this relation could be used successfully as a first order predictor of future bright point behavior.

The anticorrelation of the small and large-scale components of the emerging flux spectrum has been interpreted as evidence of a constant pattern of flux emergence over a solar cycle (Golub *et al.*, 1979). This hypothesis has been questioned (Bonnet, 1981) in light of the result of Howard and LaBonte (1981) who find that considerably more flux is emerging during cycle 21, than emerged during cycle 20. However, the constant flux hypothesis was based on the observations over a single cycle, for which the result is still valid. It did not exclude inter-cycle variations in the total flux emergence. However, bright point data now exist from the maximum phase of two cycles. The comparison of these data show that the bright point minimum at the maximum of cycle 21 falls approximately a factor of 2 below the value at the previous maximum. Interpretation of this result in terms of the power law relationship suggests that the higher level of small scale flux at the cycle 20 maximum is compensating for the lower level of large scale flux and vice versa at the maximum of cycle 21.

The implication of this result is that the amplitude of the bright point maximum at the next solar minimum will depend more on the depth of the sunspot minimum than on the difference in the total flux between cycle 20 and 21. Since the 1976 minimum was not deep by historical standards, the observed numbers being over twice the mean of

cycles 8–20, the possibility exists for even more dramatic XBP increases at future solar minima.

Finally, many aspects of the behavior of XBP remain enigmatic. The reason for the lack of correspondence, for instance, between the temporal behavior of bright points and ephemeral regions, which do not appear to show the dramatic out-of-phase variation with sunspots (Martin and Harvey, 1979), is still not known. All studies have shown that ephemeral regions are more numerous than bright points but no study has yet elucidated the particular characteristics which distinguish the two phenomena. We support the conclusion of Tang *et al.* (1983) that joint simultaneous, high spatial resolution, observations (soft X-ray and magnetograms) of several days duration are necessary to resolve this problem and suggest that the observation period provided by a space shuttle flight, scheduled late in the declining phase of the current cycle, would be ideal for this test.

#### Acknowledgement

This work has been supported by NASA under contract NAS5–25496.

#### References

- Akasofu, S.-I.: 1983, *Solar Wind Five* (in press).
- Bonnet, R. M.: 1981, *Solar Phys.* **74**, 485.
- Coles, W. A., Rickett, B. J., Rumsey, V. H., Kaufman, J. J., Turley, D. G., Ananthakrishnan, S., Armstrong, J. W., Harmons, J. K., Scott, S. L., and Sime, D. G.: 1980, *Nature* **286**, 239.
- Cook, J. W., Brueckner, G. E., and Van Hoosier, M. E.: 1980, *J. Geophys. Res.* **85**, 2257.
- Davis, J. M., Golub, L., and Krieger, A. S.: 1977, *Astrophys. J.* **214**, L141.
- Davis, J. M. and Krieger, A. S.: 1982, *Fifth International Symposium on Solar Terrestrial Physics*, COSPAR XXIV, Ottawa, Canada, p. 25.
- Golub, L., Krieger, A. S., and Vaiana, G. S.: 1976, *Solar Phys.* **50**, 311.
- Golub, L., Krieger, A. S., Vaiana, G. S., and Harvey, J. W.: 1977, *Solar Phys.* **53**, 111.
- Golub, L., Davis, J. M., and Krieger, A. S.: 1979, *Astrophys. J.* **229**, L145.
- Harvey, K. L. and Martin, S. F.: 1973, *Solar Phys.* **32**, 389.
- Howard, R. and LaBonte, B. J.: 1981, *Solar Phys.* **74**, 131.
- Mariska, J. T. and Withbroe, G. L.: 1978, *Solar Phys.* **60**, 67.
- Martin, S. F. and Harvey, K. L.: 1979, *Solar Phys.* **64**, 93.
- Maxson, C. W. and Vaiana, G. S.: 1977, *Astrophys. J.* **215**, 919.
- Mullan, D. J. and Ahmad, I. A.: 1982, *Solar Phys.* **75**, 347.
- Pneuman, G. W.: 1983, *Astrophys. J.* **265**, 468.
- Sheeley, Jr., N. R. and Harvey, J. W.: 1978, *Solar Phys.* **59**, 159.
- Sheeley, Jr., N. R. and Harvey, J. W.: 1981, *Solar Phys.* **70**, 237.
- Torr, M. R., Torr, D. G., and Hinteregger, H. E.: 1980, *J. Geophys. Res.* **85**, 6063.
- Tang, F., Harvey, K., Bruner, M., Kent, B., and Antonucci, E.: 1983, *Adv. Space Res.* **2**, No. 11, 65.
- Vaiana, G. S., Van Speybroeck, L., Zombeck, M. V., Krieger, A. S., Silk, J. K., and Timothy, A.: 1977, *Space Sci. Instr.* **3**, 19.
- Withbroe, G. L.: 1975, *Solar Phys.* **45**, 301.

4.10 Observations of the Reappearance of Polar Coronal Holes and the Reversal  
of the Polar Magnetic Field

D.F. Webb and J.M. Davis

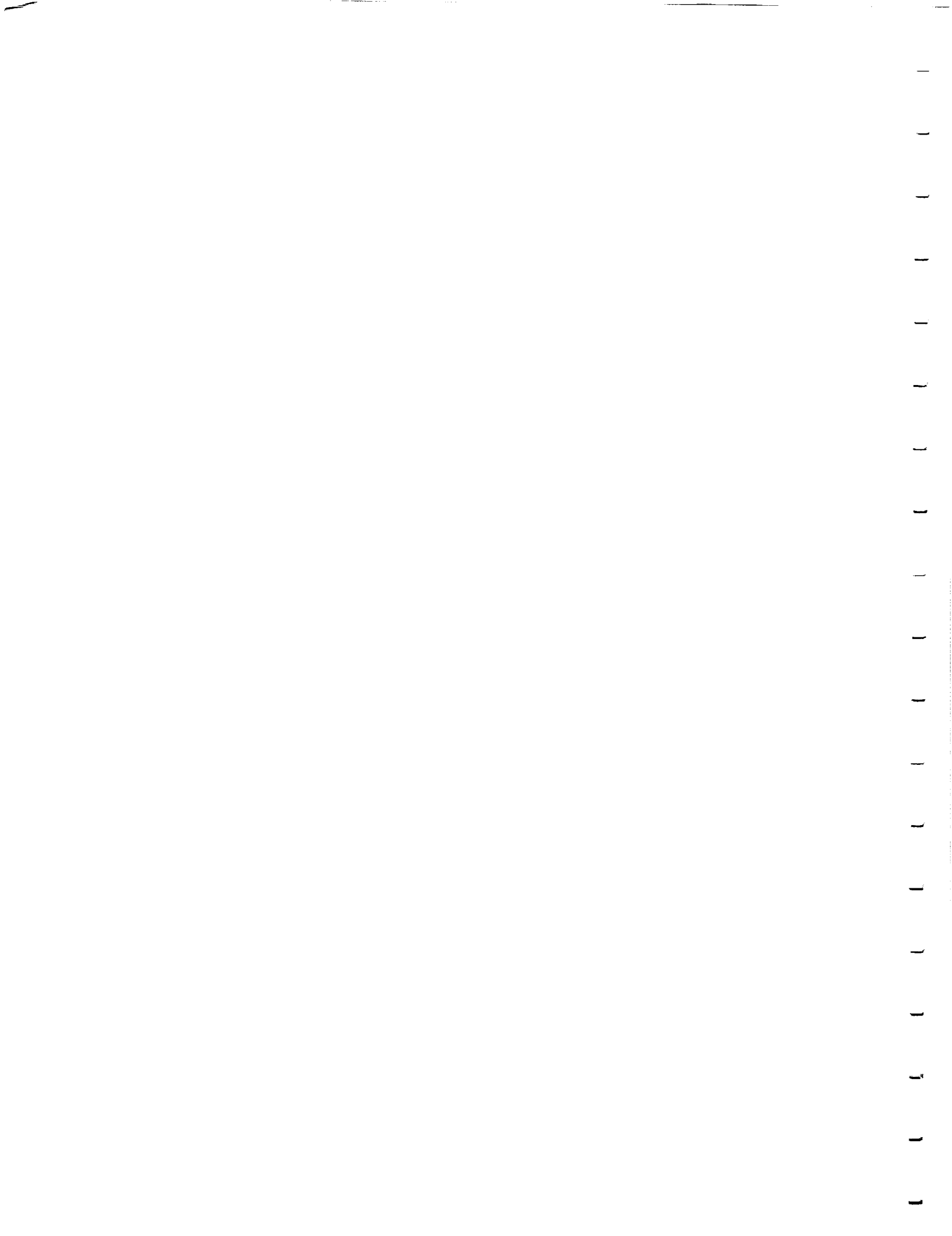
American Science and Engineering, Inc.  
Cambridge, Massachusetts 02139

and

P.S. McIntosh

Space Environment Laboratory  
National Oceanic and Atmospheric Administration  
Boulder, Colorado 80303

ORIGINAL PAGE IS  
OF POOR QUALITY



# OBSERVATIONS OF THE REAPPEARANCE OF POLAR CORONAL HOLES AND THE REVERSAL OF THE POLAR MAGNETIC FIELD

D. F. WEBB and J. M. DAVIS

*American Science and Engineering, Inc., Cambridge, MA 02139, U.S.A.*

and

P. S. McINTOSH

*Space Environment Laboratory, National Oceanic and Atmospheric Administration,  
Boulder, CO 80303, U.S.A.*

(Received 28 September, 1983; in revised form 9 January, 1984)

**Abstract.** We examine observations relating to the evolution of the polar magnetic field around sunspot maximum, when the net polar flux reverses polarity and coronal holes redevelop around the poles. Coronal hole observations during the last two solar maxima are examined in detail. Long-term averages of the latitudinal dependence of the photospheric magnetic field and the evolutionary pattern of the polar crown filaments are used to trace the poleward motion of the reversal of the large-scale surface field, and are compared to the redevelopment of the polar holes. The polar holes evolve from small, mid-latitude holes of new-cycle polarity which expand poleward until they join and cover the pole. We find that the appearance of these mid-latitude holes, the peak of flux emergence at low latitudes, and the polar polarity reversal all occur within a few solar rotations. Lagging 6 months to  $1\frac{1}{2}$  yr after this time, the polar crown disappears and the polar holes redevelop.

These results are examined in the context of phenomenological models of the solar cycle. We believe the following results in particular must be accounted for in successful models of the solar cycle: (1) The process of polarity reversal and redevelopment of the polar holes is discontinuous, occurring in 2 or 3 longitude bands, with surges of flux of old-cycle polarity interrupting the poleward migration of new-cycle flux. There is a persistent asymmetry in these processes between the two hemispheres; the polarity reversal in the two hemispheres is offset by 6 months to  $1\frac{1}{2}$  yr. (2) Contrary to the Babcock hypothesis, the polar crown disappears months *after* the magnetic polar reversal. We suggest one possible scenario to explain this effect. (3) Our observations support suggestions of a poleward meridional flow around solar maximum that cannot be accounted for by Leighton-type diffusion.

## 1. Introduction

The simplest description of the solar magnetic field is as a dipole oriented along the rotation axis with radial, unipolar fields at the poles. These polar fields are strongest and of maximum area at solar minimum. Because coronal holes form in regions where the large-scale field is unipolar, we expect the poles to be covered by holes at solar minimum and this has been consistently observed (Waldmeier, 1981; Sheeley, 1980; Nolte *et al.*, 1977).

Recent phenomenological concepts of the formation and development of coronal holes (e.g., Bohlin and Sheeley, 1978; Hundhausen, 1977) have generally invoked the ideas originally outlined by Babcock (1961) and Leighton (1964) for the explanation of the solar cycle. The Babcock and Leighton models are qualitative descriptions of the evolution of surface magnetic fields placed in the context of a dynamo theory. In these

models a weak initial poloidal field is amplified by the solar differential rotation to form a strong toroidal field. This field rises to the surface by magnetic buoyancy where it forms bipolar magnetic regions (BMRs). The BMRs are dispersed by random walk diffusion which preferentially directs the following polarity fields poleward. During this period cyclonic convection, acting on the toroidal field, produces a toroidal current and an associated poloidal field of reverse polarity to the initial field. Eventually this new poloidal field becomes dominant and the cycle reverses. Models based on these ideas are called kinematic, or  $\alpha - \omega$  dynamos (e.g., Stix, 1981). However their basic assumptions are not universally accepted and models called oscillator theories exist which are based on the existence of a deep-seated, primordial field (e.g., Layzer *et al.*, 1979). These models are generally not as well developed, mathematically, as the kinematic dynamos.

Obviously the period of the reversal of the polar fields contains information which must be explained by any successful theory. In this study we examine new observations relating to the evolution of the high latitude and polar magnetic field around solar maximum to provide a firm observational context for the development of solar cycle models. For this purpose we will derive the relative timing near the maxima of solar cycles 20 and 21 of five specific events in each solar hemisphere. These are the peak of the sunspot number, the magnetic polarity reversal above  $70^\circ$  latitude, the disappearance of the polar crown of filaments, the first appearance of a small, mid-latitude coronal hole(s) of new-cycle polarity, and the earliest coverage of the pole by a hole. It will be shown that the data set allows each of these events to be determined within a few solar rotations.

The data set emphasizes high spatial resolution synoptic coronal observations which were not previously available. Coronal hole studies have shown an intimate spatial relationship between coronal holes and large-scale unipolar areas; therefore, we expect the development of high-latitude and polar coronal holes to provide insight into the process of the polarity reversal of the polar fields. Sufficient synoptic data have now been accumulated to permit the study of two consecutive cycles of polar hole development around sunspot maximum.

Hundhausen *et al.* (1981, hereafter HHH) and Broussard *et al.* (1978) have shown that 'mid-latitude' holes (those centered at latitudes roughly between  $20$  and  $60^\circ$ ) were a feature of the corona during the maximum of cycle 20. In Section 2 we describe the high-latitude evolution of coronal holes around the maxima of cycles 20 and 21, and show that one of the characteristics of this evolution was the areal increase and poleward growth of particular mid-latitude holes of new-cycle polarity, to eventually cover the poles. In Section 3 we describe the evolution of the high-latitude magnetic field using observations of the migration of the polarity reversal of the photospheric field and of the migration and dissolution of the polar crown. In Section 4 we summarize our results with the goal of guiding the development of future models of the solar cycle.

## 2. High-Latitude Coronal Hole Evolution around Sunspot Maximum

The coronal data used for this study included AS & E X-ray rocket images, Harvard OSO-6 Mg x maps for cycle 20, eclipse data on 7 March, 1970, synoptic High Altitude Observatory (HAO) white light K-coronameter charts for cycle 20, and synoptic He I -10830 Å coronal hole boundaries for cycle 21. Various formats of H $\alpha$  synoptic charts from the NOAA Space Environment Laboratory were used to trace the poleward migration of filaments and of the large-scale magnetic field. Graphs of the latitudinally averaged photospheric field from Mt. Wilson were used to trace the poleward migration of the polarity reversals at the times of maxima. In Figure 1, the times of the rocket and OSO-6 data are superposed on the sunspot data for cycles 20 and 21 using smoothed values of  $R_z$ , the Zürich sunspot number, normalized to the starting minima of the cycles in October 1964 and June 1976, respectively.

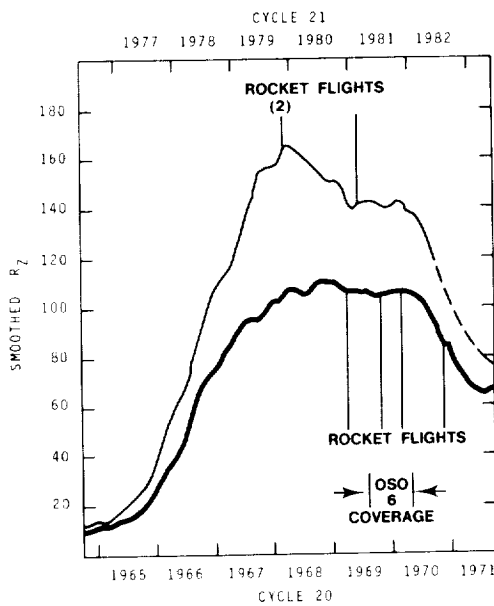


Fig. 1. The rise, maximum and early decline phases of solar sunspot cycles 20 (bottom curve) and 21 (top). The curves show smoothed values of  $R_z$ , the Zürich sunspot number, normalized to their starting minima in October 1964 (bottom) and June 1976 (top). The dashed line represents predicted  $R_z$  through late 1982 and early 1983. These data are adapted from the *Solar-Geophysical Data Bulletin*. The vertical lines denote the times of AS & E X-ray rocket flights (there were 2 in November 1979), and the arrows indicate the time coverage of the Harvard OSO-6 Mg x movie.

The maximum of cycle 20 was broad, with shape and peak similar to the average profile of the previous 12 cycles. In contrast, cycle 21 was the second most active sunspot cycle in recorded history. Compared to cycle 20 it had a steeper rise and an earlier and narrower peak. It is important to compare the patterns of evolution in the polar regions for these two cycles, which have such different levels and distributions of

magnetic activity. In this section we will examine the evolution of the high-latitude coronal holes which lead to the reformation of the polar holes.

### 2.1. THE REDEVELOPMENT OF THE POLAR HOLES IN CYCLE 20

The structure of the corona during the maximum of cycle 20 was observed in 1969 with the use of *K*-coronal observations (HHH) and EUV and soft X-ray images obtained by rocket flights (Krieger *et al.*, 1971, Figure 6; Broussard *et al.*, 1978). The rocket images corroborate the description given by HHH: that the corona was characterized by the absence of polar holes and the presence of elongated mid-latitude holes. In particular, the AS & E X-ray image on 4 November, 1969 (Carrington Rotation 1554) showed that there was no polar coronal hole in the south. The magnetic field data showed no dominant polarity at high latitudes until 1970.

For this cycle the exact time of reappearance of polar coronal holes is difficult to determine because of the low resolution of the *K*-corona data and the infrequent rocket X-ray images, as well as the cyclical tilting of the solar poles toward and away from our line of sight. HHH noted that by mid-1970 (CR 1561–63) dominance by a single polarity had begun to appear in both hemispheres. The polarities (positive in the north, negative in the south) were those expected for the new cycle following sunspot maximum.

Our interpretations of the timing of the coverage, or encirclement of the polar caps by coronal holes from the *K*-coronameter maps differ from those of HHH. Using a more conservative approach to the data, they claimed that the southern polar hole did not appear until early 1971 (CR 1572). The earliest indication in the *K*-coronameter data of a large coronal hole extension to the southern pole was in July 1970 (CR 1563). By October (CR 1567) a coronal hole could be observed poleward of  $S 70^\circ$  latitude at all solar longitudes. Although there were gaps in the *K*-coronameter data during this period, we believe that these data imply complete coverage of the polar cap by a hole at this time. An unambiguous southern polar hole was visible on the AS & E X-ray image taken on 24 November, 1970 (CR 1568) (Krieger *et al.*, 1973). This asymmetric hole extended to the equator at about  $L = 270^\circ$ , and could be traced as a continuous feature of the corona back to July 1970.\*

The critical period of late 1969 to mid-1970 was studied with the use of a cine presentation of the corona obtained with the Harvard spectroheliograph on the OSO-6 satellite (Withbroe 1981; Withbroe *et al.*, 1971),  $H\alpha$  synoptic charts (McIntosh, 1979), and coronal data obtained on 7 March, 1970, the date of a total solar eclipse at Earth. The OSO-6 movie revealed the gradual development of three coronal holes which we believe were the earliest indication of the new-cycle magnetic organization leading to the formation of the southern polar hole. These holes appeared at mid-latitude and expanded in longitude and toward the south until they reached the pole. All were of negative polarity, in agreement with the subsequent polarity of the south pole.

\* It was identified with the first long-lived, recurrent high speed wind stream following solar maximum (Krieger *et al.*, 1973; Sheeley *et al.*, 1977). The stream first appeared on August 1970 (CR 1564), in agreement in time, polarity, and longitude with the southern coronal hole.

The centroids of the holes were relatively stationary in longitude, with average Carrington longitudes of 20, 110, and 220°. The hole at  $L \simeq 110^\circ$  stretched across the central meridian on the day of the 7 March, 1970 eclipse and, hence, was well observed. It was bordered in the south by the polar crown of filaments prior to March 1970 (CR 1558), implying that the hole did not extend to the pole prior to that rotation. The polar crown began to break up on CR 1558.

The eclipse data clarify these observations. Figure 2 is a superposition of the 7 March AS & E X-ray image of the inner corona and the HAO ground-based image of the white-light outer corona. The X-ray image revealed large areas of low emission, similar in appearance to coronal holes, surrounding both poles. The solar  $B_0$  angle, denoting the tilt of the solar equator to the ecliptic, had its maximum negative value, exposing the south pole to our view. Gaps in the X-ray limb emission at position angles of  $180^\circ$  and  $215\text{--}240^\circ$  (measured CCW from north) corresponded to gaps in the white-light emission (Van Speybroeck *et al.*, 1970; HHH). These corresponded to the small hole near the south pole and the large hole at  $L = 220^\circ$  observed by OSO-6. In X-rays the region between these two 'accepted' holes contained similar low emission, suggesting that there were no intervening bright arcades that would indicate changes of magnetic polarity. Thus, the high southern latitudes appeared to be dominated by a single polarity.\*

Figure 3 shows the  $H\alpha$  synoptic map which includes the date of the eclipse (CR 1558). The top map has superimposed on it the boundaries of the coronal holes carefully drawn from the 7 March, 1970 X-ray image (Figure 2). Although the boundaries are subjective (e.g., Kahler *et al.*, 1983), our determinations are based on the use of film transparencies, which reveal subtle contrast differences not visible on prints. The double dashed lines mark regions where filament arcades may cause obscuration of the hole boundaries. The bottom map shows the  $2$  and  $3 \times 10^{-8} pB$   $K$ -coronameter contours from the west-limb data of HHH. Comparison of these maps reveals that: (1) in the southern hemisphere the  $3 \times 10^{-8} pB$  contour lies within the negative polarity cell; (2) part of the southern coronal hole visible on the X-ray image is of uniform darkness and its boundary generally follows that of the  $3 \times 10^{-8}$  contour; (3) the small positive-polarity hole near the center of the X-ray disk (S25,  $135^\circ L$ ) is not visible in the white light data.

These observations suggest that by March 1970 the large-scale south polar field was dominated by the polarity of the new cycle, with a small area of the south polar region possibly covered by an asymmetric hole. The south polar region did not become completely encircled by a hole until about October 1970.

The above comparison indicates that, at this time of the solar cycle, the  $3 \times 10^{-8} pB$  contour of the  $K$ -coronameter data may be a better approximation for the boundaries of high latitude coronal holes. We believe that HHH's interpretation of the timing of the reappearance of the polar holes was overly conservative. Their use of a single, average contour ( $2 \times 10^{-8}$ ) to define hole boundaries over the entire cycle and their

\* We believe that the white-light helmet streamer lying at  $180\text{--}215^\circ$  had its base in the hidden hemisphere, contrary to HHH's interpretation.

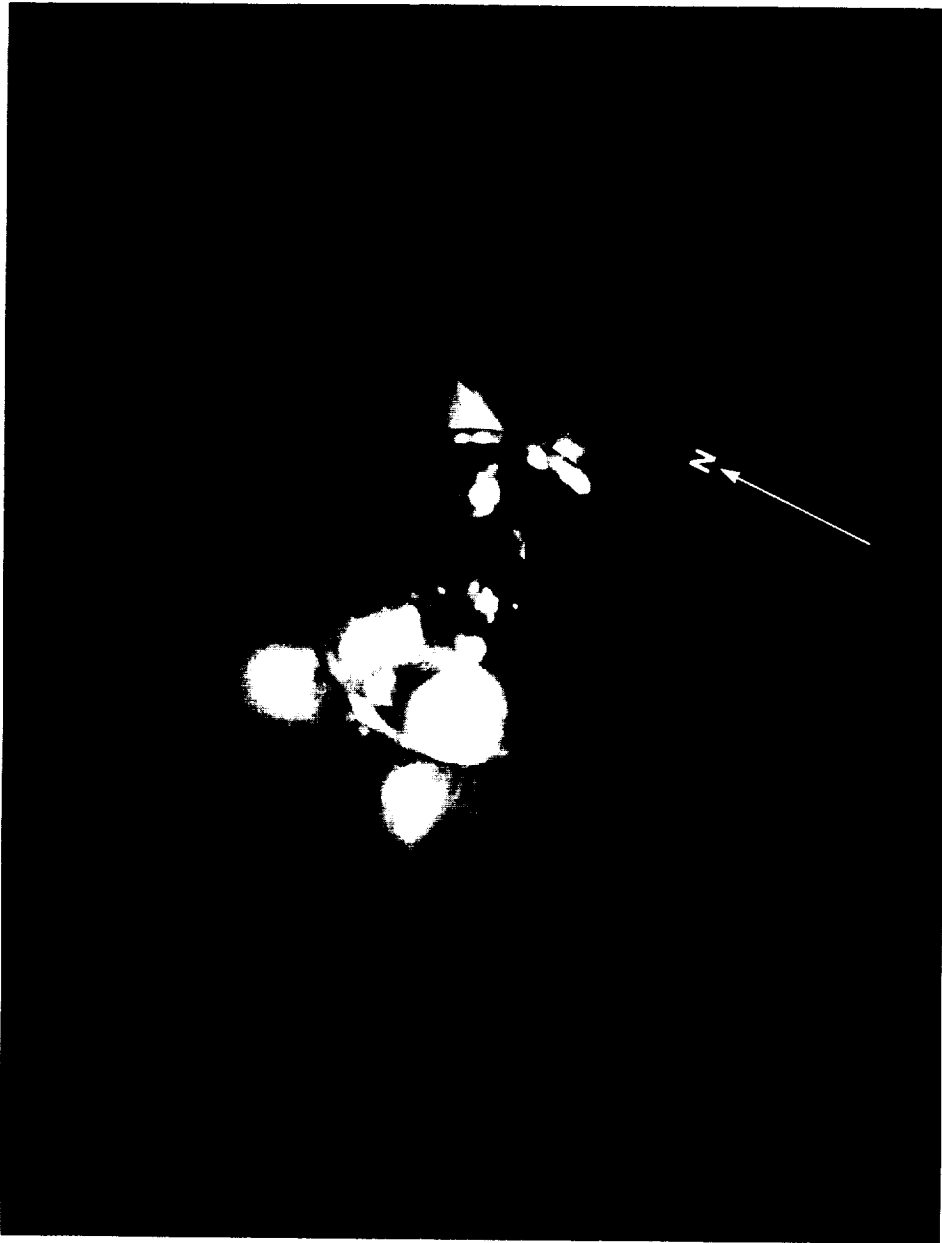


Fig. 2. A superposition of an AS & E X-ray image of the inner corona obtained during a rocket flight and a ground-based HAO white light image of the outer corona. Both were taken during the solar eclipse of 7 March, 1970. The X-ray image had passbands of 3–30 and 44–55 Å. The arrow indicates solar north.

ORIGINAL PAGE  
BLACK AND WHITE PHOTOGRAPH

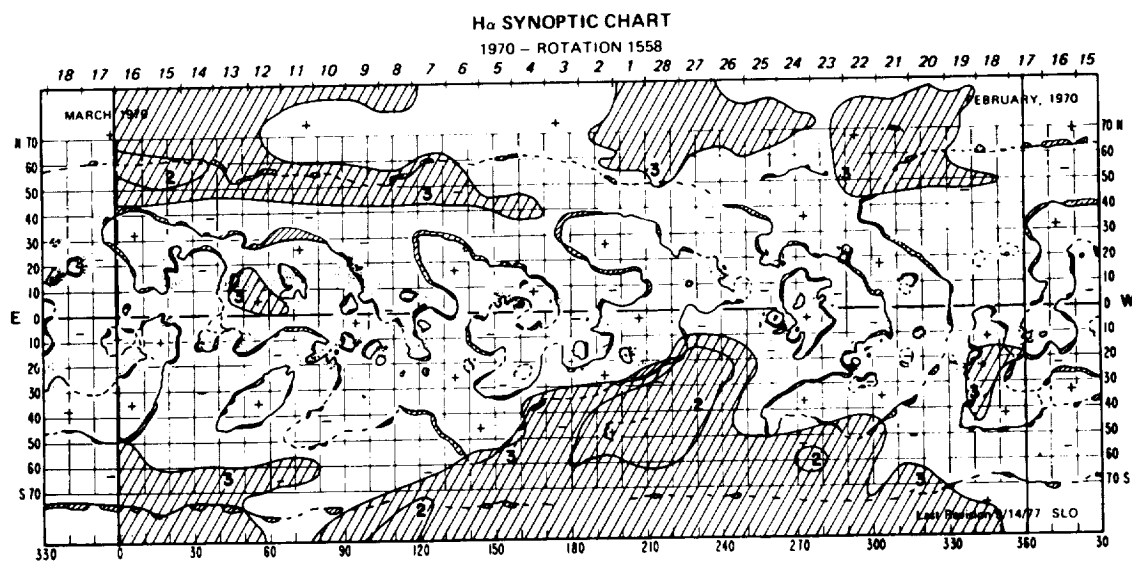
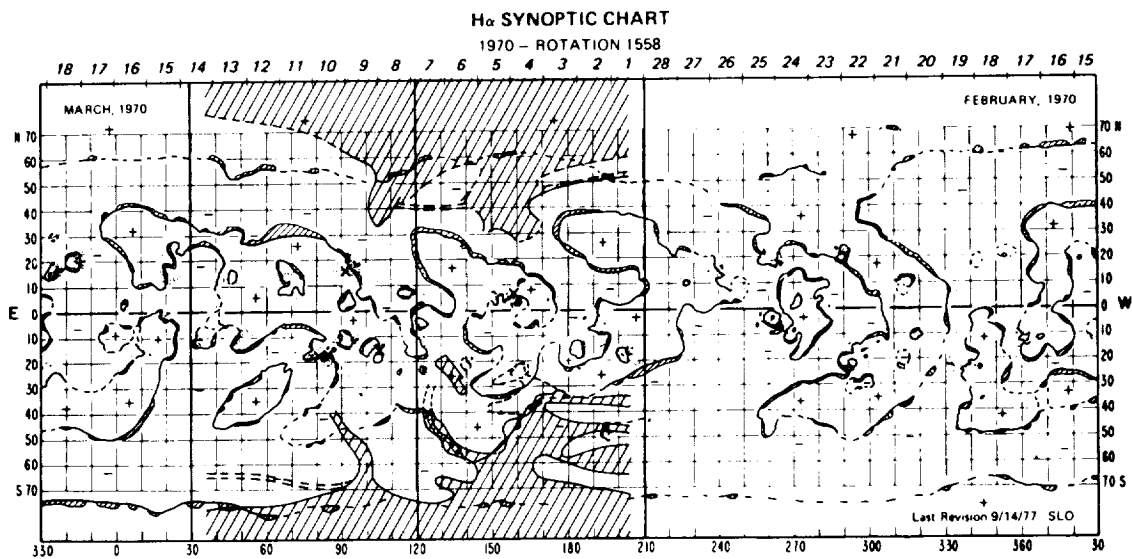


Fig. 3. Coronal data superimposed on an H $\alpha$  synoptic chart for CR 1558 (McIntosh, 1979). (a) Boundaries of coronal holes drawn from the 7 March, 1970 X-ray image in Figure 2. The three vertical lines represent the positions of the east limb (left), CMP (center) and west limb (right) on that day. Single dashed lines indicate uncertain boundaries; double dashed lines indicate the locations of coronal filament cavities. The 'x's mark the location of sunspots observed with the X-ray experiment, and provide a benchmark of the accuracy of transferring the X-ray data to the rectangular format. (b) The  $2$  and  $3 \times 10^{-8}$   $pB$  contours of the white light  $K$ -corona adapted from the west limb synoptic data of HHH.

TABLE I  
Polar events associated with sunspot maximum

Cycle No.	Pole <sup>(1)</sup>	Sunspot peak <sup>(2)</sup>	Polarity reversal above 70° lat.	Mid-latitude hole appearance	Polar crown disappearance	Earliest polar coverage by a hole
21	N	July–Nov. 1979 1684–88 <sup>(3)</sup>	Mar. 1980 1692–93 (Feb.–Mar. 1982 1719)	Dec. 1979–Jan. 1980 1690 May 1980 1695	Oct.–Nov. 1980 1701	July–Aug. 1981 1711–12
	S	Mar.–July 1980 1692–97	Sept. 1980 1699	May 1980 1695 Nov.–Dec. 1981 1715	Apr.–May 1981 1707	June 1981–Jan. 1982 1710–16
20	S	Oct. 1969 1553	Sept. 1969 1552	≥ Oct. 1969 ≥ 1553	May 1970 1561	July–Oct. 1970 1563–67
	N	June 1970 1562	July 1970 <sup>(4)</sup> 1563 (Aug. 1971 1577)	≤ May 1970 <sup>(5)</sup> ≤ 1561 Jan. 1971 1570	Sept. 1969 <sup>(6)</sup> 1552 June–July 1971 1576	Mar.–Apr. 1971 <sup>(7)</sup> 1572–73
19	S	Aug. 1957	Mar.–July 1957 <sup>(8)</sup>	–	Jan. 1959 <sup>(9)</sup>	–
	N	Jan. 1959	Nov. 1958 <sup>(8)</sup>	–	Oct. 1959 <sup>(9)</sup>	–

(1) The first pole listed in each cycle switched polarity earliest.

(2) Peak in each hemisphere. Data for cycles 19 and 20 are from White and Trotter (1977). Data for cycle 21 were derived from NOAA–SESC sunspot group numbers (see text).

(3) Carrington rotation number.

(4) From Howard (1974). The earliest time was the first reversal to positive polarity. The second time was the 'final' reversal to positive polarity.

(5) From the data of Hundhausen *et al.* (1981). The earliest time is our estimate of the hole's original time of formation. The last time is HHH's time when the hole 'reformed'.

(6) The earliest time was when the polar crown preceding positive polarity disappeared. The second time was when the 'final' polar crown preceding positive polarity disappeared.

(7) From the data of HHH.

(8) From Babcock (1959).

(9) Estimated from Waldmeier (1981); Figure 5.

definition of polar encirclement only when the pole appeared to be surrounded by a uniform band of low emission separated from the 'equatorial corona by a steep brightness gradient' yields estimates of polar hole rebirths which are, consistently, several rotations later than our estimates of the earliest coverage. It is important to emphasize that in our data set we seek the earliest time when we can be reasonably certain that each pole is covered by a hole, no matter how small or asymmetric, and which will persist in subsequent rotations. This time, or a window of times, will appear in Table I under the column 'Earliest Polar Coverage by a Hole'.

HHH's conservative approach is understandable, given the limitations of the *K*-coronameter data, which they discuss in detail. We note that these data are particularly insensitive to the detection of small coronal holes and cannot give accurate locations of the boundaries of large holes, especially those obscured by brighter structures in the line of sight. These problems are more severe near the poles at solar maximum where the *pB* signal contains a large contribution due to numerous bright structures in the mid-latitudes.

The evolution of the high-latitude holes in the northern hemisphere followed a similar, but more complicated pattern. HHH noted that redevelopment of the north polar hole occurred in a manner similar to that in the south. A small positive-polarity (new-cycle) hole developed at mid-latitudes and expanded towards the pole to eventually cover it; however, this process lagged that of the south and took longer. The delay in establishing a persistent polar hole was apparently related to an anomalous 'wave' of poleward-moving flux which caused the north pole to reverse its polarity twice more after the initial reversal (e.g., Waldmeier, 1973).

Our independent interpretation of the *K*-coronameter data indicates that north polar coverage by a hole occurred 1 to 2 rotations earlier than HHH's suggestion (i.e. CR 1572-73 rather than 1574). This event was preceded by the growth of a high-latitude, positive-polarity hole which developed on or before CR 1561 (May 1970). HHH thought this hole disappeared then reappeared between CR 1567 and 1570, but we believe that the hole only fluctuated in area, possibly because of a surge of negative flux which swept through the northern mid-latitudes (Howard and LaBonte, 1981). The X-ray image for 7 March, 1970 (Figures 2 and 3) revealed low emission over the north pole although that pole was tilted away from our view. Bright arcades overlying the broken polar crown at N 50-60° likely obscured the north pole in the *K*-corona data.

## 2.2. THE REDEVELOPMENT OF THE POLAR HOLES IN CYCLE 21

The study of the birth and evolution of coronal holes in the present solar cycle is improved because of the availability of continuous synoptic He I-10830 Å data from KPNO. Advantages to the 10830 Å data are their high spatial resolution and the minimal obscuration of hole boundaries due to overlying structures. Disadvantages include a poor understanding of the close correspondence between He I absorption and hot coronal material (Kahler *et al.*, 1983), and limb darkening in coronal holes (Harvey and Sheeley, 1977). Additional data available included AS & E X-ray rocket images obtained at the maximum and early decline of the solar cycle (as marked in Figure 1)

7 NOVEMBER 1979

13 FEBRUARY 1981

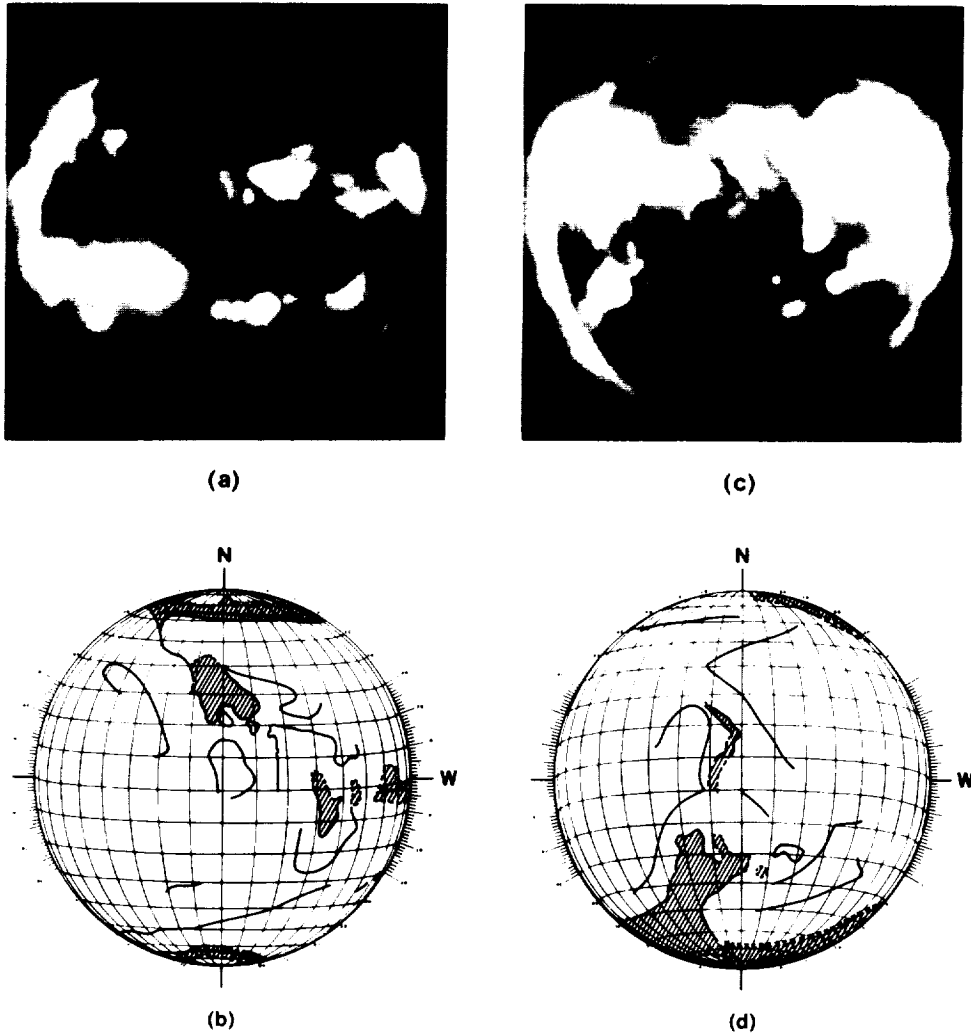


Fig. 4. *Top*: AS & E X-ray rocket images of the corona obtained on 7 November, 1979 (a) and 13 February, 1981 (c). The passbands of the images were  $8 \approx 100 \text{ \AA}$  and  $8\text{--}39, 44\text{--}64 \text{ \AA}$ , respectively. *Bottom*: Tracings on Stonyhurst disks of the boundaries of the darkest areas on the 7 November, 1979 (b) and 13 February, 1981 (d) X-ray images. Dashed lines indicate less well defined boundaries. Also shown are the principal (solid lines) neutral lines and filaments transferred from the synoptic charts for CR 1688 and 1705.

and a complete atlas of  $H\alpha$  synoptic charts with  $10830 \text{ \AA}$  coronal holes superimposed.

Figure 4 presents the AS & E X-ray images obtained on 7 November, 1979 (a), near solar maximum, and on 13 February, 1981 (c), 14 months after maximum. These images had similar sensitivities at the film plane and covered similar solar longitudes ( $\text{CMP} \approx 300^\circ \text{ L}$  for both images). At the bottom of the figure are tracings of the

boundaries of the darkest areas on the X-ray images, and tracings from H $\alpha$  synoptic charts for CR 1688 and 1705 of the definite (solid) neutral lines and filaments which were located near the dark X-ray features. Since neutral lines tend to border coronal holes and lie within coronal cavities (e.g., McIntosh *et al.*, 1976), they help us to separate these two types of dark X-ray features. Again, we used high contrast transparencies to make the X-ray drawings. We believe that the low contrast of the solar corona near maximum is physically real (Kahler *et al.*, 1983).

No polar holes are evident on the 7 November, 1979 image, nor on another X-ray rocket image obtained on 16 November, 1979. Together these images provided coverage of approximately 2/3 of the solar disk near solar maximum. The dark lanes near the poles corresponded to polar crown or high-latitude filament channels. A small hole may have appeared near the south pole on 16 November, but it was probably of negative polarity, i.e., indicative of old-cycle flux. Small mid- and high-latitude coronal holes appeared on both images. We conclude that the overall appearance of the low corona at the maximum of cycle 21 was similar to that of cycle 20. Examination of the X-ray images and the H $\alpha$  charts showed that there were small mid-latitude holes but no conspicuous polar holes, and no large-scale organization of 'new-cycle' polarity at high latitudes.

By February 1981, early in the decline of cycle 21, the X-ray image revealed a large, asymmetric coronal hole extending to near the south pole. The solar south pole was visible on the disk just as in March 1970. A coronal hole may have been present near the north pole, but this is uncertain because that pole was tilted away from Earth.

Spectroheliograms taken in the He I - 10830 Å line have been obtained daily at the KPNO since mid-1974 and have been used to map the boundaries of the coronal holes onto H $\alpha$  synoptic charts, which places the coronal holes in context with the patterns of large-scale solar magnetic fields, active regions and filaments. The accuracy of this mapping depends on observer bias in determining the hole boundary from daily images, day to day contrast variations between the hole and its surroundings, and the transfer of the data to a rectangular grid. As is the case for the H $\alpha$  data, subjective variations in the mapping are minimized by only mapping features which persist from day to day. We have assumed that for our study of large-scale evolutionary patterns the location of hole boundaries, mapped in this way, is sufficiently reliable. This assumption is supported by the observation of consistent and persistent patterns on the charts from one rotation to another.

The visibility of coronal holes in 10830 Å is a separate question. Kahler *et al.* (1983) have recently reviewed the comparisons of coronal holes seen in 10830 Å with He II - 304 Å and soft X-ray images. They compared six AS & E rocket X-ray images with 10830 Å images and found good agreement between the boundaries of large holes but poor agreement for mid- and low-latitude small holes, which were of low contrast, from 1976 to 1981. Limb darkening in coronal holes is also more pronounced in the 10830 Å line (Harvey and Sheeley, 1977). Combined with foreshortening and the variation of the solar  $B_0$  angle, these factors somewhat compromise the use of the 10830 Å data for detecting polar holes. However, although the boundaries of high-latitude holes are uncertain, the existence and large-scale evolution of these holes are

well observed in the synoptic data. Also, Fisher (1982) has shown that around solar maximum 10830 Å coronal holes of sufficient size and lifetime were always detected by the HAO M-III K-coronameter.

The relationships between coronal holes and the large-scale magnetic field patterns displayed on the H $\alpha$  synoptic charts have been examined by McIntosh *et al.* (1976) and Bohlin and Sheeley (1978). Coronal holes consistently lie near the center of unipolar magnetic areas whose dimensions usually exceed 30 heliographic degrees. The hole boundaries generally parallel the paths of adjacent neutral lines, with a constant separation between hole and neutral line. The shapes of coronal holes, therefore, mimic the forms of the surrounding magnetic cells as bounded by the H $\alpha$  neutral lines.

These relationships can be illustrated using charts where the areas of negative polarity are shaded dark, and coronal holes are crosshatched. The relationships are temporal as well as spatial, so a time series of charts, made by dividing the shaded synoptic charts into narrow zones of latitude and then assembling the zones in time series (McIntosh, 1980, 1981), is used. Figure 5 displays the zone for the southern high latitudes (south at the bottom) for the period encompassing solar cycle maximum, the polar polarity reversal and early decline of the solar cycle (May 1979–April 1982; CR 1682–1720). Although these zones extend only to 70° latitude, the original H $\alpha$  synoptic charts and daily 10830 Å images were used to confirm the boundaries of coronal holes above 70° latitude.

During the period shown in Figure 5a, a high-latitude, negative-polarity (black) coronal hole disappeared about the time of sunspot maximum. This hole was within a polar crown gap (PCG – McIntosh, 1980), seen as a dark diagonal sloping to the left with time. The PCG closed rapidly in late 1979 during the apparent deceleration of the positive-polarity (white) area to the west (right) and the demise of the coronal hole. These observations mimic those of cycle 20, when the closure of the PCG occurred exactly 11 years earlier, in late 1968 (McIntosh, 1980).

After this time the south polar region gradually became dominated by positive, new-cycle polarity. The reversal of polarity in the polar regions evidenced by the movement of the polar crown beyond the lower border (S 70) of this zone by CR 1701 (Figure 5b), followed the closure of the PCG by at least six months.

The first persistent mid-latitude coronal hole appeared on CR 1695. Figure 5b shows that this hole formed near the center of a growing positive-polarity area which encircled the Sun by early 1981. The hole grew in size and expanded poleward until it dominated the polar region by mid-1981 (after CR 1710, Figure 5c).

This episode was followed by a poleward surge of negative polarity flux from CR 1709 to 1722 which coincided with a large reduction in the high latitude hole area. The surge is seen as increased black polarity at high latitudes in Figure 5c and as a prolonged negative downturn in the magnetic field averages at mid- to high-latitudes (Section 3.1). This surge began at lower latitudes, progressed poleward and was contemporary with the development of a second mid-latitude hole on about CR 1714 at L 260°. Like the first such hole, this hole grew in size and expanded poleward until it connected to the first coronal hole at the pole on CR 1721.

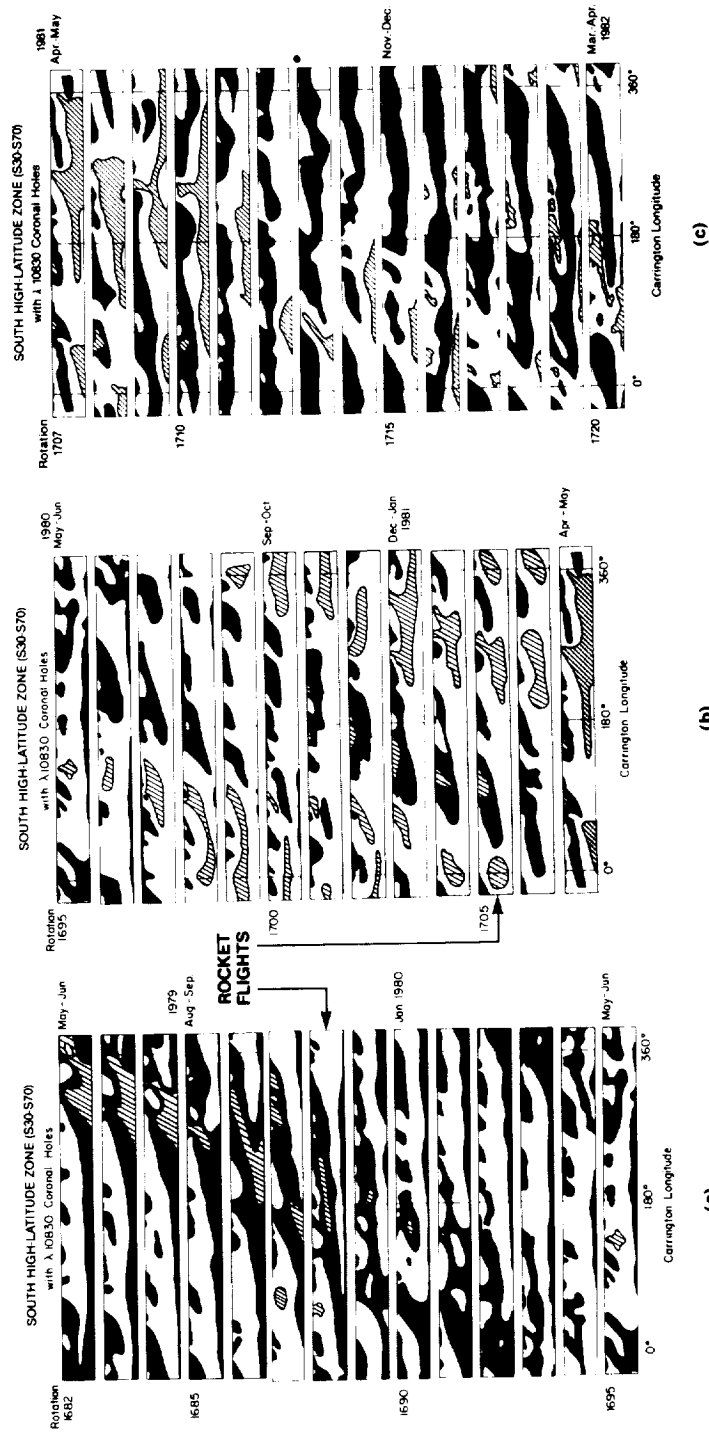


Fig. 5. A time series of portions of H $\alpha$  synoptic charts for high solar latitudes encompassing the period of sunspot maximum, polar polarity reversal and early decline of solar cycle 21 (May, 1979 - April, 1982). The upper border of each strip is at S30° and the lower border at S70°. Black areas are negative polarity; white are positive polarity; grey and cross-hatched areas are coronal holes mapped from KPNO HeI-10830 Å images. The bottom strip of each column is repeated at the top of the next column. The rotations during which the AS & E rocket images of Figure 4 were obtained are indicated.

ORIGINAL PAGE  
BLACK AND WHITE PHOTOGRAPH

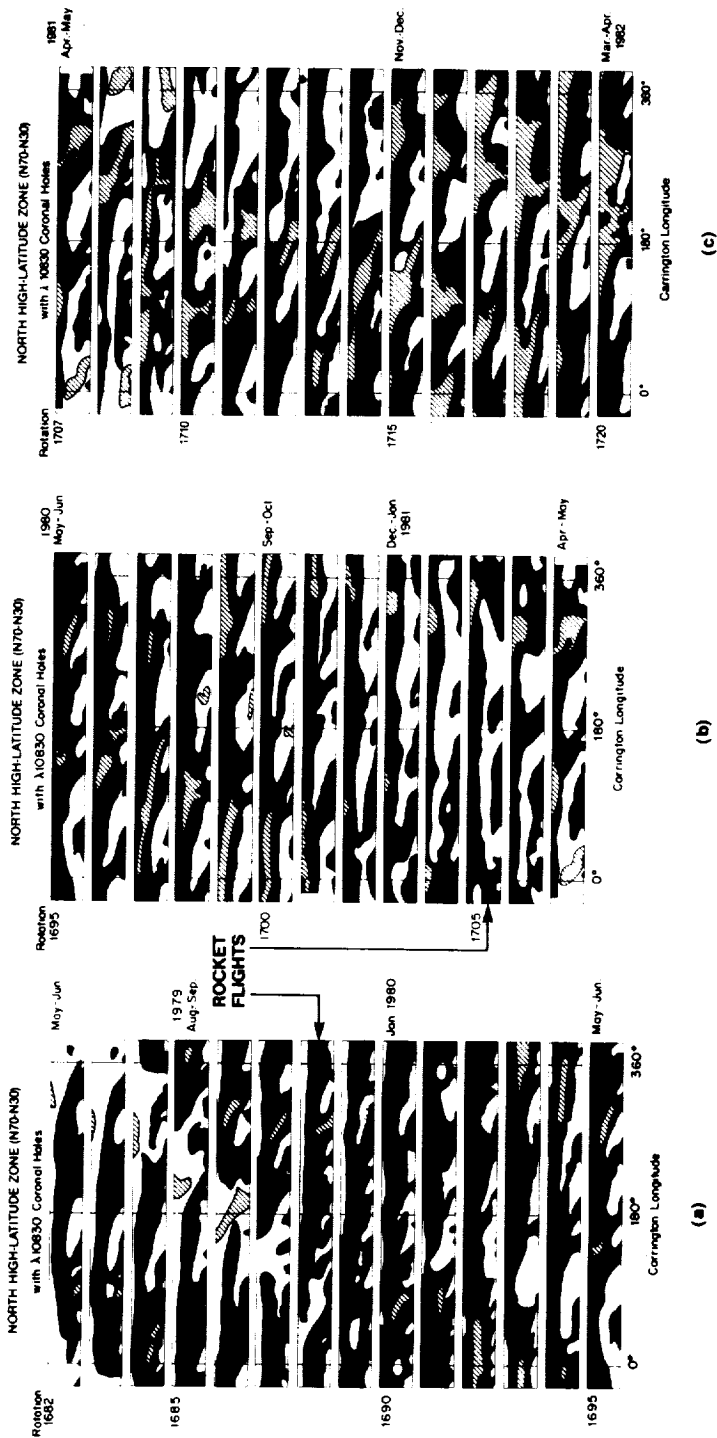


Fig. 6. High-latitude zones for the northern hemisphere for the same period as in Figure 5. The upper border of each strip is at  $N 70^\circ$  and the lower border at  $N 30^\circ$ .

The time when the south pole became covered by a coronal hole is uncertain because of the changing solar  $B_0$  angle and the reduction of the high latitude hole area through late 1981 and 1982. By CR 1717, when the  $B_0$  angle was favorable, the pole appeared to be covered over all longitudes to a latitude of at least  $S 80^\circ$ .

The evolutionary process in the northern hemisphere during solar cycle 21 was similar to that in the south, but more complicated, just as in the previous solar cycle. Figure 6 displays the northern high-latitude zone (north at the top) for the same period as Figure 5. The PCG is white (positive-polarity) and closed rapidly from CR 1687 to 1689, identical with the time of closure of the southern PCG. The polar crown is the upper border of the large black (negative-polarity) area centered within the zone for CR 1682 at the top of Figure 6a. The movement of the polar crown past the  $N 70$  border occurred by CR 1695, two rotations earlier than the southern polar crown.

By CR 1690 the northern hemisphere was encircled at high latitudes by negative (new-cycle) polarity flux. Within this belt the first persistent mid-latitude hole formed on CR 1690, very soon after the PCG closure and five rotations earlier than for the southern hemisphere. A second, persistent, mid-latitude hole formed on CR 1695 at  $130^\circ L$ . The first failed to grow and did not move to the pole. The second hole expanded rapidly on CR 1697 (Figure 6b) both toward the pole (top) and toward the equator. It extended beyond  $N 70$  by CR 1699. Its lower-latitude portion could be identified continuously through CR 1719 (March 1982).

By CR 1712 the pole appeared completely covered by a hole. But in the interval CR 1700–1712 the situation was confused, probably because of another poleward surge of flux. This surge occurred from about CR 1708 to 1714 and is seen as increased white (positive) polarity at high latitudes (Figure 6b, c) and as a positive poleward-moving peak in the magnetic field averages (Figure 7). The earliest time of coronal hole coverage of the north pole was as much as a year earlier than for the southern hemisphere. This time was better established than for the south because the coverage of the pole occurred during the time when the solar  $B_0$  angle favored viewing of the north pole.

### 3. The Polar Magnetic Field Evolution Around Maximum

There are two other specific observational tracers of the evolutionary pattern of the magnetic flux that can be related to polar hole evolution near sunspot maximum. They are the dependence of the time of reversal of the long-term average photospheric field strength as a function of latitude, and the evolution of the polar crown of filaments.

#### 3.1. THE MAGNETIC POLARITY REVERSAL

The most detailed discussion of the polar polarity reversal during cycle 20 was given by Howard (1972, 1974). Using Mt. Wilson magnetograph data, he observed successive reversals of the sign of the field to the new-cycle polarity starting at  $40\text{--}50^\circ$  latitude and proceeding to the pole. The time for this 'migration' was 1 to  $1\frac{1}{2}$  yr and similar patterns were observed at both poles, although not in phase. The reversal occurred at least 11 rotations earlier in the south than in the north, in agreement with the pattern of the development of the high-latitude and polar coronal holes.

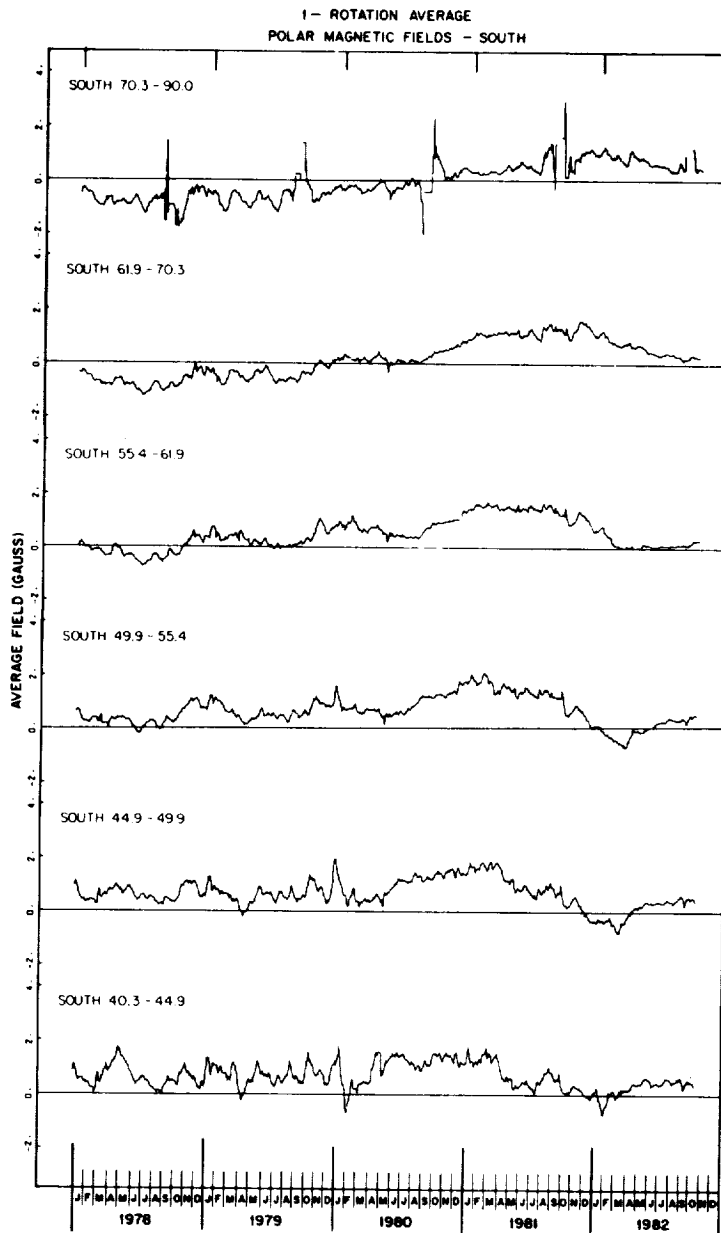


Fig. 7a.

Fig. 7a-b. The variation of the southern (a) and northern (b) photospheric magnetic field strength averaged over six latitude intervals from 1978 through October 1982. The zero level is drawn for each latitude interval. The field averages are 27-day running means. The large excursions in the data above  $70^\circ$  are related to data gaps and instrument recalibrations at times when the respective poles had their maximum tilt away from the Earth. These data are from Mt. Wilson Observatory, courtesy of R. Howard.

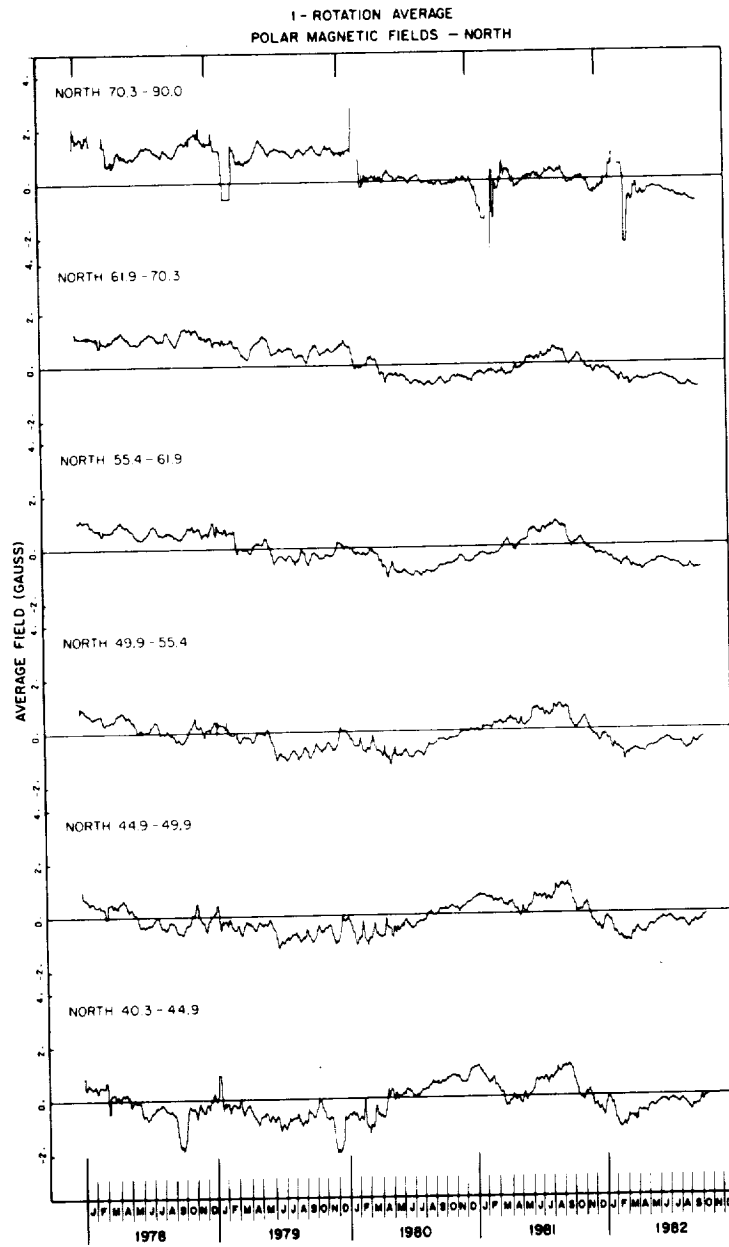


Fig. 7b.

R. Howard has kindly provided Figures 7a, b, which are plots of the north and south photospheric field, respectively, averaged over six latitude intervals from 1978 to 1982. We can see that a long-term reversal to new-cycle polarity (negative in the north, positive in the south) occurred above latitudes  $70^\circ$  around March 1980 in the north and about 6 months later in the south, although the data contain significant fluctuations and the zero level is uncertain. Because the polemost latitude band that the magnetograph samples is large, these measurements underestimate the time of reversal at the pole. However, the poleward reversal 'wave' moves so rapidly in each hemisphere that the actual polar reversal is anticipated by, at most, 1–2 rotations. (A tendency for earlier reversal at successively lower latitudes is also apparent.)

As mentioned earlier, the timing of the reversals in cycle 21 was complicated by apparent poleward movement of old-cycle polarity flux in both hemispheres. This occurred earlier and was more clearly delineated in the north. The northern surge also produced a clear but temporary positive shift in the long-term, increasingly negative polar field (Figure 7b, mid-1981). However, the effect of this shift in the polar field was very weak and the second 'reversal' was out-of-phase with the timing of the other tracers. Therefore, although in Table I we have listed two times when the northern field above  $70^\circ$  reversed polarity from positive to negative, we conclude that the earliest reversal was the 'true' one.

The southern surge did not appear to be strong enough to reestablish negative flux above  $70^\circ$  S, so we list only one reversal time for the southern hemisphere.

Table I list the times of the sunspot peak in each hemisphere (column 3) and the times of polarity reversals above latitudes  $70^\circ$  (column 4), both for cycles 20 and 21. It follows from dynamo models that the differences in the time of the polarity reversal for the two poles should depend on the differences in flux production in the two hemispheres. A crude, but commonly used measure of the amount of flux appearing on the solar surface is the sunspot number, which has been plotted separately for each hemisphere by White and Trotter (1977) through cycle 20. Such segregated counts were not available for the present cycle, so we used counts of the number of SESC regions (active regions assigned a serial number by NOAA Space Environment Services Center) occurring in each hemisphere during cycle 21. This estimate was made from the weekly NOAA *Preliminary Report and Forecast of Solar-Geophysical Activity*, without resorting to counting the number of groups on individual sunspot drawings. More regions formed in the northern hemisphere throughout the rising portion of the solar cycle. The northern hemisphere strongly dominated during the 6 months just prior to sunspot maximum. The southern hemisphere then dominated for the six months ending in August 1980. The lag time and the order of dominance between the two hemisphere mimicked that between reversals of the northern and southern poles for the last two cycles, suggesting that the amount of flux generated in each solar hemisphere determines the order and timing of the polar magnetic field reversal.

We see that in cycle 20 the south pole reversed at least  $\frac{3}{4}$  of a year before the north, and in cycle 21 the north pole reversed first, about  $\frac{1}{2}$  a year before the south. For both cycles the general pattern of development of new-cycle polarity coronal holes followed

these reversals in this same sequence. These observations are therefore consistent with our expectation for the general evolution of the polar field following sunspot maximum, as set forth in the Introduction. For completeness we have included in Table I Babcock's (1959) estimate of the time of reversal during cycle 19, when the south reversed about  $1\frac{1}{2}$  yr before the north.

### 3.2. THE DISAPPEARANCE OF THE POLAR CROWN

The final observational parameter that must be accounted for in models of the solar cycle is the poleward migration of the polar crown of filaments (e.g., Leighton, 1964). After sunspot minimum filaments in the mid-latitudes begin to move toward their respective poles. The locus of filaments maintains a nearly constant distance of  $20^\circ$  from the boundary of the shrinking polar hole (Waldmeier, 1981); in fact the coronal arcades overlying the filaments form the physical boundary of the polar hole (McIntosh *et al.*, 1976). For the past several cycles the reappearance of the polar holes has occurred close to the time of arrival near the pole, and disappearance, of the polar crown (Waldmeier, 1981).

We have determined the time of disappearance of the polar crowns for cycles 20 and 21 through the use of  $H\alpha$  synoptic charts (McIntosh, 1979; *Solar Geophysical Data*) and high-latitude zonal diagrams derived from the  $H\alpha$  charts (like Figures 5 and 6). This method permits us to observe the systematic motions of features on the maps. Integration of daily measurements of filaments at latitudes higher than  $60^\circ$  minimizes the uncertainties in the position of the polar crown.

Using mean values of the latitude distribution of prominence areas, Waldmeier (1973) was able to determine the poleward migration rate and time of arrival at the pole of the polar crown for cycle 20. Using the  $H\alpha$  synoptic charts, we have developed similar curves for cycles 20 and 21 which show the maximum latitude reached by the polar crown on each solar rotation. The times of polar crown disappearance listed in column 6 of Table I were determined to be the rotation on which the last conspicuous polar crown filament was observed.\* The disappearance times for cycle 19 were estimated from Waldmeier's (1981) Figure 5.

## 4. Summary and Discussion

### 4.1. SUMMARY OF RESULTS

We will now attempt to synthesize these observations in order to learn more about the polar evolution of the solar magnetic field. Several caveats are required for the interpretation of these data: (1) Like other solar synoptic observations, the data are noisy and

\* From Waldmeier's (1973) data on the evolution of the northern polar crown in cycle 20 one would infer an earlier disappearance time than ours. This is because his 'anomalous' polar crown (also referred to by Howard, 1974) was not the final one. Following the passage of the 'anomalous' front the polar field was of negative polarity. It then switched to the new-cycle (positive) polarity after the passage of the final polar crown.

best used to discern longer term trends. This is especially true of the polar observations which are effected by foreshortening and the tilt of the solar axis with regard to the ecliptic. (2) As noted by Howard (1974) the timing of the magnetic polarity reversal is uncertain, requiring several years of data around solar maximum to ascertain its actual occurrence. (3) Coronal hole boundaries were determined from different sets of data in cycles 20 and 21. In cycle 20 we used higher altitude *K*-coronameter, X-ray and EUV data and in cycle 21 we used primarily lower altitude He I-10830 Å data. The detailed intercomparison of hole boundaries determined at these different wavelengths is not well understood, but knowledge of the general location and evolution of the larger holes should be sufficiently accurate for our purposes. (4) Because of these limitations we estimate that the uncertainties in the timings of Tables I and II are of the order  $\pm 2$  rotations.

First we summarize the high-latitude magnetic evolution near the maxima of the last two cycles. In cycle 20 the polar polarity reversal and polar hole redevelopment occurred first in the south. Mid-latitude holes developed in late-1969 and evolved into three holes which joined at the south pole in mid-1970. The polar crown disappeared in the spring of 1970. This process took longer in the north, lagged that of the south and was more complicated. A persistent, mid-latitude hole did not appear in the north until mid-1970, following by half a year the development of such a hole in the south. The polar hole redeveloped in the spring of 1971. In both hemispheres, polar hole development lagged the appearance of the mid-latitude holes by about one year. In cycle 21 a similar pattern was followed except that all of the key events, including the peak of flux emergence, occurred first in the north. The northern polar hole redeveloped in mid-1981 and the southern in late 1981. These holes lagged the appearance of persistent mid-latitude holes of new-cycle polarity by 1–2 yr. The magnetic reversal process in the north preceeded that of the south by about 6 months, as did the polar crown disappearance. In each hemisphere the complete coverage of the pole by a hole was delayed by poleward surges of late-emergent flux.

These observations can be organized by relating the timing of the key high latitude events to the polarity reversals. Table II is adapted from Table I and shows the lag times in Carrington rotations from the time of the earliest indication of the polarity reversal

TABLE II  
Lag times from polar polarity reversal (Carrington rotations)

Cycle No.	Pole	Mid-latitude hole appearance	Polar crown disappearance	Polar hole encirclement
21	N	-3 to +3	+ (8 to 9)	+ (18 to 20)
21	S	-4	+8	+ (11 to 17)
20	N	$\geq +1$	+9	+ (11 to 15)
20	S	$\geq (-2 \text{ to } +7)$	+13	+ (9 to 10)
19	S	-	+ (20 to 25)	-
19	N	-	+12	-

above  $70^\circ$  in each hemisphere to the time of the following events: the development of the mid-latitude hole of new-cycle polarity, the disappearance of the last conspicuous polar crown filament, and the earliest coverage of the pole by a hole. We summarize these results as follows: In each hemisphere the peak of the flux emergence (in terms of sunspot number), the appearance of the mid-latitude hole(s), and the polarity reversal at the pole all occurred within a few months of each other. This is particularly true if we compare the time of the earliest indication of the polar reversal and the earliest birth of a mid-latitude hole. The polar crown disappearance and the redevelopment of the polar hole occurred between 8 months and  $1\frac{1}{2}$  yr after the polar reversal. Polar hole coverage occurred at or after the time of polar crown disappearance in both cycles, lagging by about one year in both hemispheres in cycle 21.

#### 4.2 DISCUSSION

We have examined the observations relating to the evolution of the high-latitude solar magnetic field around sunspot maximum, when the net polar flux switches polarity and coronal holes redevelop around the poles. We now integrate our results with the phenomenological concepts of coronal hole evolution near maximum mentioned in the Introduction. Before activity maximum, flux in the form of BMRs emerges at mid-latitudes. The trailing part of this flux, of opposite polarity to that of the old cycle at the poles, moves toward the poles, canceling the unipolar field there and reducing or eliminating the area of the pole occupied by a coronal hole. Near sunspot maximum a sufficient amount of trailing polarity flux has arrived at the poles to switch the polarity of the net flux, although a large amount of mixed polarity remains. In the mid-latitudes at this same time the field has reversed and the unipolar area of trailing polarity field is sufficiently large for small holes to form. After maximum, as the amount of new flux brought to the surface begins to decline, large unipolar areas of new-cycle (following) polarity begin to dominate the mid- to high-latitude region. In two or three longitude zones the small holes begin to enlarge. Although they can spread very rapidly, for a period of time they are prevented from encircling the Sun at high latitudes because of residual flux emergence and poleward flows of net old-cycle flux. The unipolar cells and the holes within them persist and grow larger until they join at high latitudes to cover the pole. At about this time the polar crown, which is supposed to form the boundary between the old-cycle (or mixed) polarity of the pole and the new-cycle, high-latitude polarity, begins to break up and disappear as it nears the pole. Although the development time of the new-cycle, high-latitude holes for these two cycles varied from 6 months to  $1\frac{1}{2}$  yr, the appearance of the polar hole occurred within several rotations of the disappearance of the polar crown in both cycles.

A major goal of our study is to provide a firmer observational context for the development of models of the solar cycle. Toward this end we comment below on the following results of our analysis which we believe must be taken into account in future models of the solar cycle.

First, the process of polarity reversal accompanying the redevelopment of the polar

holes is not a smooth process that sweeps the trailing flux from the emerging flux belts to the pole. Instead it is discontinuous, occurring in equally-spaced longitude bands. These patterns are apparent in the zonal charts (Figures 5 and 6) as diagonals formed by the large-scale magnetic cells and the coronal holes within them. The slopes of these diagonals indicate the rate of rotation of the features relative to the Carrington rate. These rates suggest a slowing of the large-scale features around the time of the cycle 21 polarity reversal, similar to that found for cycle 20 (McIntosh, 1980).

These patterns are reflected in all of the magnetic tracers that we have examined; i.e., coronal holes, latitudinally averaged photospheric magnetic fields, and the polar crown. This process is perhaps best seen in the coronal hole evolution. Small mid-latitude holes form when the magnetic cells at that latitude become large enough. Eventually one or more of them continues to grow in area and to move poleward until a segment reaches the pole. This latter process yields the large, asymmetric, high-latitude holes discussed earlier and found to be typical of high-latitude holes soon after maximum. The ultimate development of a symmetrical polar hole does not occur until a second poleward thrust of unipolar new-cycle field, as evidenced by the growth of a second magnetic cell and mid-latitude hole. This second hole develops at a longitude  $180^\circ$  from the first, and lags the first by 5–10 rotations. The observed poleward movement of the old-cycle field (Figure 7), after the early polar reversal and mid-latitude hole appearance, tends to disrupt the growth of new-cycle field, to maintain the asymmetry of the high-latitude holes, and to diminish the hole area. If the surge reaches the polar zone, the polar crown will be reestablished in that longitude band. This yields the kind of 'anomalous' polar crown first reported by Waldmeier (1973) in the north in cycle 20.

There is a persistent asymmetry between the two solar hemispheres in the timing of the processes discussed above. For instance, in any given cycle the magnetic polarity reversal between hemispheres is offset by 6 months to  $1\frac{1}{2}$  yr. Our results have confirmed such an asymmetry for the present cycle and indicate that the polar crown and high-latitude coronal hole evolution also follow this pattern for cycles 20 and 21 (Table I). Our sunspot group data for cycle 21 and the extensive sunspot number data of White and Trotter (1977) suggest that such an asymmetry is a characteristic of the maximum of the solar cycle.

Our second result concerns the relationship between the polar field reversal and the polar crown disappearance. The polar crown is hypothesized to form the boundary between the poleward-receding old-cycle flux and the advancing new-cycle flux. If this idea were correct, then we could use the time of disappearance of the polar crown to infer the time of polarity reversal at the pole. We can predict that this inferred time should be approximately the same as that implied by magnetograph polarity measurements. If the strongest new-cycle field lay  $15\text{--}20^\circ$  equatorward of the polar filaments, we might expect the measured reversal to lag the inferred reversal by several rotations. Howard (1974) first noted that for cycle 20 this relationship was not as good as expected. We have found that, for the last two cycles, the *opposite* actually occurred; i.e., the polar crown consistently disappeared 6 months to 1 year *after* the magnetic polar reversal.

It is possible to explain this sequence in terms of the presence of the poloidal field of the new cycle, which, in  $\alpha - \omega$  dynamo models, is generated by the toroidal current associated with the toroidal field component. The poloidal field, although essential to the regeneration of the dynamo, is much weaker than the toroidal field and would therefore be difficult to observe. In fact, doubt has been cast on its existence and subsequently used as argument against the  $\alpha - \omega$  mechanism (Layzer *et al.*, 1979). However, at the time of the polar field reversal, the toroidal components of the old and new cycle flux might be expected to cancel, thus allowing the poloidal field to be observed. Our observations suggest the following scenario: With the appearance of new-cycle flux at mid-latitudes, the quantity of old-cycle flux migrating poleward will gradually diminish. If a point in time is reached, before the new-cycle flux reaches the polar zone, when the polar zone flux from the old cycle falls below the level of the poloidal component arising from the new cycle, a reversal in the measured average field strength in the polar zone would occur. Thus the apparent contradiction in the observations would be removed; the polar crown would still form the boundary between the *toroidal* fields of the old and new cycle. As the new cycle builds and its flux migrates poleward, the polar crown will dissipate and the toroidal component will again dominate the field measurements. If this interpretation is correct, it provides the first evidence for the existence of a reversing poloidal field component which is critical for kinematic models of the solar dynamo.

Finally, our observations appear to support recent studies of the magnetic field (Howard and LaBonte, 1981) and polar filaments (Topka *et al.*, 1982) which suggest that there is a poleward meridional flow averaging about  $10 \text{ m s}^{-1}$ . These authors have interpreted this flow as the result of a large-scale poleward circulation that cannot be accounted for by Leighton (1964) - type diffusion. In the Mt. Wilson data the strongest flows originated in the sunspot belts near solar maximum and moved to the poles in 2-3 yr. We see apparent poleward flows of this magnitude in our data at high latitudes near maximum. For instance, in the south in cycle 21 the polarity reversal wave and the subsequent surge of old-cycle flux moved poleward at about  $13 \text{ m s}^{-1}$ . We estimate that the poleward movement of the high-latitude coronal holes was about  $10-15 \text{ m s}^{-1}$ , but with a large uncertainty due to the difficulty of measuring the coronal hole boundaries at high latitudes.

We can ask if we see any differences in the timing of these events that can be understood in terms of the different levels and distributions of magnetic activity between the last two cycles. Interestingly, the answer is generally no. The polarity reversal occurred first in the south for two consecutive cycles (19 and 20), then in the north in this cycle. A persistent phase lag between hemispheres of 6 months to 1 year was observed. In accordance with the more rapid rate of flux emergence, the polar reversals occurred faster in cycle 21 than cycle 20. On the other hand, the timing of the development of the high-latitude, new-cycle field and the polar crown migration and disappearance were similar during these two cycles. Polar hole coverage appeared to be retarded in cycle 21. This latter result could be due to the increased amount of total flux emergence in cycle 21 and the subsequent disruption in the development of the high-lati-

tude unipolar fields from poleward movement of old-cycle flux. In conclusion, there seems to be no strong correlation between the levels of solar cycle-dependent magnetic activity and the timing of events around the time of the polar polarity reversal.

### Acknowledgements

The authors would like to thank R. Howard, of the Mt. Wilson and Las Campanas Observatories, for providing the magnetograph data and A. Krieger for helpful discussions. We thank the AS & E and NOAA technical publication groups for their assistance with the figures. DFW and JMD were supported at AS & E by NASA Contracts NAS5-25496 and NASW-3586.

### References

- Babcock, H. D.: 1959, *Astrophys. J.* **130**, 364.  
 Babcock, H. D.: 1961, *Astrophys. J.* **133**, 572.  
 Bohlin, J. D. and Sheeley, N. R., Jr.: 1978, *Solar Phys.* **56**, 125.  
 Broussar, R. M., Sheeley, N. R., Jr., Tousey, R., and Underwood, J. H.: 1978, *Solar Phys.* **56**, 161.  
 Fisher, R. R.: 1982, *Astrophys. J.* **259**, 431.  
 Harvey, J. W. and Sheeley, N. R., Jr.: 1977, *Solar Phys.* **54**, 343.  
 Howard, R.: 1972, *Solar Phys.* **25**, 5.  
 Howard, R.: 1974, *Solar Phys.* **38**, 283.  
 Howard, R. and LaBonte, B. J.: 1981, *Solar Phys.* **74**, 131.  
 Hundhausen, A. J.: 1977, in J. Zirker (ed.), *Coronal Holes and High-Speed Wind Streams*, Colorado Associated Univ. Press, Boulder, Colorado, p. 225.  
 Hundhausen, A. J., Hansen, R. T., and Hansen, S. F.: 1981, *J. Geophys. Res.* **86**, 2079.  
 Kahler, S. W., Davis, J. M., and Harvey, J. W.: 1983, *Solar Phys.* **87**, 47.  
 Krieger, A. S., Vaiana, G. S., and van Speybroeck, L. P.: 1971, in R. Howard (ed.), *Solar Magnetic Fields*, D. Reidel Publ. Co., Dordrecht, Holland, p. 397.  
 Krieger, A. S., Timothy, A. F., and Roelof, E. G.: 1973, *Solar Phys.* **29**, 505.  
 Layzer, D., Rosner, R., and Doyle, H. T.: 1979, *Astrophys. J.* **229**, 1126.  
 Leighton, R. B.: 1964, *Astrophys. J.* **140**, 1547.  
 McIntosh, P. S.: 1979, UAG Report 70, World Data Center A for Solar-Terrestrial Physics, NOAA, Boulder, Colorado.  
 McIntosh, P. S.: 1980, in M. Dryer and E. Tandberg-Hanssen (eds.), *Solar and Interplanetary Dynamics*, D. Reidel Publ. Co., Dordrecht, Holland, p. 25.  
 McIntosh, P. S.: 1981, in L. E. Cram and J. H. Thomas (eds.), *The Physics of Sunspots*, Sacramento Peak National Observatory, Sunspot, New Mexico, p. 7.  
 McIntosh, P. S., Krieger, A. S., Nolte, J. T., and Vaiana, G.: 1976, *Solar Phys.* **49**, 57.  
 Nolte, J. T., Davis, J. M., Gerassimenko, M., Lazarus, A. J., and Sullivan, J. D.: 1977, *Geophys. Res. Letters* **4**, 291.  
 Sheeley, N. R., Jr.: 1980, *Solar Phys.* **65**, 229.  
 Sheeley, N. R., Jr., Asbridge, J. R., Bame, S. J., and Harvey, J. W.: 1977, *Solar Phys.* **52**, 1977.  
*Solar Geophysical Data Bulletins*: U.S. Department of Commerce, NOAA, Boulder, Colorado.  
 Stix, M.: 1981, *Solar Phys.* **74**, 79.  
 Topka, K., Moore, R., LaBonte, B. J., and Howard, R.: 1982, *Solar Phys.* **79**, 231.  
 Van Speybroeck, L. P., Krieger, A. S., and Vaiana, G. S.: 1970, *Nature* **227**, 818.  
 Waldmeier, M.: 1973, *Solar Phys.* **28**, 389.  
 Waldmeier, M.: 1981, *Solar Phys.* **70**, 251.  
 White, O. R. and Trotter, D. E.: 1977, *Astrophys. J. Suppl.* **33**, 391.  
 Withbroe, G. L.: 1981, private communication of 16-mm OSO-6 movie.  
 Withbroe, G. L., Dupree, A. K., Goldberg, L., Huber, M. C. E., Noyes, R. W., Parkinson, W. H., and Reeves, E. M.: 1971, *Solar Phys.* **21**, 272.

4.11 The Detection of Soft X-Rays with Charged Coupled Detectors

P. Burstein and J.M. Davis

American Science and Engineering, Inc.  
Cambridge, Massachusetts 02139

ORIGINAL PAGE IS  
OF POOR QUALITY

